Atomic and Electronic Structure of Graphene and Graphene Intercalation Compounds

X-Ray Standing Wave and Scanning Tunnelling Microscopy Studies

I n a u g u r a l - D i s s e r t a t i o n

zur

Erlangung des Doktorgrades

der Mathematisch-Naturwissenschaftlichen Fakultät

der Universität zu Köln

vorgelegt von

Dipl.-Phys. Sven Runte

aus Norden

Köln 2013

Erster Berichterstatter:	Priv.-Doz. Dr. Carsten Busse
Zweiter Berichterstatter:	Prof. Dr. Stephan Schlemmer

Tag der mündlichen Prüfung: 26.11.2013

Abstract

The morphology of graphene/Iridium(111) was studied by x-ray standing wave (XSW) measurements. A dependence of the moiré corrugation on the graphene coverage is observed. A comparison with density functional theory (DFT) reveals a discrepancy on the corrugation caused by stress appearing from the cool down from the preparation temperature. The model of rehybridised graphene due to cluster adsorption is supported by a structure analysis. Graphene intercalation compounds were investigated by scanning tunnelling microscopy (STM), low energy electron diffraction (LEED), and XSW. It is shown that intercalation takes place via cracks and holes at wrinkles and wrinkle crossings. The superstructures of caesium intercalated graphene are resolved. For intercalants interacting mainly via van der Waals forces it could be shown that the graphene-intercalant distance is dependent on the charge transfer. Moreover, the structure analysis supports that oxygen intercalation leads to quasi freestanding graphene. A rigid-band model is introduced and applied to graphene intercalation compounds. Scanning tunnelling microscopy measurements reveal clear indications for Dirac electron scattering at defects. In these processes the pseudo-spin is not conserved leading to both inter- and intravalley scattering.

Contents

Frequently Used Symbols and Abbreviations

$\sqrt{3}_{\mathrm{XY}}$	$(\sqrt{3} \times \sqrt{3})$ with respect to the XY unit cell
$(2 \times 2)_{\mathrm{XY}}$	(2×2) with respect to the XY unit cell
ARPES	Angle Resolved Photoemission Spectroscopy
CLS	Core Level Shift
CVD	Chemical Vapor Deposition
DFT	Density Functional Theory
$F^{(hkl)}$	Coherent Fraction of (hkl)-Reflection
FWHM	Full Width at Half Maximum
GIC	Graphite Intercalation Compound
gr	Graphene
grIC	Graphene Intercalation Compound
HV	High Vacuum
LEEM	Low Energy Electron Microscopy
LT-STM	Low Temperature Scanning Tunnelling Microscope
ML	Monolayer
$P^{(hkl)}$	Coherent Position of (hkl)-Reflection
PES	Photoemission Spectroscopy
R	Reflectivity
STM	Scanning Tunnelling Microscopy/Microscope
STS	Scanning Tunnelling Spectroscopy
TPG	Temperature Programmed Growth
UHV	Ultra High Vacuum
XPS	X-Ray Photoelectron Spectroscopy/Spectra
XSW	X-Ray Standing Waves

PART I

Introduction

In search for novel materials graphene is a promising candidate for diverse applications. This allotrope of carbon combines outstanding electronic and structural properties. Prominent features are the pure two dimensionality and the high charge carrier mobility. As this allows for smaller and faster electronics graphene may pioneer post-CMOS technology [1–5]. Extraordinary effects like room temperature ballistic transport [6] and a half-integer quantum hall effect [3] are found for this material.

Promising applications like high-frequency transistors [7], gas sensors [8], or transparant electrodes are in constant focus of present research. For many envisioned applications in this field tailoring of its electronic structure - by doping or band gap formation - is of high importance. Moreover, due to the high mechanical strength and concurrent extremely low mass density multi-layered graphene was used as a diaphragm for loudspeakers [9].

The preparation of graphene is done by several methods. The most famous one works via exfoliation of a graphite crystal, which was used to measure the transport properties of multilayer graphene presented by researchers in the group of A. Geim [10]. This seminal work lead to exceptional interest in this field, which was the reason for the award of the Nobel Prize in 2010 to A. Geim and K. Novoselov. In this preparation method the topmost graphite layers are peeled off from a graphite crystal by sticky tape. The layers are reduced in thickness by repetition of these peeling steps and finally pressed onto a silicon dioxide wafer for further processing. This preparation leads to few micrometer sized graphene flakes of mono-, bi-, and multilayer thickness surrounded by graphitic grains. Hence, as this process is not controllable and limited to micrometer samples it is useful for academic issues only.

One way to prepare graphene with high structural quality on large scales is the epitaxial growth of graphene. This method allows for high structural quality and macroscopic specimen. However, further experiments were demanded concerning the influence of stress on the morphology, especially buckling of graphene [11]. The high structural quality of epitaxial graphene is due to the interaction with the substrate, which however has a strong influence on the electronic structure of the carbon layer. To overcome this influence by concurrent retaining of the high structural quality intercalation is a good method to achieve quasi freestanding graphene. This was shown for graphene on silicon carbide by hydrogen intercalation, which leads to a saturation of dangling bonds of the silicon surface, and in turn to decoupling of the carbon buffer layer, which becomes quasi freestanding graphene [12].

On metals and silicon carbide several intercalants decouple graphene from the substrate, as it was shown for a wide range of atom species from alkali metals to halogens [13–

24]. While intercalation facilitates transfer of the graphene sheet [25], it also enables the formation of an insulating buffer layer [26].
An exceptional high structural quality is found for graphene on iridium [27], which enables the growth of perfectly aligned arrays of clusters with defined size [28]. This system is expected to have far-reaching consequences for understanding catalytic processes, when changes in its structure and surface chemistry are investigated during catalysis [29].

The content of this thesis involves different topics. The fundamental background is introduced in Part II dealing with the sample system and the measuring techniques. In Part III experimental details are shown. Starting from a description of the experimental setups used for this work also enhancements are presented. The procedures of sample preparation as well as data processing are also described there.
In Part IV the results are discussed. Structural investigations are presented, which address the question of the influence of stress on the morphology of graphene. Cluster arrays on graphene are investigated concerning the atomic structure of this system. Furthermore, the process of intercalation through a graphene layer is discussed and the atomic structure of various graphene intercalation compounds is revealed.
Finally, the electronic structure of graphene intercalation compounds is discussed regarding the doping and the scattering of Dirac electrons.

PART II

Fundamentals

CHAPTER 1

Graphene

This chapter offers a brief introduction to graphene. The atomic structure and the band structure are presented in section 1.1. For a more detailed introduction the reader is referred to literature, e.g. the articles of A. Geim *et al.* [30], A. H. Castro Neto *et al.*[31], and M. I. Katsnelson [32].

1.1 Graphene - a Two Dimensional Crystal

An ideal graphene sheet is a single layer of sp^2 hybridised carbon in a hexagonal structure with infinite size [33], where the three sp^2 orbitals of each atom interconnect the carbon atoms by σ-bonds and the remaining, half-filled p_z orbitals form the π bands filled with delocalised electrons. From the nearest-neighbour-distance of 1.42 Å the lattice constant results to $1.24\,\text{Å} \times \sqrt{3} = 2.46\,\text{Å}$ [34]. A sketch of a graphene layer is shown in Figure 1.1. The unit cell of the honeycomb lattice (pink) contains two carbon atoms (grey and black), corresponding to two hexagonal sublattices (grey and black). As a consequence of this two-atom basis electronic states are composed of states of both sublattices, using two component wavefunctions [30]. The sublattices are indicated similarly to the spin index, as it distinguishes also between two different states [30]. Hence, in analogy to the spin, this index is called *pseudo-spin* [30, 32].

The Brillouin zone is shown in the inset in Figure 1.1 (compare Fig. 2 in Ref. [31]), where the six points at the corner are usually labelled K and K'. For neutral graphene the bonding and antibonding π-bands, π and π^*, touch each other at Fermi energy exactly at these points (see Figure 1.2), which are also referred to Dirac-points [31]. The naming Dirac-point is due to the fact that the linear behaviour of the π-bands can formally be

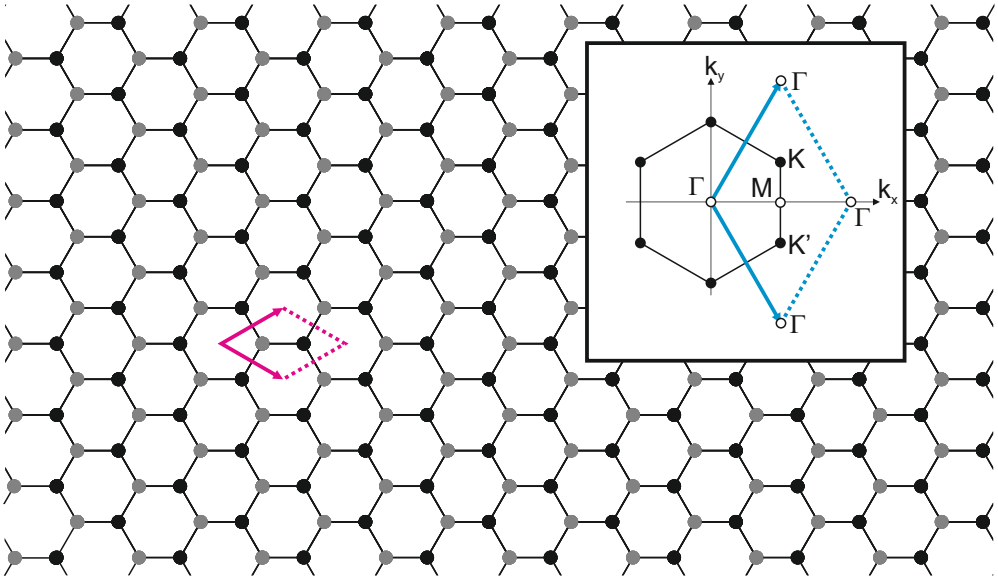

Figure 1.1: Schematic drawing of a graphene layer. Carbon atoms are arranged in a honeycomb lattice. The unit cell contains two atoms (black and grey) as indicated by the pink unit vectors. Inset: Reciprocal space. The two atomic basis leads to a differentiation of the points K and K'. The reciprocal unit vectors are represented by the blue arrows.

described by a Dirac Hamiltonian for quasi-relativistic massless fermions [30]. The absence of a band-gap is closely related to perfect equivalence of both sublattices.

1.2 Graphene/Ir(111)

Graphene on iridium is a good model system for freestanding graphene, because it has a rather weak substrate interaction [35]. Nevertheless, the interaction with the substrate is strong enough to suppress the Raman features, which are often used to identify graphene [36]. However, as it can be prepared with laterally high structural quality up to the millimetre regime [27] it is an ideal system for studies via laterally averaging investigation methods like x-ray standing wave (XSW).

1.2.1 Preparation

Graphene can be prepared utilising catalytic dehydrogenation of hydrocarbons on a hot Ir(111) surface [37]. This leads to a sample thickness of precisely one atomic layer, because the catalytic process is stopped at areas where the iridium crystal is already covered with carbon [37]. In order to prepare a fully closed layer or partly covered iridium surfaces

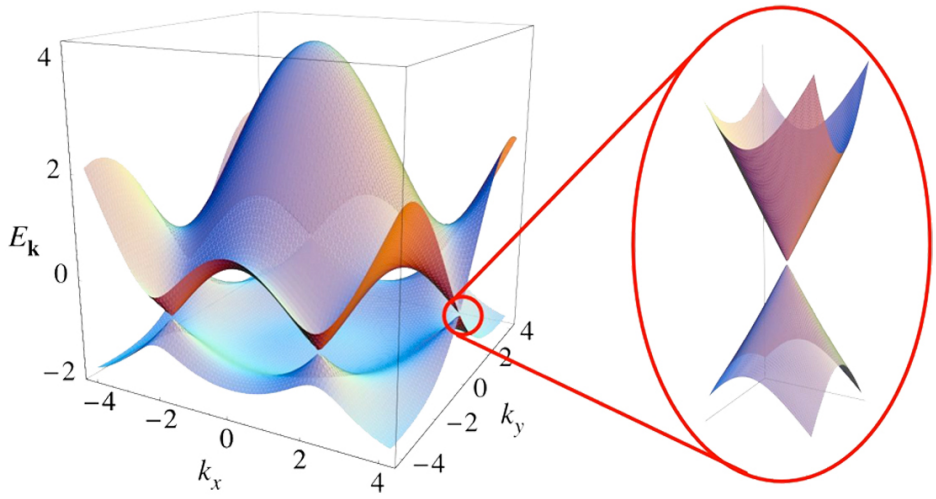

Figure 1.2: Electronic structure of the π^*- and π-bands of a honeycomb lattice. Overview (left) of the π^*- and π-bands and zoom into the rim of the Brillouin zone (right) where both bands touch each other around Fermi energy. The zoom shows the linearity of the band structure around the K-points, which are called Dirac points. Image reprinted with permission from Ref. [31]. Copyright 2009 by the American Physical Society.

one can follow different preparation procedures. Two methods of graphene growth will be explained in the following: Temperature programmed growth (TPG) and chemical vapor deposition (CVD). In both cases ethene (C_2H_4) is often used as the precursor molecule as it has a sticking coefficient of almost one on Ir(111) [38].

TPG is a method where hydrocarbons are adsorbed on the surface at room temperature with subsequent annealing to decompose the hydrocarbon molecules. By using ethene this procedure ends up with a partial carbon covered surface of 22% [37]. In order to increase the coverage this procedure can be repeated, at which the residual area of iridium decreases for each TPG cycle by 22%.

CVD can be used for preparation of a fully closed layer of graphene. The sample is heated in a hydrocarbon atmosphere, so that the decomposition of hydrocarbons on the iridium surface is continuous [38]. For a dose $\gg 1\,\mathrm{L}$ a fully closed layer of graphene can be grown.
In order to prepare a graphene sheet with a high structural quality a combination of a TPG step followed by CVD can be employed. By this, well oriented graphene islands formed during the TPG step act as seeds and grow until they coalesce to a fully closed layer without structural disintegrity of graphene besides small angle tilt boundaries [39].

1.2.2 The Moiré Pattern

The difference in the lattice constants of graphene and iridium leads to an incommensurate $(10.32 \times 10.32)_{\mathrm{gr}}/(9.32 \times 9.32)_{\mathrm{Ir}}$ moiré pattern with a size of the supercell of 25.3 Å [38]. By density functional theory (DFT) calculations including van-der-Waals forces the geometry of the moiré unit cell was calculated [11] as shown in Figure 1.3.

Inside the moiré unit cell three high symmetry regions can be found, which are labelled *hcp*, *fcc*, and *top*. These regions are characterised by the first underlying iridium atom layers. The top-region is that section of the cell, where the centre of a carbon ring is positioned directly above the uppermost iridium atom, while at the hcp- and fcc-region a carbon atom is lying directly on top of a iridium atom. The difference of the hcp- and fcc-regions can be found in the second and third iridium layer: For hcp the centre of a carbon ring is located above the second iridium layer, while for fcc it is located above the third iridium layer [see Fig. 1.3(a,b)]. The charge transfer from graphene towards the iridium substrate is depicted in Figure 1.3(d). In the fcc- and hcp-regions the carbon atoms on top of an iridium atom hybridise with the substrate, and a charge accumulation takes place in between the respective atoms, which indicates the formation of a weak covalent bond. This effect can nicely be seen in the magnification in Figure 1.3(e).

The average height of graphene on iridium(111) in these calculations was determined to be 3.41 Å, which is in good agreement to the experimental value of 3.38 Å from XSW

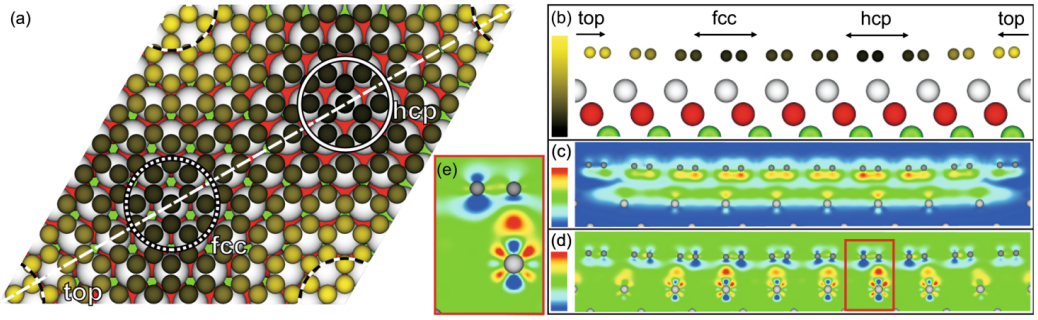

Figure 1.3: DFT calculation of the moiré unit cell of gr/Ir(111). Top view (a) of the moiré unit cell with high symmetry regions (hcp, fcc, top) indicated by circles. Side view (b) along the dashed line in (a) showing the first three layers of iridium atoms (white, red, and green spheres) and the carbon atoms (yellow) in same colour code as (a). Visualisation of the nonlocal-correlation binding-energy density (c) due to adsorption. Charge transfer (d) induced by adsorption, with magnification of the red box in (e). The range of the colour scale is $-0.0138\,\mathrm{e}^{-}\mathrm{Å}^{-3}$ (blue) for a reduced electron density to $+0.013\,\mathrm{e}^{-}\mathrm{Å}^{-3}$ (red) for an enhanced one, while green indicates the average electron density. Image reprinted with permission from Ref. [11]. Copyright 2011 by the American Physical Society.

measurements [11]. However, the DFT calculation had to be performed using a simplified moiré unit cell of $(10 \times 10)_{\mathrm{gr}}/(9 \times 9)_{\mathrm{Ir}}$ [11] and does not include external stress due to the experimental preparation procedure, which will be important for the analysis in Section 8.1.

The moiré pattern has also an effect on the electronic structure of the graphene layer. In Figure 1.4 the result from an angle-resolved photoemission spectroscopy (ARPES) measurement shows the π-band that reveal minigaps that are indicated by the arrows, and replica bands labelled 'R'. The appearance or replica bands and minigaps is related to the moiré potential [40].

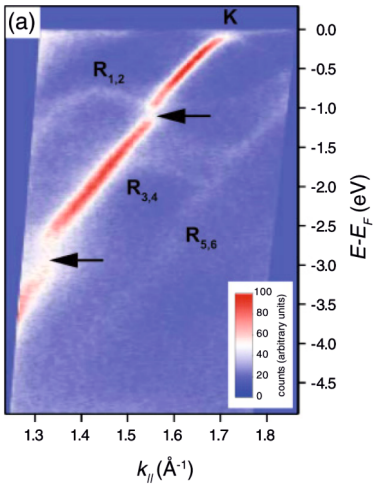

Figure 1.4: ARPES measurement of gr/Ir(111). The linear π-band from the Dirac cone is clearly visible. The position of the K point is indicated by 'K'. Replica bands (faint lines) are indicated by 'R', coming from the Dirac cones of the neighbouring K-points in the Brillouin zone. Minigaps are highlighted by the arrows. Image reprinted with permission from Ref. [40]. Copyright 2011 by the American Physical Society.

1.3 Cluster Growth on Graphene/Ir(111)

Graphene on iridium is well suited for the growth of a cluster array, as experimentally proven for many different metals [28, 41, 42]. Clusters grow layer by layer and form an array with the periodicity of the moiré pattern [28, 42], as exemplary shown for the case of iridium clusters in Figure 1.5. The difference in the brightness of the clusters indicates the difference in height. The inset shows a magnification of the black box, which contains two distinct height levels, which is related to a different number of iridium layers. Note, that due to tip convolution the width of the clusters can not be determined precisely by STM.

The reason for the formation of the cluster array can be found in the DFT calculation already shown in Figure 1.3(e). While a formation of weak covalent bonds at hcp regions takes place, the charge accumulation between the carbon and iridium atoms leads to a charge deficiency in the vicinity of the involved carbon atoms [blue area in Fig. 1.3(e)].

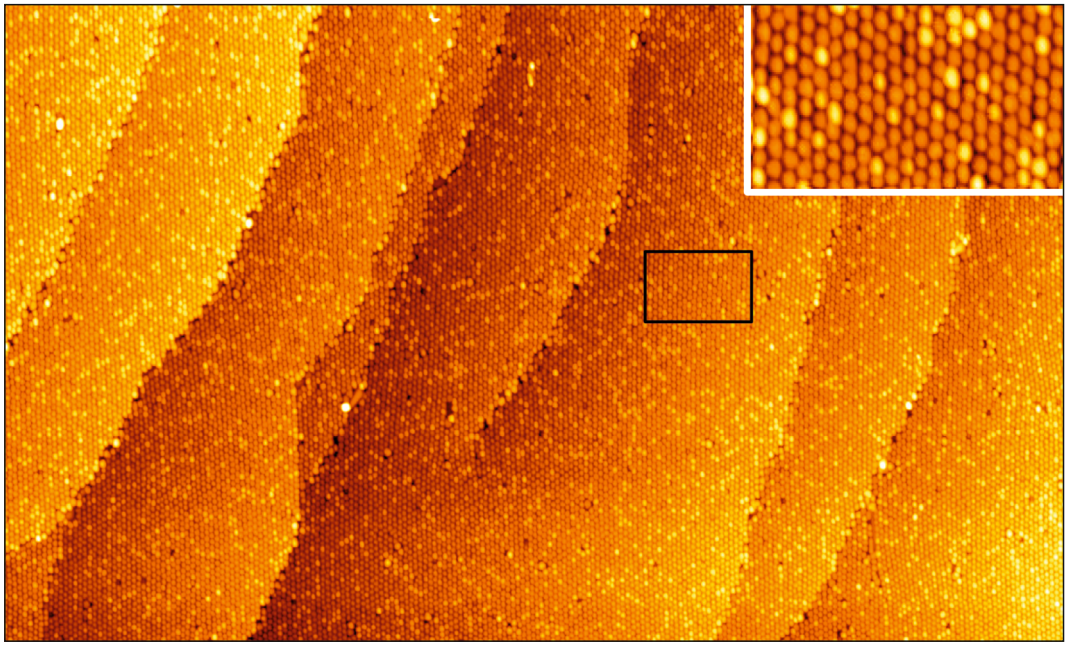

Figure 1.5: STM image of an Ir cluster superlattice on gr/Ir(111). Deposition of 0.8 ML Ir at room temperature forms a well ordered cluster array. Magnification of the black box is shown in the inset. Image size 0.5 μm × 0.3 μm, inset 500 Å × 500 Å. Image reprinted with permission from Ref. [28].

In consequence, the high electronegativity promotes strong bonds of the deposited metal atoms [43, 44]. This explains, why clusters bind preferably to the hcp regions within the moiré unit cell. Furthermore, the binding of cluster atoms leads to complete rehybridisation of the involved carbon atoms, as shown by x-ray photoemission spectroscopy (XPS) and DFT calculations [45]. Moreover, the electronic structure of graphene changes upon cluster deposition, which leads to the formation of a bandgap [46]. However, the position of the clusters regarding the distance to the carbon atoms is not described in literature, but will be revealed in Section 8.2.

1.4 Graphene Intercalation Compounds

The insertion of atoms or molecules between graphite layers, meaning preparing a graphite intercalation compound (GIC), was found to have a high influence on the free carrier concentration, which affects the electrical, thermal, and magnetic properties of graphite [47]. Hence, as the modification of graphene's properties is of high interest for future

applications also graphene intercalation compounds (grICs) are in the focus of present research.

The peculiarity of graphene intercalation compounds is the possibility of strong doping, where for p-doping via fluorine intercalation the Dirac point shifts to $E_\mathrm{D} = +0.8\,\mathrm{eV}$ [15], whereas for n-doping by europium intercalation a shift of $E_\mathrm{D} = -1.4\,\mathrm{eV}$ was observed [48]. This strong effect is caused by the linearity of the band structure close to and the vanishing density of states at the Dirac point, which leads to a significant shift of graphene's band structure upon doping.

The high structural quality of epitaxial graphene is due to the interaction with the substrate, which however has a strong influence on the electronic structure of the carbon layer. To overcome this influence by concurrent retaining of the high structural quality intercalation is a good method to achieve quasi freestanding graphene. This was shown for graphene on silicon carbide by hydrogen intercalation, which leads to a saturation of dangling bonds of the silicon surface, and in turn to decoupling of the carbon buffer layer, which becomes quasi freestanding graphene [12]. On metals and silicon carbide several intercalants decouple graphene from the substrate, as it was shown for fluorine [15, 16], oxygen [21, 22], lithium [13, 14], germanium [23], and silicon [24]. Successful decoupling was also observed for gold intercalation on silicon carbide [17] as well as on metal substrates like on nickel [18–20] and silicon carbide [17].

Many intercalants on several systems are already studied, but as graphene is predicted to be impermeable even to helium atoms, the reason why intercalation is possible and how it takes place was not demonstrated in literature, but will be discussed in Section 8.3 and Reference [49].

CHAPTER 2

Measuring Techniques

A brief introduction on the fundamentals of the measuring techniques is presented in this chapter. The focus of the following pages is to give a short overview on the main principles of the respective techniques.

2.1 X-Ray Photoelectron Spectroscopy

X-ray photoelectron spectroscopy (XPS) is introduced in this section, as this is the basic measurement in an x-ray standing wave (XSW) experiment. For more details concerning XPS the reader is referred to literature, especially to Reference [50].

By irradiating a sample with x-rays it emits photoelectrons. Determining their kinetic energy with an electron analyser this measure can be related to a binding energy of electrons by

$$E_{\text{bind}} = E_{\gamma} - \Phi - E_{\text{kin}}, \tag{2.1}$$

where E_{bind}, E_{γ}, and E_{kin} are the binding, photon, and kinetic energy, respectively, while Φ represents the work function of the sample system.

Beside more complicated effects most of the measured electrons are photoelectrons, that are emitted from various core levels of the atoms. As the binding energy can be related to respective core levels as well as their chemical state due to core level shifts (CLS), the resulting spectrum exhibits features that reveal the chemical composition of the sample.

The total photoelectron yield of a core level, i.e. the integral of the corresponding peak, is proportional to the amount of the atoms present in the sample. Note, that for a

comparison of different core levels the cross sections have to be taken into account, which complicates a quantitative analysis.

2.2 X-Ray Standing Waves

As mentioned before, the total photoelectron yield is proportional to the photon intensity at the atoms. The main idea of the x-ray standing wave technique is the local excitation of photoelectrons, as for this case the yield represents the amount of atoms at this position. This technique is presented in detail in Reference [51, 52]. Further information about XSW can be found in literature, e.g. in References [53, 54]. A short introduction to this topic is presented in the following.

Using Bragg condition for the desired crystal plane of the substrate crystal a standing wave field is created at the position where the incident beam and the reflected beam superpose. By slightly changing the photon energy the phase shift between the incident and the reflected photon beam continuously passes from π to 0, which results in a shift of the position of the nodes towards the crystal planes. Hence, in case of a flat layer of adsorbates lying on the crystal surface the total photoelectron yield changes from a high value, if the antinodes are at the position of the adsorbates to a low value, if the nodes are at this position.

The concurrent fit of the reflectivity, determined as a ratio between the intensity of the incident beam to the reflected beam, and the total photoelectron yield allows for determination of structural parameters, which reveal the height of the adsorbates above the substrate. As detailed in Reference [51, 52] the total photoelectron yield is fitted by Equation 2.2.

$$Y^{(hkl)} = 1 + R + 2\sqrt{R}F^{(hkl)} \cos\left(\nu - 2\pi P^{(hkl)}\right) \tag{2.2}$$

Here, $Y^{(hkl)}$ is the total photoelectron yield for a (hkl)-reflection, R is the reflectivity, and ν is the phase. The results of the fit are the structural parameters coherent fraction $F^{(hkl)}$ and coherent position $P^{(hkl)}$, which are both in the range of 0 to 1. The coherent fraction $F^{(hkl)}$ represents the width of the height distribution while the coherent position $P^{(hkl)}$ contains information on the average height. In the simple case of a symmetric height distribution the coherent position $P^{(hkl)}$ can directly be related to an average height. However, the absolute position is unsure, as the position is determined relative to the standing wave field and the average height h results to

$$h = (n + P^{(hkl)}) \cdot d^{(hkl)}, \tag{2.3}$$

where n is an integer that is chosen by consistency arguments. The parameter coherent fraction $F^{(hkl)}$ represents the width of the height distribution, meaning that a value between 0 and 1 stands for the fraction of atoms at the height determined by the coherent position. Hence, incoherent distributed atoms lead to a reduction of the coherent fraction, given by the ratio of incoherent to coherent distributed atoms.

2.3 Scanning Tunnelling Microscopy

Shortly after the development of the scanning tunnelling microscope (STM) in 1982 [55] G. Binning and H. Rohrer were awarded for their invention with the noble prize in 1986 and the scanning probe microscopy techniques have rapidly developed into important tools for surface physics. A short introduction to the basic of scanning tunnelling microscopy and spectroscopy is given in this section. For more details the reader is referred to literature, e.g. to References [56–58].

The fundamental principle behind this measuring technique is the quantum-mechanical tunnelling effect, which allows a current flow by applying a voltage between two electrodes even without direct contact but through a gap of nanometer size. This is provided by an overlap of the wave functions of mainly those atoms of both electrodes which are closest to each other.

For scanning tunnelling microscopy (also abbr. STM) one electrode is a conducting sample, while the other one is a conducting probe, which in ideal case is an atomically sharp tip. It is brought into tunnelling contact by applying a bias voltage and approaching the tip until a tunnelling current in the order of nanoamps or picoamps is measured. In case of two planar electrodes the tunnelling current I results to

$$I \propto \int_{-\infty}^{\infty} |M(E)|^2 \cdot \rho_{\mathrm{tip}}(E - eU) \cdot \rho_{\mathrm{sample}}(E) \cdot \Big[f(E - eU) - f(E) \Big] \mathrm{dE}, \tag{2.4}$$

where $f(E)$ is the Fermi function, $M(E)$ the tunnelling matrix element, U_{Bias} the Bias Voltage, ρ_{tip} and ρ_{sample} are the density of states of the tip and the sample, respectively, and E is the energy of the respective states [59].

A simple theory for the case of the STM was developed by J. Tersoff and D. Hamann [60, 61], where an s-orbital is assumed to be the tunnelling tip and the voltage U is chosen

to be small compared to the work function of the sample. For this case the tunnelling current results to

$$I \propto U \cdot \rho_{\mathrm{tip}}(E_{\mathrm{F}}) \cdot \rho_{\mathrm{sample}}(\mathbf{R}_{\mathrm{tip}},E_{\mathrm{F}}). \tag{2.5}$$

Here, $\rho_{\mathrm{tip}}(E_{\mathrm{F}})$ and $\rho_{\mathrm{sample}}(R_{\mathrm{tip}})$ are the density of states of the tip and of the sample surface at the center $\mathbf{R}$ of the tip orbital and at Fermi energy. This means that the STM does not image the atoms but the electronic density of states at the sample surface near the Fermi energy. However, in case that the bias voltage is not small compared to the work function this theory must be extended and yields in the simplest extension

$$I \propto \int_{E_{\mathrm{F,tip}}}^{E_{\mathrm{F,tip}}+eU} \rho_{\mathrm{tip}}(W)\rho_{\mathrm{sample}}(E+eU)T(W,U)\mathrm{dW}, \tag{2.6}$$

where $T(W,U)$ is the transmission coefficient. Hence, the tunnelling current is composed of the integrated density of states in the energy range from E_{F} to $E_{\mathrm{F}} + eU$.
In scanning tunnelling spectroscopy (STS) the density of states of the sample is measured, which is extracted by utilising the lock-in technique, where the derivative of the measured signal is recorded. For the case of a constant density of states and a constant transmission coefficient within this energy range Equation 2.6 results to

$$\frac{\mathrm{dI}}{\mathrm{dU}}(U) \propto \rho_{\mathrm{sample}}(U) \tag{2.7}$$

and leads to the density of states of the sample for the applied bias voltage U, meaning that the spectroscopy signal indeed is approximately proportional to the density of states of the sample. The energy resolution ΔE is given by the expression

$$\Delta E = \sqrt{(3.3 \cdot k_B T)^2 + (2.5 \cdot eU_{\mathrm{mod}})^2}, \tag{2.8}$$

where k_B is the Boltzmann constant, T the temperature, and U_{mod} the amplitude of the modulation voltage of the lock-in amplifier [62]. Spectroscopy can be performed on single positions sweeping the bias voltage in order to get a spectrum of the local density of states in dependence of the energy. Moreover, while the topography represents the integrated density of states spectroscopy map reveal the lateral distribution of the state for the applied bias voltage within the energy resolution shown in Equation 2.8.

PART III

Experimental

CHAPTER 3

The Scanning Tunnelling Microscopy Apparatus: LT-STM

The LT-STM apparatus is a commercial system that mainly was brought into service during this work by me with the help of M'hamed Rabie Djemour and Fabian Craes. Parts of this apparatus as well as additional instruments were built up or upgraded during this work. The sample carrier plate in the load-lock was upgraded in cooperation with Fabian Craes and Jürgen Klinkhammer. The metal shield for evaporation experiments was built up by Fabian Craes and Jürgen Klinkhammer according to my planning. The electrical and thermocouple contacts at the manipulator as well as the electron beam sample holder were upgraded and an alkali evaporator was built up by me. The gas supply lines for hydrogen, water, ethene, and oxygen was managed and partly built up by me. The change of the vibration isolation was planned by me and carried out in cooperation with Jürgen Klinkhammer.

The low temperature scanning tunnelling microscopy apparatus LT-STM[1] was used for all own STM and STS measurements presented in this work. A schematic drawing of the setup is shown in Figure 3.1. The whole apparatus is bedded on four **vibration isolator feet**[2] with a resonance frequency of 1 Hz (vertical) and 1.5 Hz (horizontal) [63] in order to decouple the system from vibrations of the building. The vibration isolation was changed during this work. The upgrades are described in section 3.5.
The apparatus consists of three chambers [Fig. 3.1(a)]. A load-lock enables quick and easy loading of samples, which can be prepared in the preparation chamber. In order to have always clean conditions at the STM it is mounted in a separate chamber, namely the STM-chamber, at a liquid helium bath cryostat [Fig. 3.1(b)]. Details about the setup are presented in this section. For completeness the whole setup will be described in the

[1] LT-STM, SPS Createc GmbH
[2] S-2000 Stabilizer^{TM} Vibration Isolators, Newport Corporation

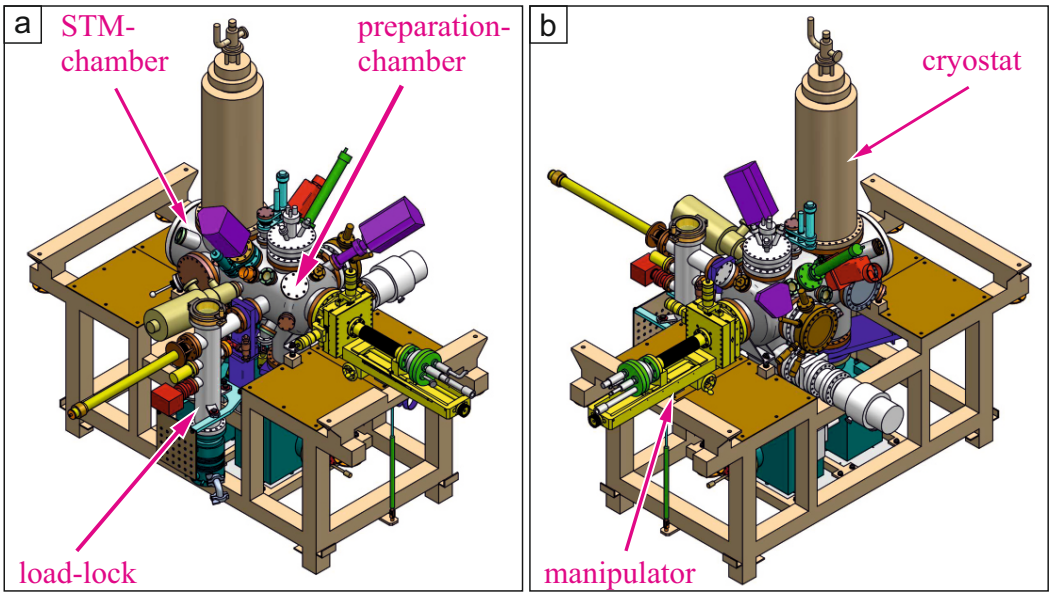

Figure 3.1: Schematic drawing of the LT-STM apparatus. Image reprinted with permission from Createc GmbH.

following, focused on the parts used for this work, especially if they were upgraded by me. Details about the upgrades and self-built parts are explained in section 3.5.

3.1 The Sample Holders

Several types of sample holders for different types of samples are commercially available. All sample holders consist of a copper body and a contact plate. The body is modified for the different types of samples that can be mounted. The original contact plate is made out of an aluminium oxide (Al_2O_3) plate which has electrodes deposited onto it. The top electrode material is silver in order to enable soldering with UHV compatible solder. Due to problems that occurred during soldering and to the limitation to four contacts on the manipulator site the plate was redesigned. Details about this upgrade can be found in section 3.5.

Figure 3.2 shows the sample holders used in our lab. A **wafer sample holder** (a) can be used to prepare e.g. silicon wafers utilising resistance heating by applying a current directly through the wafer. For preparing two wafers on the same sample holder a **dual sample holder** (b) is also available. Hat-shaped metal samples can be prepared on the **metal sample holder** (c), where the sample is clamped directly onto a resistance heating by a molybdenum clamp. By this a sample temperature of about 1200 K can be reached, measured by a type-K thermocouple that is fixed under the clamp. For preparation

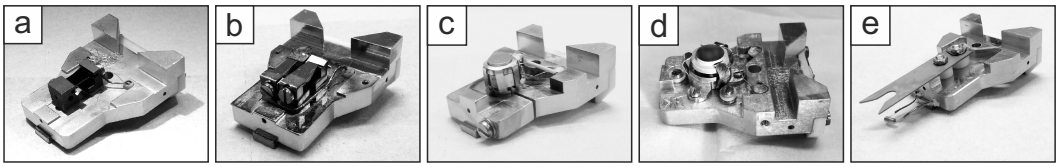

Figure 3.2: Photographs of the sample holders used at the LT-STM apparatus. Wafer samples can be mounted on a wafer sample holder (a). There is also a version for two wafers on the same sample holder - the dual sample holder (b). For metal samples and preparation temperatures below 1300 K the metal sample holder (c), for higher temperatures the e-beam sample holder (d) can be used. Tip exchange in the STM is performed by using the tip tool (e). This version is upgraded with a heating filament [64].

of metal samples at higher temperatures the **electron-beam sample holder** (d) can be used. By applying high voltage between the filament and the sample temperatures even higher than 1600 K can be reached easily. During flash annealing the chamber pressure rises to about 1×10^{-9} hPa. The sample temperature is measured via a type-K thermocouple wires that are inserted into two sidewise holes of the sample or spot-welded, if no holes are present. More details about the e-beam sample holder can be found in section 3.5.

In order to change a tip in the STM a **tip tool** (d) is available. This tip transfer tool has an additional filament for flash annealing of carried tips mounted below the fork. The upgrade of this tip tool was carried out by Jürgen Klinkhammer during his doctoral studies [64].

3.2 The Load-lock

Samples can be loaded through a **quick-close viewport**[3] onto a sample carrier plate, which is mounted on a transfer rod. The carrier plate was redesigned in the past in order to be able to load two samples at the same time as well as to load and transfer the tip tool. Details about this can be found in section 3.5. The chamber pressure is measured by a **wide range pressure gauge**[4]. The base pressure of the load-lock is in case of a baked load-lock about 8×10^{-10} hPa and in the range of 7×10^{-8} hPa unbaked. A quick bake-out of the load-lock can be done utilising a **bake-out lamp**. Hereby the time for heating up the load-lock is 30 min, the cool down usually takes 2 h. The final pressure after the quick bake-out is in the lower 10^{-9} hPa range, therefore the load-lock is baked typically

[3] CF-Schnellschlusstür mit Sichtfenster, VAb Vakuum GmbH
[4] Atmion^{TM}, Vacom GmbH

over night by the common method using heating belts. The load-lock is evacuated by the use of a **Turbo-molecular pump**[5] connected upstream of a **membrane pump**[6].

3.3 The Preparation Chamber

The heart of the chamber is the **manipulator**[7] [see Fig. 3.1(b)] with four degrees of freedom, which is shown in Figure 3.3. It can be moved in three translational directions as well as be fully rotated along its axis. Sample holders can be grabbed via a translator that pulls a T-shaped part to the copper counter part and thereby presses the sample holder against the head (see Figure 3.3). This enables sufficient heat transfer to the actively cooled manipulator in order to avoid heating up of the sample holder during preparation. The active cooling is done by a **helium flow cryostat**[8] that can be cooled by liquid helium and liquid nitrogen as well as by pressurised air. A resistance heating is integrated for annealing the manipulator head and the grabbed sample holder. A silicon diode is mounted for temperature control at the manipulator head. By default temperatures up to 1300 K can be reached, but not all modifications at the head can stand that high temperatures. Especially the soldering of the temperature diode is a weakness as it melts at 494 K. Therefore the manipulator heating should not be used for standard preparations, also because the chamber pressure increases even to the 10^{-8} hPa range due to the high temperatures of the parts at the head. In fact, in case the usage of the heating is indispensable temperatures above 450 K should be avoided.

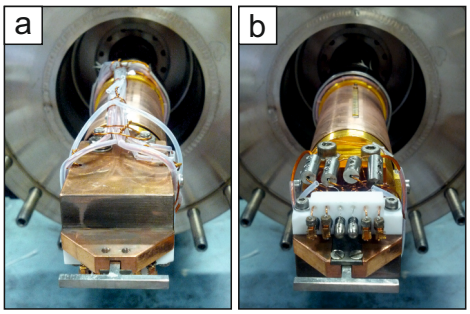

Figure 3.3: The head of the manipulator at LT-STM. Top view (a) and bottom view (b) of the upgraded manipulator. The T-shaped part is used for grabbing samples by pressing them against the copper block. Six individual contacts are used for contacting the sample holder. More details about the upgrade are in section 3.5.

A view into the preparation chamber is shown in Figure 3.4, where the pink arrows indicate the view to the centre through view ports. A **Knudsen cell**[9] (1) for evaporation of gadolinium is mounted behind a valve. This enables easy reloading or changing the

[5] TurboDrag Pump HiPace 300, Pfeiffer Vacuum
[6] MD4, Vacuubrand GmbH
[7] PM 25-400, VAb GmbH
[8] HVK-St, VAb GmbH
[9] WEZ40-20-16-KS, Dr. Eberl MBE Komponenten GmbH

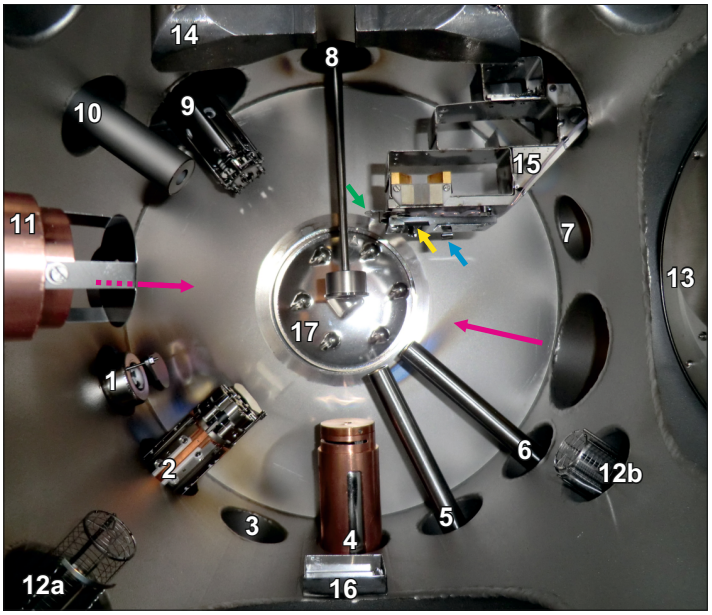

1 Knudsen cell
2 e-beam evaporator
3 alkali evaporator slot
4 Eu evaporator
5 water inlet
6 gas inlet
7 evaporation shield
8 quartz crystal balance
9 mass spectrometer
10 ion gun
11 HABS
12 pressure gauges
13 LEED
14 magnet yokes (MOKE)
15 sample storage
16 UHV trash can
17 gate valve

Figure 3.4: Photograph from the manipulator flange into the preparation chamber. View-ports enable direct view onto the sample within the evaporator plane during preparation as indicated by the pink arrows. On the left the view-port is partly masked by the HABS (11). Short arrows mark positions of parts mounted under the sample storage (green: filament, yellow: blade, blue: ground contact). Image reprinted from [64].

instrument without breaking the vacuum. A **four pocket electron beam evaporator**[10] (2) with two moveable and two fixed pockets is mounted for evaporation of metal targets from rods and from crucibles, respectively. A home-built **alkali evaporator** is mounted at the position (3) which is described in section 3.5. The **low temperature effusion cell**[11] (4) is used for europium evaporation. Gold covered **gas dosing tubes** for water (5) and ethene (6) are connected via leak valves to the gas supply lines. For the water inlet two leak valves are mounted in series with a **spinning rotor gauge**[12] in between. Thereby the enclosed volume can be filled with a precise amount of water molecules which can be dosed to the sample surface via the dosing tube.

The free slot (7) is used for a home-built **evaporation shield**. Utilising a linear shift a horizontally aligned metal plate can be moved close to the common sample preparation position. After that the sample can be moved behind this shield and moved into the evaporation beam by z-translation of the manipulator. Optical control of the exact position of the sample with respect to the deposition edge is achieved by a camera mounted behind the view-port on the left hand side of Figure 3.4 marked by the pink arrow.

[10] EBE-4, SPECS GmbH
[11] NTEZ 40-2-16-KS-2007849, Dr. Eberl MBE Komponenten GmbH
[12] Spirotorr^{TM} SVG 1 vacuum gauge, SAES Getters

Evaporation rates can be determined by material deposition onto a **microbalance**[13] (8). It is fixed on a linear shift in order to be able to move it to the sample position for rate determination. A **mass spectrometer**[14] (9) is mounted in order to analyse the residual gas of the chamber as well as the partial pressure of a selected gas like ethene or oxygen. For ion bombardment of the sample a differentially pumped **ion gun**[15] (10) is mounted. By a **hydrogen atom beam source (HABS)**[16] (11) a beam of atomic hydrogen can be dosed to the sample surface. The chamber pressure is determined by a Bayard-Alpert **pressure gauge**[17] (12a). A spare pressure gauge is also mounted at position (12b).

The **microchannel plate LEED**[18] (13) allows LEED measurement of beam currents in the regime of nano-amps so that also insulating samples can be investigated. The yoke of the electromagnet (14) enables magnetisation of the sample. It is part of a home-built setup for magneto-optical Kerr effect measurements(**MOKE setup**) that was built up by Jürgen Klinkhammer and is described in detail in his PhD-Thesis [64].

The **sample storage**[19] (15) can be loaded with up to five sample holders and up to six tip holders. A filament is mounted under the storage and can be used for tip annealing by moving the tip into the glowing filament loop (green arrow). By applying negative high voltage to the tip even very high temperatures can be reached. A crystal blade (yellow arrow) is also mounted under the storage for cleaving crystals by pressing the sample edge against the blade. The upper (and unusable) part from cleavage can be dumped to the UHV trash can (16).

An **integrated gate valve** (17) separates the STM-chamber from the preparation chamber leading to continuously clean conditions at the STM during sample preparation. The preparation chamber is pumped by a **turbo-molecular pump**[20] upstream of a **rotary pump**[21]. An adsorption trap[22] prevents backstreaming of oil vapor between rotary pump and turbo-molecular pump. In addition an **ion pump**[23] with an integrated **liquid nitrogen cooling** and a **titanium sublimation pump**[24] are used for keeping vacuum, especially during STM experiments when turbo-molecular pumps are switched off.

[13] Quarz Crystal Balance, Sycon Instruments; In-vacuum Sensor: VSO-100
[14] QMS 200, Pfeiffer Vacuum
[15] IQ 10, Kremer Vakuumphysik
[16] HABS-40-A-2104840, Dr. Eberl MBE-Komponenten GmbH
[17] UHV 24, Varian Vacuum Technologies
[18] BDL 800 IR-MCP2-LMX-ISH, OCI Vacuum Micrengineering Inc.
[19] SPS CREATEC GmbH
[20] TMU 521 P, Pfeiffer Vacuum GmbH
[21] Trivac D1, 6B, Leybold Heraeus GmbH
[22] Absorptionsfalle, Leybold GmbH
[23] TiTan^{TM} 300TV, Gamma Vacuum
[24] Subli-con 51, Vacom GmbH

3.4 The STM Chamber

The base pressure of the STM chamber is below 10^{-10} hPa. It is measured by a **Bayard-Alpert pressure gauge**[25]. In case that the cryostat is cooled down residual gas molecules in the chamber adsorp on the cold surfaces leading to a drop of the base pressure to values below the detection limit. The vacuum is generated by an **ion pump**[26] with an integrated **liquid nitrogen cooling** and a **titanium sublimation pump**[27]. The chamber is equipped with a **bath cryostat**[28], consisting of an inner cryostat for liquid helium (4 l), an outer one for liquid nitrogen (15 l), and an actively nitrogen cooled radiation shield. A **liquid helium level meter**[29] measures the helium level by pulsed current measurements through a superconducting probe wire. A **liquid nitrogen level meter**[30] determines the filling by a capacity measurement of two concentric metal tubes due to the difference in capacity of a filled and an empty probe. The liquid helium lasts for about 70 h so that refilling is only necessary every three days whereas the liquid nitrogen lasts for about 50 h, but can be refilled automatically by the electronics of the level meter. Therefore manual refilling is not necessary during e.g. weekends.

The **Besocke-beetle-type STM** is mounted below the inner cryostat by coil springs in order to decouple the STM from vibrations of the apparatus. An eddy current brake serves as a damping for the free-hanging STM. This damping system enables STM measurements with atomic resolution even when the system is not vibration isolated via the external vibration isolator feet and while the turbo-molecular pumps are running, but with a very high hum and noise level. Nevertheless, the image quality from measurements, where the pumps are still running lasts for test measurements e.g. to check, if a preparation did work. The STM is surrounded by a radiation shield, which has a gate for sample transfer. Two viewports are mounted in the radiation shield: one for optical control during the sample transfer and one for optical control of the tip positioning on the sample. The STM can be cooled down to about 5.3 K, and be set to a desired temperature by counter-heating via a Z-diode during cooling. A **leak valve** is mounted in front of an additional gate that is connected to a hydrogen supply line in order to be able to dose hydrogen directly to the sample even while measuring with the STM.

[25] UHV 24, Varian Vacuum Technologies
[26] TiTan^{TM} 300TV, Gamma Vacuum
[27] Subli-con 51, Vacom GmbH
[28] UHV He bath cryostat, Cryovac Gesellschaft für Tieftemperaturtechnik mbH
[29] HLG 200, Wessington Cryogenics
[30] SPS Createc GmbH

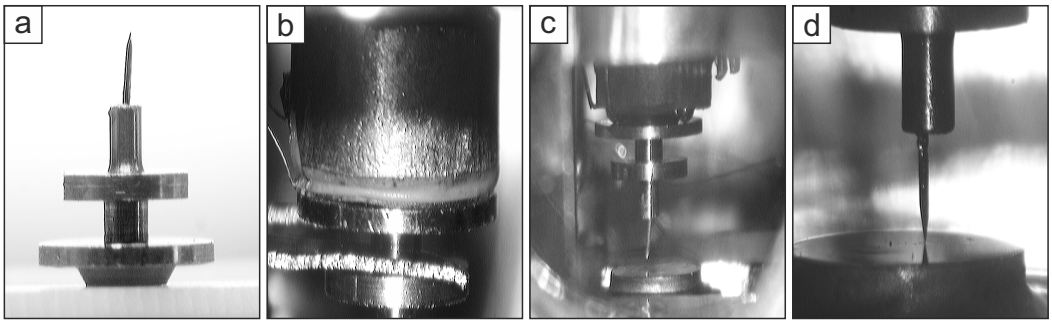

Figure 3.5: STM tip holders. The tip is mounted in a magnetic tip holder (a). By the fork of the tip tool it can be inserted upside down into the scanner (b). A tip approach is shown in (c) where the reflection of the tip on the sample surface can be used for coarse approach. Positioning of the STM tip can easily be done (d).

For STM measurements home-made **tungsten tips** were used, which were produced following the procedure described in [64]. The tips are mounted in a tip holder as shown in Figure 3.5(a). The tip holder can be picked up by the fork of the tip tool [see Fig. 3.2(d)] and set in upside down into the scanner [see Fig. 3.5(b)]. The optical control of the tip exchange is done by the usage of a **microscope** with a **camera** attached to it. Note that Figure 3.5(b) shows an old version of the scanner with a planar arrester. It was switched to a version with three spheres [see Fig. 3.5(c)] in order to avoid possible wobbling of the tip holder through small imperfections in the arrester plane. A coarse approach of the STM tip can be done by utilising the reflection of the tip on the sample surface [see Fig. 3.5(d)]. The reflection also enables lateral positioning with high accuracy by the microscope. In order to avoid mechanical shocks (e.g. by touching the setup) during a change of the tip position to reach a different sample area the camera as well as the **cold-light source**[31] can be turned on and off by a remote switch.
A **Preamplifier**[32] converts the tunnelling current to a voltage signal measured by the STM electronics. For spectroscopy measurements a **Lock-In amplifier**[33] is used.

3.5 Self-Built Parts and Upgrades

During this work the vibration isolation, the manipulator contacts as well as the contact plate for the sample holders, and the loading plate in the load-lock were upgraded. Also an alkali evaporator and an e-beam sample holder were built-up. Details about this are presented in the following.

[31] Kaltlichtquelle KL 200, Schott AG
[32] LCA-4K-1G (ultra low-noise); DLPCA-200 (variable gain), Femto Messtechnik GmbH
[33] SR 830, Stanford Research Systems

Upgrade of the Vibration Isolation

At the beginning the vibration isolation of the system was implemented by steel springs with one end fixed at the ceiling and the other end fixed to the frame of the LT-STM apparatus in order to decouple it from mechanical vibrations of the building. But as evaporation of the cooling liquids inside the cryostat leads to a shift of the centre of mass of the setup it had to be realigned before and also during the experiments in order to avoid short circuits between the free-hanging STM and the cryostat heat shielding. Therefore the vibration isolation was changed to the common version where the setup is bedded on top of four vibration isolator feet with a resonance frequency of 1 Hz (vertical) and 1.5 Hz (horizontal) [63]. The floating screed is removed at the positions of the feet so that they are standing directly on the sub-concrete to gain enhanced decoupling from vibrations e.g. by walking persons in the corridor. The isolation is achieved by an balloon-like volume filled with pressurised air which lifts the setup by about 6 mm. The high mass of the setup is the main factor of vibration isolation as the vibration amplitude is heavily reduced due to mass inertia of the setup. A diaphragm inside the air-filled volume leads to laminar flow between two separated regions and thereby induces damping. Automatic levelling is done by an adjusted cantilever at each foot that opens a valve for pressurised air to the air-filled volume (or release pressure) until the desired height is reached.

Upgrade of the Loading Plate

Sample holders can be loaded onto the sample loading plate in the load-lock that is depicted in Figure 3.6(a). The transfer rod is moved to the right hand side for transferring sample holders to the preparation chamber. Two upward standing pins (indicated by the white arrows) serve as holders to avoid samples to fall off the loading plate by putting the central hole inside the body over the pins. The sample holders are oriented with the contact plate pointing to the lower edge of the image. Also the tip tool can be transferred. In this case no additional sample holder can be loaded to the plate, because the tip tool has to be rotated counter-clockwise on the plate as shown in Figure 3.6(b). This ensures safe transfer as the tip tools cross section is reduced which is critical for transferring from/to the preparation chamber through the gate valve. By the use of the manipulator and careful movement of the transfer rod the tip tool can be rotated in the right orientation for grabbing it by the manipulator and vice versa.

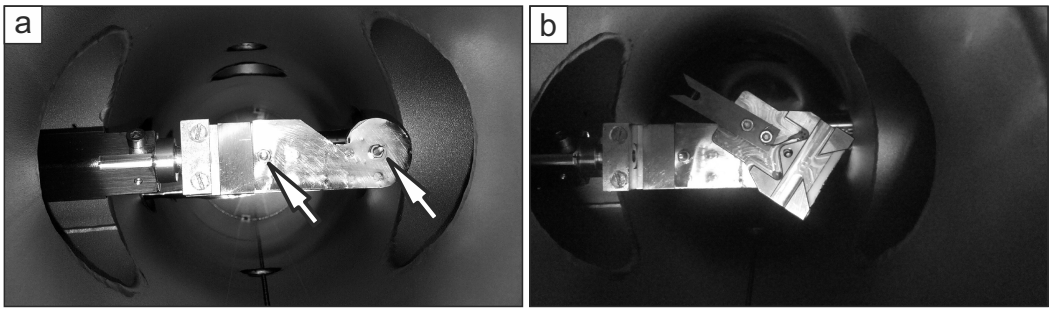

Figure 3.6: View into the load-lock. Two upward standing pins indicated by the arrows (a) allow safe loading of two samples at the same time. The tip tool can be rotated in order to fit through the gate valve to the preparation chamber (b).

In the previous version loading two samples at the same time or a rotation of the tip-tool on the loading plate was not possible. Therefore the upgrade leads to a more comfortable usage for loading sample holders as well as a higher safeness for loading the tip tool.

Upgrade of the Manipulator

The contacts of the manipulator were redesigned during this work as problems with the temperature reading and fragility of the previous contacts occurred. Both versions can be seen in Figure 3.7. The old version of the contacts were made out of CuBe springs that press against the contact plate of the sample holder as depicted in Figure 3.7(a). Several times it happened that some of the contacts did not touch the sample holder contacts anymore [see Fig. 3.7(b)]. Therefore the old contact springs were changed to a version with six individual contacts: four laminated contacts and two rounded rods as shown in Figure 3.7(c) that are pushed in the direction of the sample holder contact plate by hand-made tungsten coil springs as can be seen in the drawing in Fig. 3.7(c). The block in which the contacts are inserted is made out of MACOR that is mounted under the manipulator head [Fig. 3.7(d)] at the same position like the old version. In the topview [Fig. 3.7(e)] the laminated contacts are presented in detail. A terminal stop made out of a screw inside the rods on the backside of the MACOR block guarantees that the outermost end of the contacts is always at the right position. The thermocouple contacts are made out of thermocouple material (Chromel and Alumel) and the electrical contacts out of stainless steel gibs with copper-beryllium laminated contacts screwed on. Also the electrical contact by a copper wire is screwed onto the gibs and connected via lustre terminals to the electrical feedthrough of the manipulator [see Fig. 3.7(e,f)].
The upgrade of the manipulator head enhanced not only the robustness of the contacts. It enables precise temperature measurements at the sample position as the new version

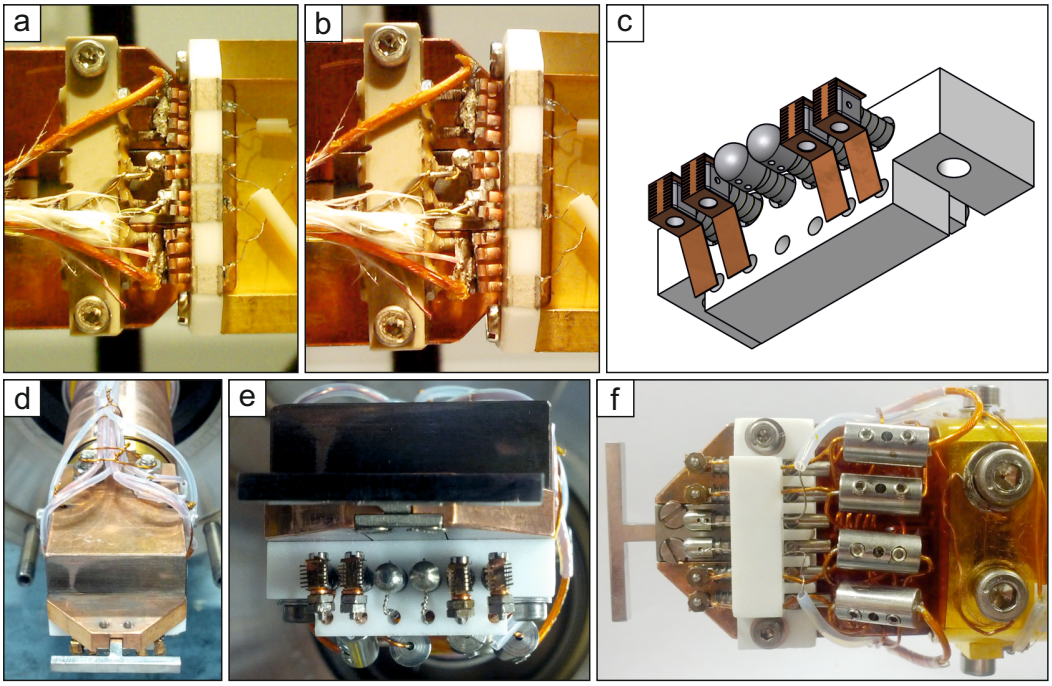

Figure 3.7: Upgraded manipulator contacts of the LT-STM apparatus. In the old version the sample holder contact plate is pressed against the CuBe springs (a). Several times some of the springs lost contact (b). The new version of the contacts is made out of laminated contacts screwed onto steel gibs and pins made out of type-K thermocouple material (c) mounted in a MACOR block. Hand-made tungsten coil springs press the contacts in the direction of the contact plate. Cabling of the contacts is made by screwing the copper wire to the electrical contacts and twisting the thermocouple that is feed through the holes in the pin. Cables are guided through the holes below the gibs. The MACOR block is mounted under the manipulator head (d). The cables are mounted on a cable bridge in order to avoid contact to the manipulator heating (upper part). The six individual contacts can be seen in detail (e). The contacts are fixed inside a MACOR block with a screw used as fence and pressed in the direction of the sample holder by tungsten coil springs as seen in the bottom view (f). Four lustre terminals are used to connect the electrical contacts to the manipulator wiring, thermocouple wires are twisted at the gibs and spot-welded to the manipulator wiring.

is continuously made out of thermocouple material. The accuracy of the temperature reading was proven by a test measurement with a reference thermocouple feedthrough. To both thermocouple wires at the sample holder an additional wire of exactly the same material was spot-welded and connected to the reference feedthrough. During the test measurements all possible combinations of cooling and heating of the sample, with and without heating of the manipulator head, and with and without cooling of the whole manipulator by liquid helium were tested in order to get all possible combinations of temperature gradients along the manipulator head. The calibration of the measured

temperature at the manipulator as well as at the reference was always identical, meaning that the measurement was exact within the precision limit of a thermocouple.
Nevertheless the measured Curie-temperature from a MOKE experiment did not fit to a calibration by a SQUID (superconducting quantum interference device) measurement [64]. This is not surprising as the temperature measured by the thermocouples is an average temperature measured inside the crystal while the sample surface was at Curie-temperature. And as the thermocouple can not be mounted on the surface this is a systematic error that can not be avoided for samples designated for STM experiments.

Upgrade of the Contact Plate

The original contact plate is made out of an aluminium oxide (Al_2O_3) plate on which electrodes are deposited as depicted in Figure 3.8(a,b). One side of the contact plate points to the manipulator (manipulator-side: Fig. 3.8a) and the other one to the STM (STM-side: Fig. 3.8b) when mounted at the sample holder. The manipulator-side contains four contacts where the outer ones have a larger area in order to have more CuBe springs from the manipulator in contact to it. By this the maximum current that can be applied is doubled compared to the smaller ones. All contacts from the manipulator-side are passed to the STM-side, where the outermost contacts are typically used for the heating current at the sample holder as they can stand higher currents due to the larger area on the other side. The central contacts are used for measuring temperatures by soldering thermocouple wires to it at the STM-side. The second and fifth contact can be used inside the STM as e.g. a probe for the bias voltage.
For various reasons the contact plate was redesigned. As the silver layer from the contacts several times was soaked into the solder ending up in contacts that could not be soldered anymore, the contacts were changed to CuBe foils enabling spot-welding of the wires to it.

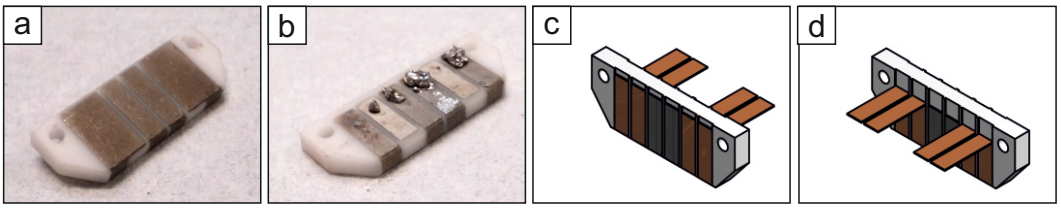

Figure 3.8: Photographs of the contact plate. The old version (a,b) was made out of Al_2O_3 with contacts deposited onto it, whereas the new one is made out of MACOR with foils pulled over the body that serve as contacts. The manipulator-side has four contacts for the old version (a), the new version has six contacts (c). At the STM-side both versions have six contacts (b,d). The foils are bent to enable spot-welding of wires to it (d).

This leads also to a higher thermal stability of the contact as the UHV-compatible solder melts at about 490 K. Another reason was that the inner contacts for the temperature reading were not made out of thermocouple material. Therefore the new contact plate, which is made out of a MACOR body, contains six individual contacts as depicted in Figure 3.8(c,d).
The two electrodes in the middle are made out of foils from type-K thermocouple material while the other four contacts are made out of CuBe foils. Each pre-bent foil is pulled over the deepening in the body that guarantees electrical insulation between the contacts. The larger contacts like for the old version [Fig. 3.8(a,b)] is not necessary anymore as the manipulator contacts are now laminated ones, thus having more contact points for each laminated contact than for the manipulator version with CuBe springs.
In combination with the upgrade of the manipulator all six contacts can be used also during preparation. Therefore this upgrade leads to more stable contacts to the wires at the sample holder as well as an increase of the number of usable contacts during preparation. Hence an additional ground contact can be applied to the sample during preparation which does not create short circuits in the STM. Also the emission currents during e-beam heating can be measured as well as the ion current during sputtering.

The Electron Beam Sample Holder

For metal samples that need annealing temperatures higher than 1200 K during preparation the **electron beam (e-beam) sample holder** is used, which was upgraded during this work. It can be seen in Figure 3.9. The temperature is measured utilising two thermocouple wires (type K) which are inserted into two sidewise holes of the sample, measuring the average temperature inside the sample. The sample can be heated by thermal radiation from the glowing filament[34] to temperatures of about 500 K and higher. In case that the manipulator is cooled by liquid helium sample temperatures up to room temperature can be reached by thermal radiation. By applying high negative voltage to the glowing filament, emitted electrons can be accelerated to the sample and the heating power is increased by the electrical power that is applied. This way temperatures even higher than 1600 K can be reached easily.
The top view [Fig. 3.9(a)] shows the sample that is clamped by three tungsten springs onto sapphire balls each laying in a deepening of the outer cylindrical molybdenum pod [Fig. 3.9(b)]. The inner molybdenum cylinder is mounted on an insulating Al_2O_3 rod and serves as a Wehnelt cylinder due to charging of the electrically insulated cylinder.

[34] WRh alloy, diameter 0.125 mm, maximum current 1.80 A

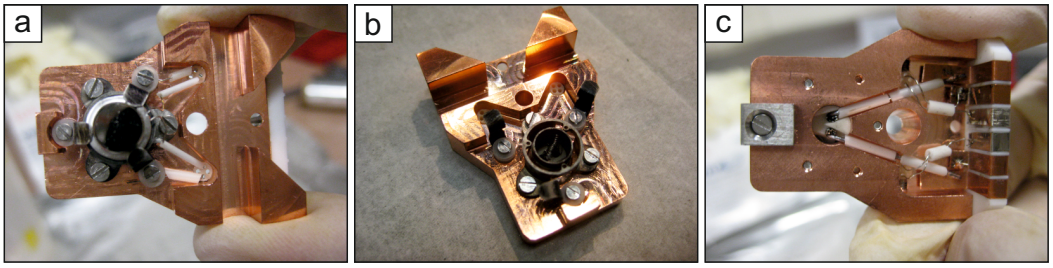

Figure 3.9: Photographs of the redesigned e-beam sample holder. Top view with (a) and without (b) mounted sample. The filament is located in the Wehnelt cylinder which is surrounded by a cylindrical pod (b). The three tungsten springs press the sample against underlying sapphire balls that rest on the pod. The bottom view (c) shows the new version of the contact plate with six individual contacts. The outer contacts are spot-welded to insulated Ta wires in Al_2O_3 tubes, that are connected to the filament, the inner ones are thermocouple contacts. The other contacts are used for grounding the sample.

Therefore all electrons emitted from the filament are accelerated to the sample only as this is the only surface on lower potential than the filament - except for a very small portion of electrons that can escape through the very small gap between sample and Wehnelt cylinder to the chamber walls that are on ground potential as well.
The bottom view [Fig. 3.9(c)] shows the cabling of the filament through Al_2O_3 tubules to the contact plate on the right hand side. Wires to the filament are spot-welded to the outer contacts, the thermocouple wires to the inner ones. The inner CuBe foils are used for contacting the sample in order to ground it e.g. via a multimeter. By this the temperature reading is not disturbed as the sample does not get charged. In addition an ion current to the sample can be measured via this contacts.
The advantage of the e-beam sample holder is not only the higher temperature that can be reached but also a very low heat-up time of about 25 s for a flash anneal temperature of 1500 K. Therefore the body does not heat up as much as by slow heating. Hence the pressure during a flash annealing is just in the range of 1×10^{-9} hPa or even below. The additional contacts of the contact plate enable measuring the temperature via the thermocouple during e-beam heating of the sample. During this also the emission current can be measured as well as an ion current during ion bombardment of the sample.

The Alkali Evaporator

Three alkali dispenser[35] are mounted on a four-fold electrical feedthrough that was mounted inside-out on a linear translational bellow as shown in the top view [Fig. 3.10(a)]. A hole

[35] Alkali Metal Dispensers with terminals, SAES Getters Group

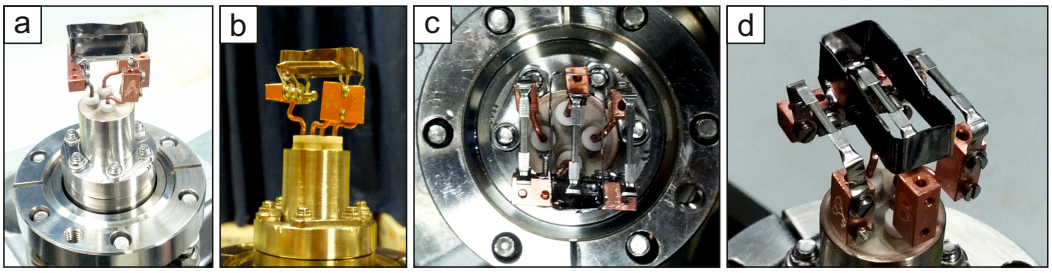

Figure 3.10: Photographs of the home-built alkali-evaporator. Overview (a) and side view (b) of the top parts of the evaporator that are mounted directly on an electrical feedthrough in an inside-out version. The central dispenser is surrounded by a shield to avoid heating up neighbouring dispensers during evaporation by thermal radiation. The top view (c) shows the alkali dispensers that are mounted centrally of the translator axis. All disperser have one lustre terminal in common, the other electrode of each dispenser is mounted to an individual terminal as shown in the side view (c,d).

drilled into the electrodes of the dispenser is used to screw one side of the dispenser to one of the three individual lustre terminals. The other side is screwed to one commonly used lustre terminal. Alkali atoms are evaporated by a current flowing through the dispenser that induces a temperature driven chemical reaction dissolving alkali atoms. By the three individual contacts it is possible to use each dispenser with different evaporation rates at the same time. A molybdenum foil serves as a radiation shield which is mounted around the middle dispenser. Hence warming up of neighbouring dispenser by thermal radiation is avoided which could lead to an inadvertent alkali evaporation as the vapour pressures of alkali metals is rather high even at moderate temperatures.

CHAPTER 4

The Beamline ID-32

The prearrangements of the experimental work for the beam times were mostly done by me. On site assembling was also mostly done by me with assistance of Chi Võ Văn. The caesium evaporator was built on site by me. I did not take part in the beam time with the iridium cluster experiments, but analysed parts of the data.

The beamline ID32 at the European Synchrotron Radiation Facility (ESRF) consists of two optics hutches with monochromators and post-monochromators, and two experimental hutches equipped with a diffractometer and a UHV setup, respectively. For experiments in the UHV experimental hutch a flight tube is set in the first experimental hutch, to keep the beam always in UHV conditions - from the synchrotron ring up to the UHV chamber. As the experiments have been built up in the UHV experimental hutch only, the other hutches will not be explained here.

ID32 is an undulator beamline, which provides photons with an energy between 2.5 keV and 30 keV with an energy resolution of $\frac{\Delta E}{E} = 10^{-4}$ and better [65]. The flux at the sample is about $10^{12}\,\mathrm{s}^{-1}$ to $10^{13}\,\mathrm{s}^{-1}$ at an area of maximum $2\,\mathrm{mm} \times 1\,\mathrm{mm}$ [65], which can be reduced by changing the slit size.

The UHV-system at the ESRF consists of a load-lock for quick sample loading and two main chambers: the preparation chamber and the analysis chamber for XSW measurements.

4.1 The Preparation Chamber

This chamber used for sample preparation provides a base pressure of about 10^{-9} hPa and better. It is equipped with an **ion gun**[1], a commercial rear view **LEED-Optics**[2], **leak valves** as gas inlets, and a **manipulator** with three translational and one rotational degree of freedom.
A heating stage is mounted at the frontside of the manipulator, which allows sample heating to temperatures above 1500 K by electron bombardment. By a commercial **microbalance** the deposited amount of evaporated material can be determined. It is mounted on the backside of the manipulator to avoid deposition of material onto the sample during determination of the atom flux. The sample temperature is measured by a **pyrometer** with a threshold temperature of about 580 K.
Additional equipment was brought from home labs. The gas inlets were used for oxygen and ethene. A commercial high temperature **Knudsen cell**[3] was used for europium evaporation and an **electron beam evaporator**[4] for evaporation of platinum.

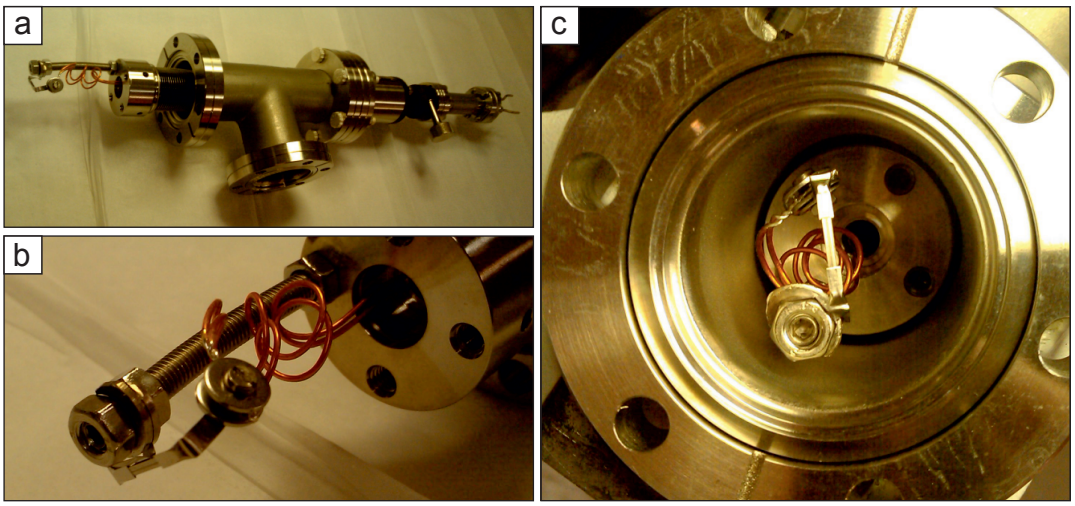

Figure 4.1: Photograph of the Cs evaporator at ID32. The evaporator was built on site. It is mounted on a linear motion bellow (a) and consists of a caesium dispenser that is fixed with one electrode to a thread rod which is on ground potential (b). The other electrode is clamped to wires connected to an electrical feedthrough. The dispenser is mounted in the centre of the translator axis (c).

A **caesium evaporator** was built up on site that is shown in Figure 4.1. The whole evaporator is shown in (a). It has a linear motion bellow in order to be able to move it

[1]SPECS GmbH
[2]SPECS GmbH
[3]HTEZ40-1-19-KS-2005897, Dr. Eberl MBE-Komponenten GmbH
[4]EBE-4, SPECS GmbH

into the preparation chamber after bake-out. One terminal of the **caesium dispenser**[5] is clamped to a thread rod that is grounded by the chamber (b). The other terminal is clamped to wires which are connected to the electrical feedthrough. The dispenser is fixed in the centre of the translator axis (c).

4.2 The Analysis Chamber

For XSW experiments the analysis chamber was used, which has a base pressure of about 5×10^{-10} hPa. It is equipped with a manipulator with three translational and two rotational degrees of freedom. A commercial hemispherical **electron analyser**[6] with an energy resolution below 15 meV is mounted perpendicular to the incoming photon beam. The photon flux is determined by measuring the drain currents from the sample. At a reflectivity screen the photon flux of the reflected photons is determined this way. Fluorescent paint at the reflectivity screen enables the correct positioning of the sample as one can set the reflection very close to the chamber opening for the incoming beam. This ensures that the photons are at almost normal incidence.

[5] Alkali Metal Dispensers with terminals, SAES Getters Group
[6] Phoibos 225, Specs GmbH

CHAPTER 5

The High Vacuum Growth Chamber

This high-vacuum chamber was used in the past as a test chamber. The upgrade of it was planned by Carsten Busse and me. It was organised by me and largely executed by Takahiro Seo.

The growth chamber is an upgrade of a high-vacuum (HV) test chamber in order to enable graphene production under high-vacuum conditions. The basic chamber is described in section 5.1. All modifications made on the chamber are described in section 5.2. The growth of graphene can thereby investigated by methods that are used in industrial processes while ultrahigh-vacuum conditions are typically used for fundamental research only.

5.1 The Test Chamber

An overview of the chamber is shown in Figure 5.1. The front side [Fig. 5.1(a)] is equipped with a Bayard-Alpert **pressure gauge**[1] and a leak valve. A **mass spectrometer**[2] is mounted at the back side. The vacuum is generated by a **turbomolecular pump**[3] upstream of a **rotary pump**[4]. The base pressure is about 8×10^{-8} hPa, but it can be baked leading to a pressure of about 6×10^{-10} hPa. In general the chamber is used for tests as well as for vacuum annealing of parts that are used in UHV-systems. Vacuum annealing is done by an electron beam heating stage that usually is mounted at the top flange of the setup.

[1] UHV 24, Varian Vacuum Technologies
[2] Quadruvac Q200, Leybold-Heraeus GmbH & CO. KG
[3] Balzers TPU 270, ARTHUR PFEIFFER Vakuumtechnik Wetzlar GmbH
[4] DUO 5, Pfeiffer Vacuum

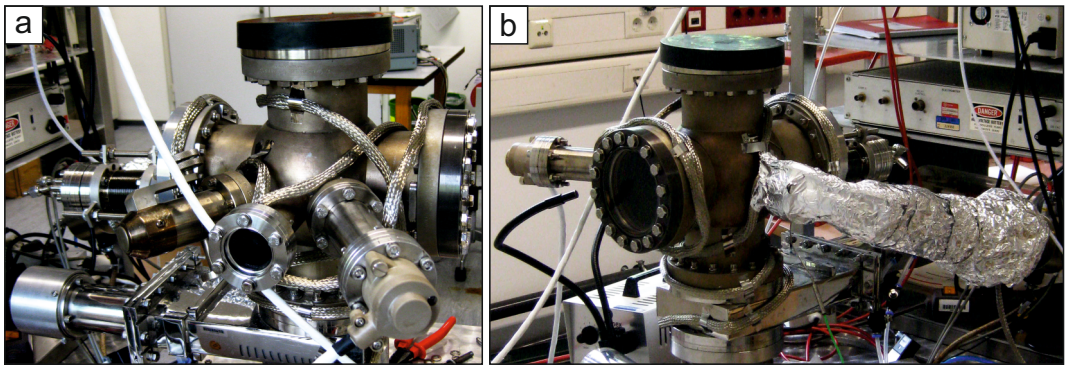

Figure 5.1: Photograph of the high vacuum chamber test chamber. The chamber mostly was used for used for tests of UHV instruments, as well as for vacuum annealing of self-built parts.

5.2 The Upgrade of the Chamber

The upgrade of the chamber includes the gas inlets as well as a facility for sample preparation. In Figure 5.2(a) the upgraded chamber is shown. On the left hand side the gas inlets can be seen. Two leak valves connected for oxygen and ethene gas are mounted at the chamber in order to be able to dose both gases at the same time with different partial pressures. A pyrometer is mounted in order to measure the sample temperature. The sample is mounted on an e-beam sample holder from the LT-STM apparatus, which is clamped to a rod that is fixed to a flange [Fig. 5.2(b)]. The electrical contact to the filament is done via a connector that is pushed over the contact plate containing

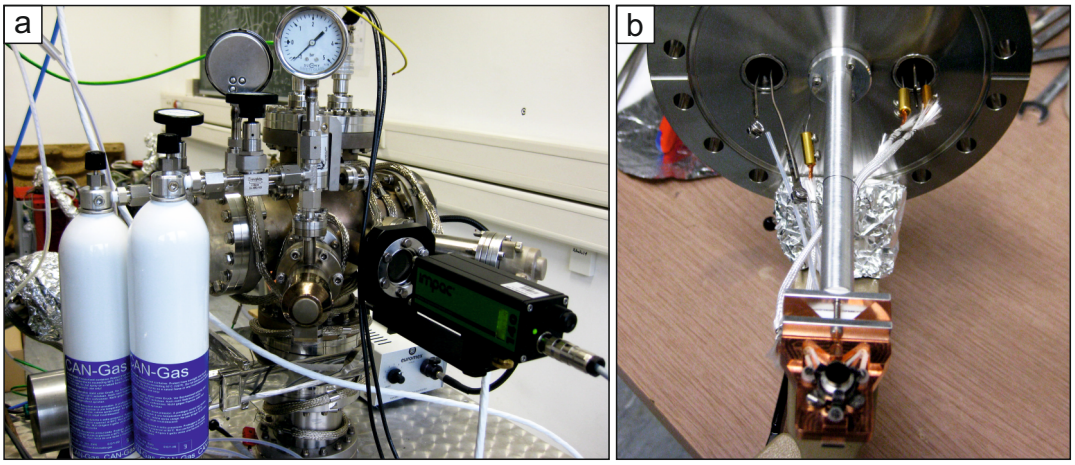

Figure 5.2: Photograph of the upgraded high vacuum chamber. Gas inlets via leak valves for oxygen and ethene are shown on the left. The pyrometer on the right provides an additional way of determining the sample temperature. The sample holder is mounted at the top flange.

thermocouple clamps as well as CuBe-clamps. The sample temperature can therefore be measured by thermocouples and by the pyrometer.

CHAPTER 6

Sample Preparation

The preparation of samples can be split into three different parts: Substrate cleaning, graphene growth, and further treatment like cluster adsorption or intercalation. In section 6.1 the cleaning and growth process is described, the following sections deal with cluster growth and intercalation. As the values for temperatures, pressures, and times vary for different experiments typical parameters are presented in the following. Decisive deviations from these values are given with the respective experiments.

6.1 Graphene Growth

In order to prepare samples with high structural quality an Ir(111) single crystal was cleaned by cycles of ion bombardment with Ar^+ ions at an energy of either 1.5 keV or 2.0 keV and subsequent flash annealing between 1370 K to 1470 K. The cycles were repeated until a LEED image shows the typical hexagonal structure without any superstructure spots to prove cleanness of the surface. Exemplary LEED images are shown in Figure 6.1(a,c).
For STM measurements additional oxygen firing was done at about 1150 K with an oxygen pressure of about 5×10^{-9} hPa for approx. 20 min to make sure that large areas are free of carbon surface impurities on the atomic scale. After the pressure has recovered to the lower 10^{-10} hPa range the sample was flash annealed to 1470 K to remove residual oxygen adsorbates.

TPG steps were performed by adsorption of ethene at a pressure of 10^{-7} hPa to 10^{-6} hPa for 30 s to 60 s. At the LT-STM apparatus the adsorption was performed in front of the gas inlet which boosts the gas dosing by a factor of 85 ± 10 [64]. After adsorption the sample

was flash annealed, mostly to temperatures between 1120 K and 1470 K, depending on the desired island size.

CVD was always done after a previous TPG step. The ethene partial pressure was in the order of 10^{-6} hPa for 5 min. At the LT-STM apparatus this was done with the sample held in front of the gas inlet and a partial pressure of 10^{-7} hPa. Low temperature CVD at 1120 K and also high temperature CVD at about 1400 K were done.

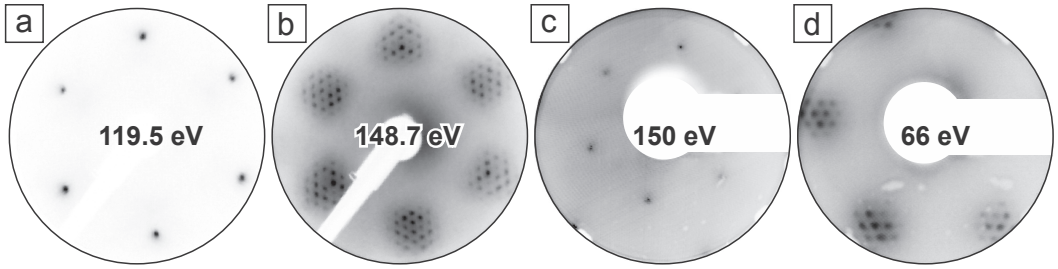

Figure 6.1: LEED images taken at LT-STM (a,b) and at ID32 (c,d). The beam energies are written in the center. Sharp spots related to the Ir(111) surface can be seen (a,c) with high contrast to the background. No additional superstructure spots are visible. In (b,d) Ir(111) related and graphene related spots surrounded by moiré spots are visible. The absence of elongation of the graphene spots along a circle indicates a high quality sample with no indication for rotated grains. Note, that the LT-STM LEED images have higher contrast, esp. for the moiré spots. For image (d) the sample was rotated to show the moiré spots. LT-STM images (a,b) are deskewed.

The processes described above allow for variable graphene coverages. LEED images of graphene samples show Ir(111) related spots as well as carbon related ones. As the carbon related spots are not elongated along a circle it is ensured that well aligned graphene samples were grown. Note that the LEED images taken at the beamline ID32 show less contrast than the ones at LT-STM.
LEED measurements were always performed to test the sample quality. Note, that not all LEED measurements were recorded at ID32 as the required time for this significantly impedes the XSW measurements.

6.2 Graphene Intercalation Compounds

In this section the preparation of graphene intercalation compounds is described. The intercalants used were caesium, europium, and oxygen.

6.2.1 Caesium Intercalated Graphene

Caesium intercalated samples were prepared at ID32 as well as at the LT-STM apparatus by depositing caesium from a dispenser on top of a fully closed graphene layer. The sample was held at room temperature during deposition. A rough deposition rate was determined by a commercial microbalance before starting the deposition. For this the sample needed to be rotated out of the atom beam at ID32. Following this the sample was held into the beam for a preassigned time in order to deposit the desired amount of caesium. At LT-STM the sample was also rotated out of the atom beam for one preparation. Other samples were prepared with the sample partly covered by a metal shield. By moving the manipulator during deposition four areas with different amount of deposited caesium were created.

Note, that from TDS measurements the desorption temperature of the caesium multilayer was found to be 280 K, while for the monolayer of caesium on graphene it is 370 K [66]. In consequence, due to reevaporation the measured rate at the microbalance is not proportional to the real rate. Hence, the deposited amount is given by the deposition time and the current applied to the caesium dispenser. Note, that for the case of a changed dispenser or a different evaporator a new calibration for the deposition has to be performed.

As furthermore the heating of the dispenser via the applied current might change due to heat flow to the support the rate at the beginning of the evaporation was measured to get a rough estimation of the real evaporation rate. This has to be considered in particular for different evaporators, which helps to reproduce the experiments.

6.2.2 Europium Intercalated Graphene

Europium intercalated samples were prepared at ID32 by deposition of europium on top of a fully closed graphene layer. Before deposition the evaporation rate was determined by a commercial microbalance. As the microbalance was mounted at the backside of the manipulator the sample was rotated out of the atom beam for rate determination. During deposition the sample was heated to 670 K in order to evaporate excessive europium from the surface after saturation in the intercalation process. Therefore residual europium on the surface can be ruled out.

6.2.3 Oxygen Intercalated Graphene

The oxygen intercalated sample was prepared at ID32 only. The sample could not be set to a constant and suitable temperature (see section 4.1) as the pyrometer does not allow temperature measurements below roughly 600 K. Furthermore pyrometer measurements are challenging at this temperatures due to diffuse light from e.g. glowing filaments. Therefore a cool down curve was measured, which is shown in Figure 6.2. The sample was flash annealed to 1470 K and the temperature was measured as a function of time. As the manipulator does not stay at constant temperature but heats up an exponential decay formula with just one component is not suitable to fit the data. The heating up of the cooling reservoir can be taken into account by fitting the data to a two component exponential decay formula, which is in good agreement with the data. With this calibration curve the sample could be set to a defined temperature range by flash annealing and choosing a time frame.

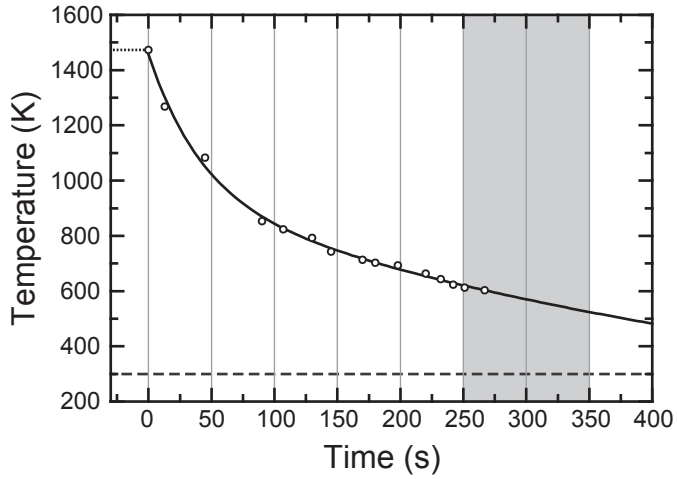

Figure 6.2: Cool down curve of the iridium crystal after flash annealing to 1470 K. The data was fitted by a two component exponential decay formula. The dashed line indicates room temperature. The grey area indicates the time when oxygen was applied to a sample with 53 % coverage of graphene.

Three TPG steps were done to prepare a sample with 53 % coverage of graphene, since intercalation of graphene with oxygen does not work for fully closed layers (see Ref. [21]). The sample was flash annealed to 1470 K and after 250 s of cool down oxygen was applied for 100 s at a pressure of 10^{-5} hPa. During the time of oxygen dosing the sample temperature was in between 620 K and 530 K as one can read out from the extrapolation of the fitted cool down curve.

6.3 Clusters on Graphene/Ir(111)

In this section the preparation of a cluster lattice on graphene on iridium(111) is described. Platinum as well as iridium clusters were prepared.

6.3.1 Platinum Clusters on Graphene

After an XSW experiment of a fully closed layer of pristine graphene on Ir(111) the sample was flash annealed to 1370 K in order to refresh it from possible beam damage. Platinum was evaporated by an electron beam evaporator. The deposited amount was determined utilising a flux monitor, which was calibrated by former STM experiments at TuMA-III lab [67]. During deposition the sample was at room temperature.

6.3.2 Iridium Clusters on Graphene

During a former beamtime at ID32 iridium clusters were deposited onto an iridium crystal that was partly covered with graphene by two TPG cycles leading to a graphene coverage of 39 %. The temperature for flash annealing was 1420 K. After XSW measurements at this pristine graphene sample 0.3 ML iridium was deposited at room temperature by evaporation from a current heated iridium wire. After measuring, the sample was flash annealed to 1100 K in order to move the clusters to the bare iridium terraces. Two more TPG cycles with flash annealing to 1360 K were performed, ending up with a surface coverage of 63 %. After an XSW measurement 0.9 ML iridium was deposited onto the surface.

6.4 High-Vacuum Preparation of Graphene

Cleaning of the iridium crystals at the HV graphene growth chamber can only be done by oxygen firing, as the setup is not equipped with a sputtering gun. Oxygen firing was done at about 1360 K under oxygen pressure around 5×10^{-6} hPa between 5 min to 10 min. Depending on the former treatment the oxygen firing was extended up to almost one hour in sum.

CHAPTER 7

Data Acquisition and Processing

Prior to XPS measurements reflectivity curves were measured to identify regions on the sample with the highest crystal quality. The spots with the lowest value of the FWHM were used for the XPS measurements. All photoelectron spectra were taken with beam energy out of Bragg reflection. Survey scans mostly from 2810 eV down to the Fermi edge were measured. Spectra were taken for different core levels of the elements present on the sample.

The XSW measurements were performed by stepwise measuring XPS for several core levels and subsequently changing the photon energy within ±6 eV around Bragg energy. The photon flux on the sample as well as the reflectivity were recorded for each step. Mostly 31 or 41 single spectra for every core level under investigation were taken.

Note, that due to XSW measuring conditions the overall resolution for all XPS measurements drops down to 400 meV.

The photoelectron spectra are recorded by **SpecsLab**[1]. For analysis the spectra are exported to **CasaXPS**[2]. The identification of the peaks is done by using tabulated values of the binding energies from the **Periodic Library**[3], based on References [68, 69]. For each core level spectrum the one with the highest measuring point density was fitted with single or multiple pure gaussian peaks in order to take the full peak area into account while the peak shape is well described by the fit. The gaussian peaks were fitted just for practical reasons. It would also be suitable to integrate the raw data, but by doing so data containing strongly scattering data points is described better by fits. Also the subtraction of a Shirley background for the whole series works better this way. From spectra with a

[1] SpecsLab, SPECS GmbH
[2] CasaXPS Version 2.3.16 Pre-rel 1.4, Casa Software Ltd
[3] Periodic Library Version 1.0, SPECS GmbH

high measuring point density constraints were defined and applied to the XPS series of an XSW scan. Further, plots of the peak area and also of the reflectivity were produced as a function of beam energy. The fits to this data were produced using the program **DARE**. LEED images were taken by a digital camera in black to white colour code (at LT-STM) or as colour images (at ID32) and are presented with enhanced, inverted contrast in grey scale.

STM images were taken by the software **STMAFM**[4]. Image processing was done using the programs **WSxM**[5] [70] and **SPIP**[6]. Images are presented as raw data with background substraction (global/local plane) only, if not mentioned differently. Further image processing includes correction for tip changes by flattening (line-wise/using paths). Two dimensional fourier transformation maps are produced by the inbuilt 2D-FFT function.

[4]STMAFM3.0, SPS Createc GmbH
[5]WSxM 5.0 Develop 5.3, Nanotec Electronica S.L.
[6]SPIP^{TM} 6.0.9, Image Metrology A/S

PART IV

Results and Discussion

CHAPTER 8

Structural Analysis

Parts of Section 8.1 are also presented in Reference [71].
Parts of Section 8.2 are also presented in References [72] and [73].
Parts of Section 8.3 are also presented in Reference [49] concerning the mechanism of intercalation and in Reference [74] concerning the structure of the intercalation compounds.
LEEM and ARPES measurements were performed by the group of M. Kralj. The STM and LEED experiments were planned and performed by me with assistance of Marin Petrović. The analysis of this data was done by me. XSW experiments were performed together with Carsten Busse, Johann Coraux, and Chi Võ Văn with assistance of the beam line personnel of ID32 at the ESRF, Grenoble, including Jörg Zegenhagen and Blanka Detlefs. The analysis of the XSW data was done by me, the final fits using the program DARE was performed by Jörg Zegenhagen. For experimental details and data processing the reader is referred to Chapters 6 and 7.

This chapter deals with the structure of graphene. In section 8.1 the morphology of graphene is analysed by XSW, showing a dependence of the morphology of the graphene layer on the coverage. The rehybridisation of graphene by cluster adsorption is proven in section 8.2 by determination of the distance of the cluster to the substrate using XSW. In the last section 8.3 the structure of graphene intercalation compounds is shown. Their structure is revealed using LEED, XSW, and STM measurements. For details about the analysis procedure the reader is referred to the experimental chapters.

8.1 Morphology of Graphene/Ir(111)

In this section the dependence of the morphology of graphene/Ir(111) on the coverage is investigated by XSW. For this purpose samples with increasing coverage were prepared and will be discussed in the following. The coverage of these samples are ① 0.22 ML, ② 0.39 ML, ③ 0.63 ML, and ④ 1.00 ML, which were prepared by one TPG step at 1470 K, two TPG steps at 1420 K, four TPG steps at 1420 K, and a TPG plus CVD combination at 1470 K, respectively.

The structural quality of the samples was tested by LEED measurements. The characteristic six fold symmetry of carbon spots and moiré satellites are visible in LEED for all samples, as exemplary shown for sample ④ in Figure 8.1. This diffraction pattern indicates that the carbon rows are aligned to the iridium substrate. The lack of further spots rules out the presence of rotated domains. Consequently, the results presented in this section are valid for well-aligned graphene/Ir(111) without significant disturbance e.g. due to rotated grains.

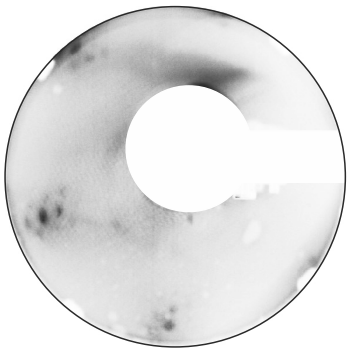

Figure 8.1: LEED image of gr/Ir(111). Carbon and iridium related spots surrounded by moiré satellites are visible. The image was taken from sample ④, but is exemplary for all samples in this section. The sample has been slightly rotated out of perpendicular incidence for better visibility of the spots.

XPS survey spectra reveal the chemical quality of these four samples. A representative spectrum, which was taken on sample ①, is shown in Figure 8.2. Iridium related core level peaks are identified. Beside the named core levels the spectrum in the range of 750 eV to 2000 eV is dominated by Auger electrons. This was found out by changing the energy of the incident photon beam, which results in a shift of the peak positions [75]. Small, broad satellite peaks are also present at an energy of about 30 eV above the named iridium peaks, very prominent e.g. next to the Ir 4p and Ir 3d core levels.

A closer look to a C 1s core level spectrum is presented in Figure 8.3. The C 1s core level peak from the graphene layer resides at (284.35 ± 0.08) eV.The raw data (circles) is well-described by the XPS fit (grey line) and allows for a determination of the peak area (light grey area), i.e. the total photoelectron yield. In the same way the series of spectra for all samples were analysed leading to the XSW results shown in grey in Figure 8.4.

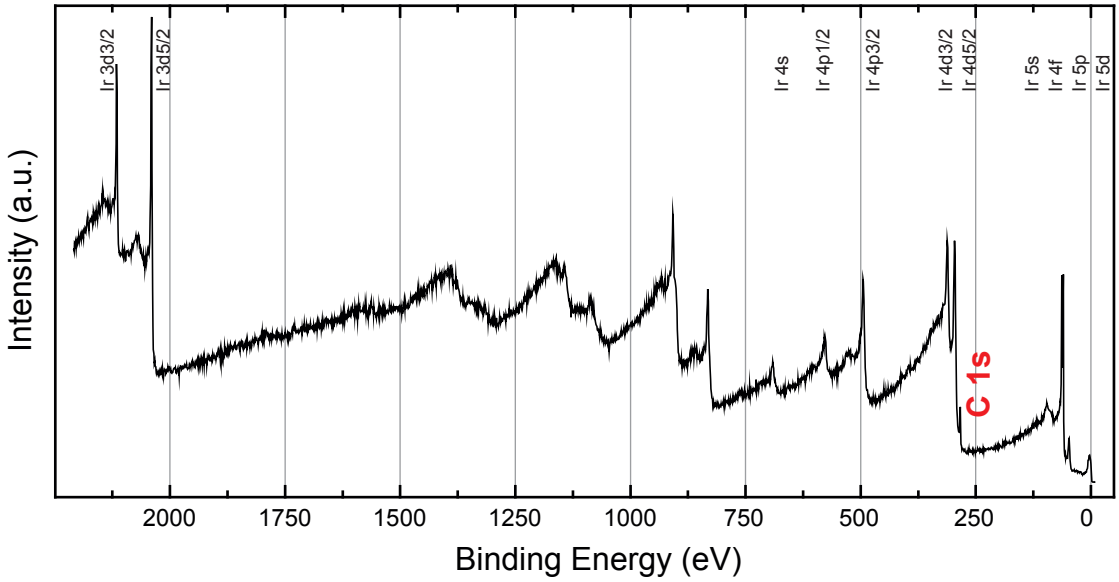

Figure 8.2: XPS survey spectrum of gr/Ir(111). Iridium related core level peaks are shown in the top row in the diagram. In the range of 750 eV to 2000 eV the spectrum is dominated by Auger peaks (comp. Ref. [75]). The graphene flakes lead to additional carbon peaks, i.e. the C 1s core level at 284.1 eV. See text for discussion of additional peaks (e.g. Auger peaks). Photon energy was 2810 eV.

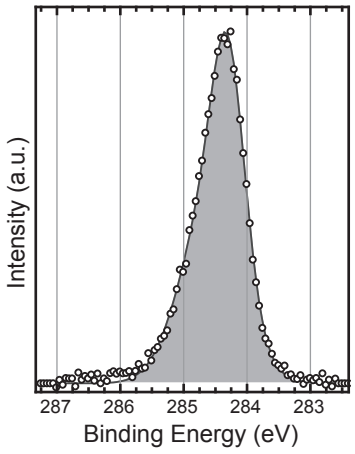

Figure 8.3: XPS measurement of the C 1s core level of gr/Ir(111). Background substracted raw data is shown as circles, the fit to the C 1s core level is shown as a grey line, leading to the total photoelectron yield (light grey area). The integral of the peak (area) is used for the XSW analysis. Photon energy was 2810 eV.

The raw data is shown as grey points, the XSW fits of these data as grey solid lines, and the corresponding reflectivity is depicted in orange points (raw data) and orange solid lines (fits). Samples ② and ③ were measured during a former beam time at ID32 with a different detector with poorer performance. Hence, the error bars are larger for sample ② and ③.

XSW measurements were repeated on different positions on the samples. The resulting parameters coherent position $P^{(\mathrm{hkl})}$ and coherent fraction $F^{(\mathrm{hkl})}$ were averaged over all sample measurements and are presented in table 8.1, coming from one, two, four, and three measurements for samples ①, ②, ③, and ④, respectively. A refined data analysis for samples ② and ③ yields values that differ slightly but insignificantly from those published in Reference [11].

Table 8.1: XSW results for pristine gr/Ir(111). Average values of the coherent position and coherent fraction of graphene flakes and a fully closed graphene layer. Results are averaged from one, two, four, and three single XSW measurements for samples ①, ② ③, and ④, respectively.

Sample	**Coverage**	$P^{(111)}$	$F^{(111)}$
①	0.22 ML	0.52 ± 0.01	0.70 ± 0.04
②	0.39 ML	0.52 ± 0.01	0.85 ± 0.05
③	0.63 ML	0.52 ± 0.01	0.72 ± 0.04
④	1.00 ML	0.50 ± 0.03	0.38 ± 0.17

The results of the coherent fraction depend on the homogeneity of the sample. Therefore an estimation of the portion of generally present non-regularly distributed carbon atoms is necessary. This atoms lower the value from exactly $F_{\mathrm{flat}} = 1.00$ for a perfect flat layer. Point defects within the graphene layer can be neglected as they are rarely seen in graphene on iridium and have a very small portion due to their 0D nature. From LEED images (comp. Fig. 8.1) the presence of grain boundaries can be excluded, and small angle rotations should not have a big influence. Therefore the residual defects that should be taken under considerations are the corrugation of graphene, carbon contamination, wrinkles, step edges of the substrate, as well as graphene edges.

Carbon contamination from adsorbates can be excluded as they were never observed by STM on freshly prepared pristine graphene. Furthermore, there is no signature for a different carbon species in the photoelectron spectra. Moreover, in case that a carbon contamination would exist on the pristine iridium it would mean that for lower coverage this effect would increase, leading to a lowering of the coherent fraction. However, this is

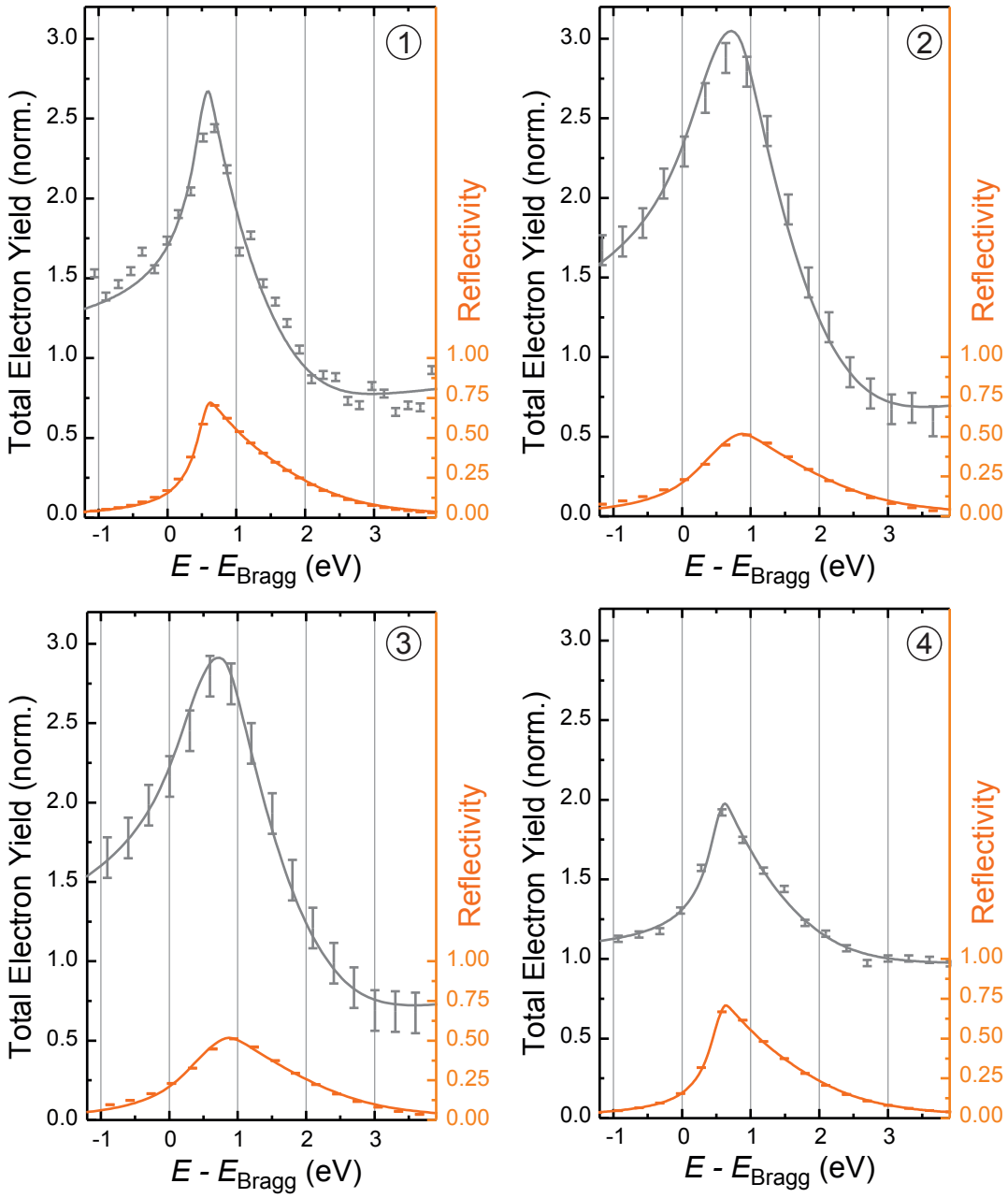

Figure 8.4: XSW measurements of the C 1s core level of gr/Ir(111). The total photoelectron yield of samples ① to ④ is shown in grey, the corresponding reflectivity in orange.

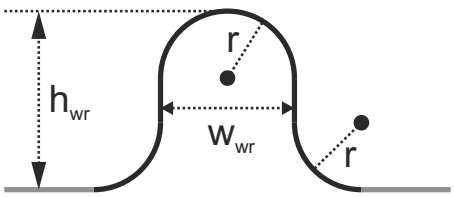

Figure 8.5: Model of a gr wrinkle. The wrinkle is split into bended and straight sections. The bended sections combines to a tube with the diameter w_{wr}. The straight section consists of two lines with the length of $h_{\mathrm{wr}} - w_{\mathrm{wr}}$. The arc length of the wrinkle b_{wr} is shown in black, the flat graphene layer in grey.

in contradiction to our findings. This means that there are no contamination present on our samples that would have influence on our results.

Wrinkles are formed during the cool down of the sample due to a difference in the thermal expansion coefficient of graphene and iridium ($\Delta\alpha = 7.15 \times 10^{-6}$) [76]. From STM measurements the width of wrinkles w_{wr} was determined to be in the range of 2.8 nm to 10 nm. However, it is unlikely that the width of wrinkles varies much. The reason for that is the increasing cost of delamination energy. It is more likely that the tip artificially broadens the wrinkle, as it is common for high objects in STM (tip convolution). Conclusively a width of 3 nm was used for the following estimation. The height h_{wr} of wrinkles was found to be in the range of 2.8 nm to 3.8 nm, therefore a value of $h_{\mathrm{wr}} = 4$ nm is a good upper limit for the determination of lifted carbon within the sample. The arc length b_{wr} of graphene across the wrinkle can be determined by a model shown in Figure 8.5. The wrinkle can be split into bended and straight sections. Overall the bended sections combine to a tube with the diameter of 3 nm, and a residual straight part of 1 nm

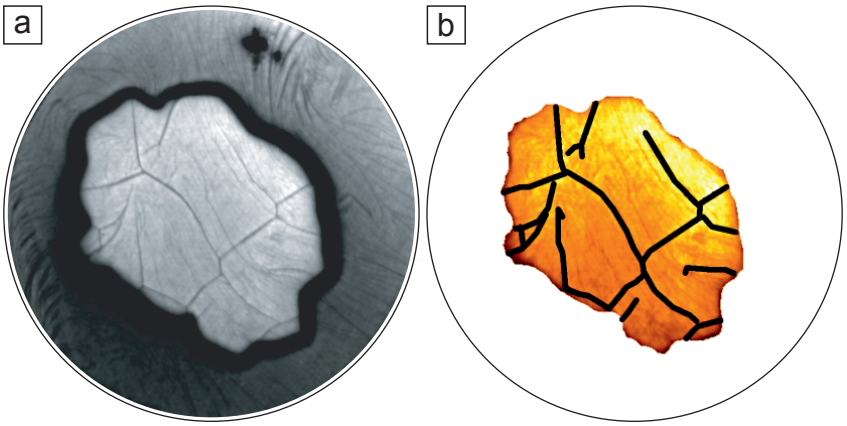

Figure 8.6: LEEM image of gr/Ir(111). Graphene flake (bright center) on iridium (a). Detail view (b) of the flake with wrinkle network superimposed as black lines. Faint lines are step edges. Field of view is 10 μm. Image reprinted with permission from Ref. [76].

from the difference between height and width of the wrinkle. Hence, the arc length of the wrinkle results to $b_{\mathrm{wr}} = \pi \cdot 3\,\mathrm{nm} + 2 \cdot 1\,\mathrm{nm} = 11.4\,\mathrm{nm}$.
The density of wrinkles can be estimated from LEEM images, shown in Figure 8.6. The total area of the flake (bright centre) is approximately $A_{\mathrm{fl}} = 25.1\,\mu\mathrm{m}^2$, while the area that is covered with wrinkles is $A_{\mathrm{wr}} = w_{\mathrm{wr}} \cdot l_{\mathrm{wr}} = 0.081\,\mu\mathrm{m}^2$, where $l_{\mathrm{wr}} = 27\,\mu\mathrm{m}$ is the measured length of the entire wrinkle network, which is in line with findings in References [49, 76]. The ratio of carbon inside a wrinkle to the whole carbon present in the sample can be determined using the ratio of the surface area of the wrinkles $S_{\mathrm{wr}} = b_{\mathrm{wr}} \cdot l_{\mathrm{wr}}$ to the whole surface area $A = A_{\mathrm{fl}} - A_{\mathrm{wr}} + S_{\mathrm{wr}}$. The ratio p_{wr} of lifted carbon to the entirety arised by the reason of wrinkles is therefore

$$p_{\mathrm{wr}} = \frac{S_{\mathrm{wr}}}{A_{\mathrm{fl}} - A_{\mathrm{wr}} + S_{\mathrm{wr}}} = \frac{b_{\mathrm{wr}} \cdot l_{\mathrm{wr}}}{A_{\mathrm{fl}} - w_{\mathrm{wr}} \cdot l_{\mathrm{wr}} + b_{\mathrm{wr}} \cdot l_{\mathrm{wr}}} = 1.21\,\%. \tag{8.1}$$

Step edges are also regions where the distance between graphene and iridium naturally varies as the graphene layer continuously covers the steps of the substrate. To get a rough estimation about how large the effect of the step edges is the average step edge distance is analysed. In Figure 8.7 two large scale images of a clean iridium(111) surface are shown. As many large scale images show a significant lower amount of step edges, the results presented here are therefore an upper limit.
A cross section perpendicular to the steps was taken, which is shown to the right of each image. For Figure 8.7(a) it contains 19 steps over a length of 196 nm, which results to an average distance of the steps of 10.3 nm. In Figure 8.7(b) the cross section has a length of 775 nm containing 60 steps. The average step distance thus amounts to 12.9 nm. From these two values the average step edge distance results to $d_{\mathrm{steps}} = 11.6\,\mathrm{nm}$. Assuming the step edge to be shaped like two connected arcs of a cylinder (comp. Ref. [39]) the width of the step edge can be estimated using the iridium step height $d_{\mathrm{Ir}} = 0.222\,\mathrm{nm}$ and the bending radius $R = 0.27\,\mathrm{nm}$ [39]. Geometrically the width of the graphene layer across a step edge results to $l = 0.508\,\mathrm{nm}$, while the projected width is $l_{\parallel} = 0.436\,\mathrm{nm}$. The ratio p_{SE} of lifted carbon atoms due to step edges is therefore

$$p_{\mathrm{SE}} = \frac{l_{\parallel}}{d_{\mathrm{steps}} + (l - l_{\parallel})} \cdot \frac{l}{l_{\parallel}} = \frac{l}{d_{\mathrm{steps}} + (l - l_{\parallel})} = 4.35\,\%. \tag{8.2}$$

Graphene edges have a contribution that depends strongly on the morphology of graphene. While the amount of edge atoms is negligible for large islands, small islands have a high fraction of them. The atoms at the edge of a graphene flake are predicted to be bound more strongly to the substrate with a height of approximately 1.6 Å [77].

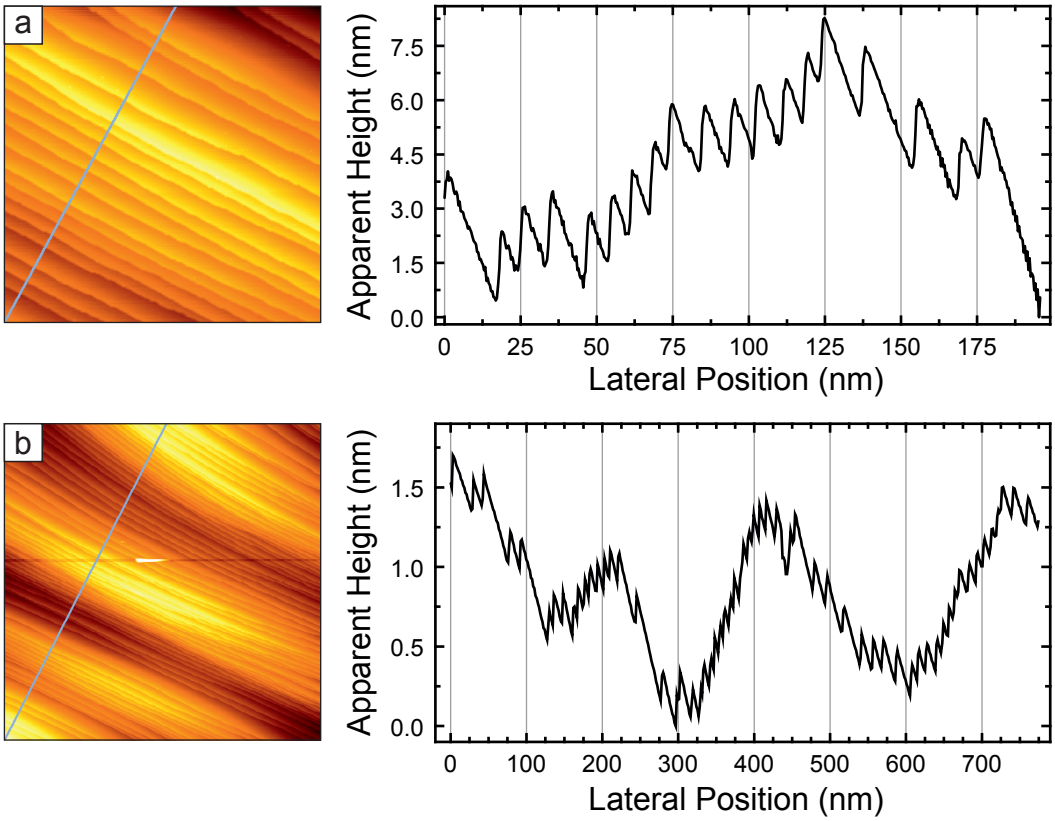

Figure 8.7: STM images of step edges on a clean Ir(111) surface. (a) Image size is 172 nm × 172 nm, the line marks the position of the cross section, shown on the right. The cross section has a length of 196 nm, containing 19 steps. Image (b) has a size of 690 nm × 690 nm, the cross section on the right was measured at the position of the line, which contains 60 step over 775 nm. Images were taken at room temperature.

Moreover, the centre of a nano flake with a width of five carbon rings does not reach the experimentally measured average height of 3.38 Å from Reference [11], but is predicted to be situated at 3.05 Å [78] or 3.13 Å [77]. A significant difference to the mean height is found for the outermost two atom rows of the zig-zag edge (comp. Ref. [77]). Hence, the width of incoherent edge atoms can be approximated by $\Delta_{\text{edge}} = 1.1$ Å. The fraction of edge atoms can be estimated by the ratio of the area of a circular ring $A_{\text{edge}} = \pi \cdot (R^2 - (R - \Delta_{\text{edge}})^2)$ to the area of the entire circle $A_{\text{flake}} = \pi \cdot R^2$. For the case of sample ① with a coverage of 0.22 ML and a preparation temperature of 1470 K the radius can be approximated by 20.2 nm (comp. Ref. [37]). Hence, the fraction of the edge atoms results to

$$p_{\text{egde}} = \frac{A_{\text{edge}}}{A_{\text{flake}}} = \frac{\pi(2R\Delta_{\text{edge}} - \Delta_{\text{edge}}^2)}{\pi R^2} = 2 \cdot \frac{\Delta_{\text{edge}}}{R} - \left(\frac{\Delta_{\text{edge}}}{R}\right)^2 \overset{①}{=} 1.09\,\%. \tag{8.3}$$

In conclusion this means that up to $p_{\mathrm{SE}} + p_{\mathrm{wr}} \approx 6\,\%$ of the carbon atoms obey a incoherent height above the substrate just by wrinkles and step edges and which reduce the values of the coherent fraction. Hence, for real samples the coherent fraction might in general be reduced by a factor of up to $p = 6\,\%$. In a more differentiated view, for small islands the influence of graphene edges gains importance, while the influence of wrinkles can be neglected in that case.

A theoretical value from a DFT calculation including the van-der-Waals force predicts the height and the height distribution of gr/Ir(111) [11]. It was calculated from a supercell containing 10×10 graphene unit cells on top of four layers of 9×9 iridium atoms with periodic boundary conditions. Thus, the DFT calculation is a model for fully closed layers. The resulting positions can be calculated to coherent position and coherent fraction values as described in Reference [52], leading to $P_{\mathrm{DFT}}^{(111)} = 0.54$ and $F_{\mathrm{DFT}}^{(111)} = 0.97$.

For a better comparison of the data and the DFT calculations an illustration of the XSW results is presented in Figure 8.8. The evolution of the coherent position $P^{(111)}$ is shown in black, while the coherent fraction $F^{(111)}$ is shown in pink. The respective values from DFT are shown as dashed lines. One can clearly see, that the value for the coherent

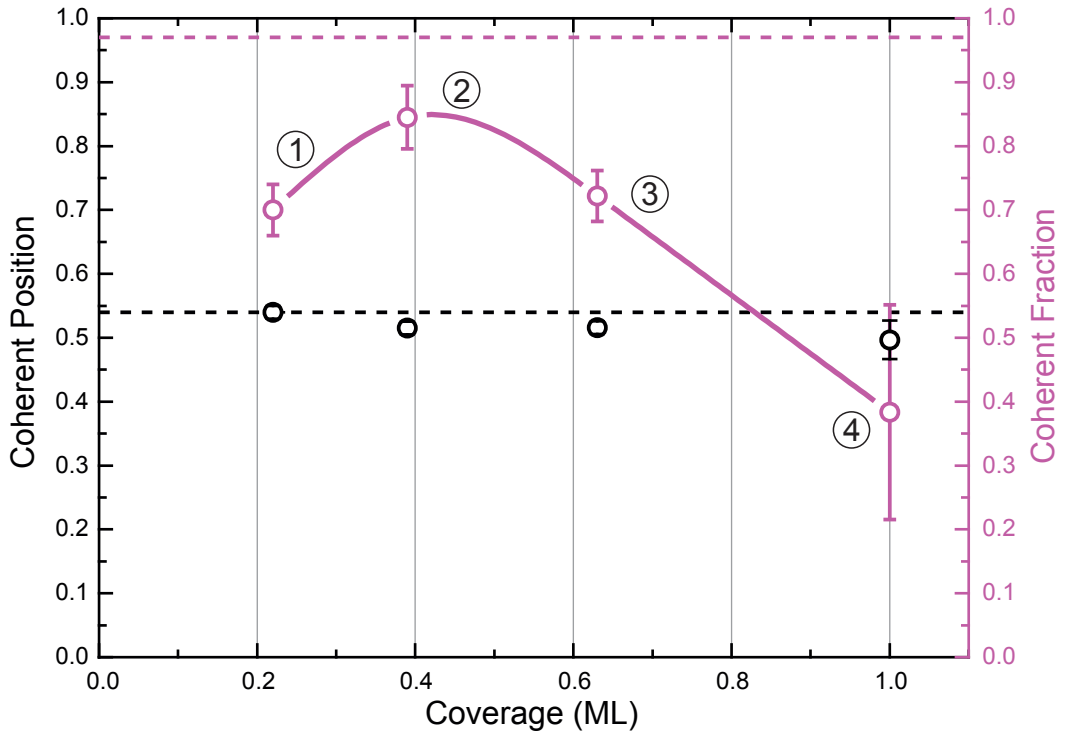

Figure 8.8: XSW results of gr/Ir(111). The coherent position (black) and coherent fraction (pink) versus graphene coverage. The pink line is inserted to guide the eye. The theoretical values [11] for the coherent position and coherent fraction are shown as dashed lines.

position $P^{(111)}$ versus the coverage is quite robust. Moreover, the results of the coherent position from the DFT calculation are in good agreement with our data.

While the value for the coherent position stays almost constant for different coverages the coherent fraction changes a lot. The highest value is found for sample ② and decreases for both lower and higher graphene coverages. A pink line is inserted to ease the view on this tendency.The morphologies of the analysed samples can be described by taking a look into exemplary STM images [11, 37] as shown in Figure 8.9. These samples were prepared under near identical conditions in our home labs. The sample morphologies ①, ②, ③, and ④ can be described as small islands [Fig. 8.9(a)], large islands [Fig. 8.9(b)], a network of percolated graphene flakes with vacancy islands in it [Fig. 8.9(c)], and a fully closed layer [Fig. 8.9(d)], respectively.

To understand this behaviour of the coherent fraction it is adjuvant to think about the growth process and further treatment of graphene on iridium: The samples were all prepared above 1420 K, i.e. at elevated temperatures. However, the measurements were performed at room temperature. Due to different thermal expansion coefficients of graphene and iridium, this procedure leads to compressive stress within the graphene layer [39]. A way of stress relaxation is the formation of wrinkles [39] (see discussion about influence of wrinkles to XSW results below). Nevertheless, for the formation of wrinkles it is mandatory that parts of the graphene layer can slip across the sample, feeding wrinkles with more and more carbon atoms. This slipping process is a possible way of stress relaxation for all kinds of samples. In case of medium-sized islands [sample ②] the sliding allows for sufficient relaxation. To the contrary for spatially extended networks [compare

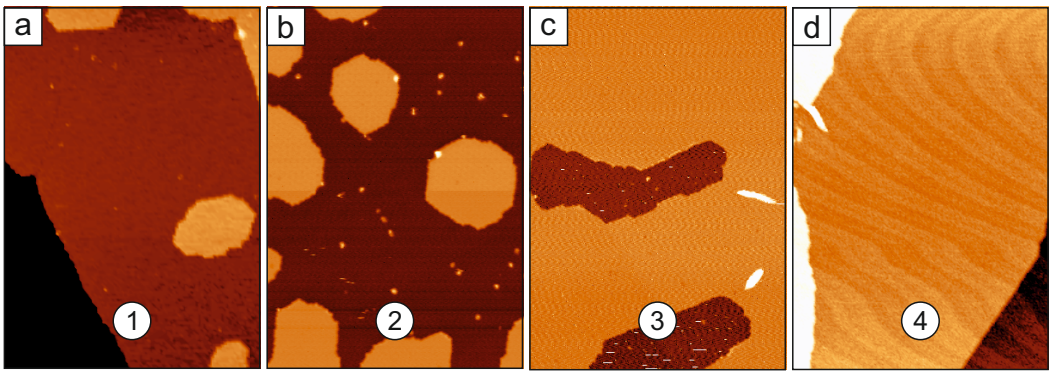

Figure 8.9: STM topographs of gr/Ir(111). The imaged samples (a,b,c,d) were prepared by one TPG step (0.22 ML) at 1470 K, two TPG steps (0.39 ML) at 1420 K, four TPG steps (0.63 ML at 1420 K, and one TPG step followed by CVD at 1320 K. Hence, they correspond to samples ①, ②, ③, and ④, respectively. All images are presented in identical colour scale and image width, which is 100 nm. Data reevaluated, comp. Refs. [37, 38] (a), Ref. [75] (b,c), Ref. [27] (d).

Table 8.2: Peak-to-peak corrugation of graphene. Values consider generally present incoherent C atoms caused by wrinkles, iridium step edges, and graphene edges. The lower limit corrugation are corrected for this incoherent C atoms.

		Corrugation	
Sample	**Coverage**	average	lower limit
①	0.22 ML	0.85 Å	$\geq$ 0.73 Å
②	0.39 ML	0.57 Å	$\geq$ 0.36 Å
③	0.63 ML	0.94 Å	$\geq$ 0.86 Å
④	1.00 ML	1.82 Å	$\geq$ 1.33 Å

sample ③] slipping is inhibited as isotropic relaxation must lead to wrinkle formation with the associated cost of delamination energy. For the fully closed layer [sample ④, Fig. 8.9(d)] this effect is even stronger.

While the relaxation of strain was found to vary on length scales below 340 nm on SiC [79], it can be assumed that wrinkles do not lead to a complete stress relaxation for the entire sample. Therefore the stress state of the samples might vary laterally on small length scales, meaning that for XSW measurements these stress variations are averaged. Hence, the experimental value for the coherent fraction is lowered.

This explanation is suitable to describe the tendency of the coherent fraction value for the high coverage regime, but does not hold for the case of small islands [compare sample ①, Fig. 8.9(a)]. For this case the area of graphene islands can be determined utilising the graphene island density diagram from Reference [28]. The average value for the radius results to $R = 20.2\,\text{nm}$. With the estimation of the width of the edge of 1.1 Å the fraction of edge atoms results in $p_{\text{edge}} = 1.09\,\%$. Note, that in contrast to the estimation of wrinkles this value marks the *lower* limit, as the estimation is based on circular islands. In case that the island is elongated, the circumference increases. As a matter of fact most of the islands are elongated, meaning that the fraction of edge atoms is even larger. For sample ① it can be concluded that the fraction of incoherent atoms from the edge and step edges is $p = p_{\text{edge}} + p_{\text{SE}} \approx 6\,\%$.

The XSW results clearly reveal that the corrugation of graphene depends on the graphene coverage and is lowest for medium-sized islands. Moreover it is also closest to the theoretical approximation of $F_{\text{DFT}}^{(111)} = 0.97$. However, the experimental value does not perfectly agree with this DFT results, as theory does not include additional stress due to the cool down of the sample.

As described in the supplementary information in Reference [11] the coherent fraction can be translated into the peak-to-peak amplitude of the moiré corrugation using an eggbox model. A diagram of the coherent fraction versus the peak-to-peak height of the moiré

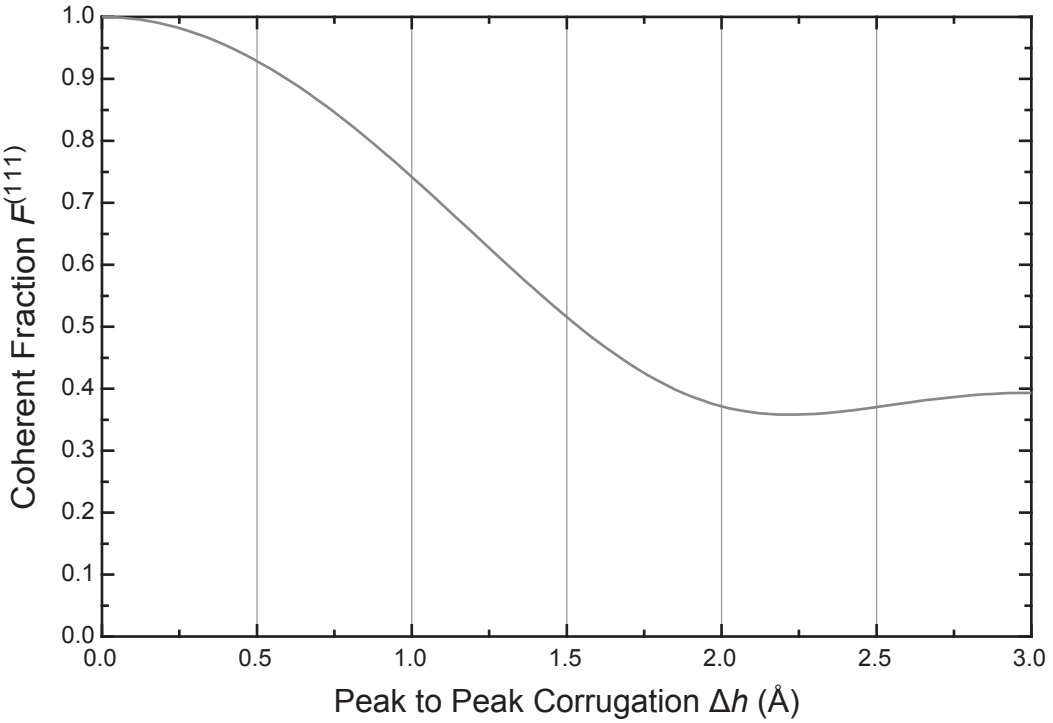

Figure 8.10: Simulation of the corrugation amplitude for gr/Ir(111). The coherent fraction $F^{(111)}$ as a function of the difference of the highest to the lowest atom within a moiré unit cell Δh, resulting from theory described in Ref. [11].

is shown in Figure 8.10. The resulting peak-to-peak heights for samples ① to ④ are presented in Table 8.2. As mentioned before, for sample ① the incoherent carbon comes from iridium step edges and graphene edges, therefore the measured coherent fraction can be corrected to $F^{\text{corr}}_{①} = 0.70/0.94 = 0.81$. Surprisingly, this value is still lower than for sample ②. A reason for this can again be found in the morphology. The slipping process for the reduction of compressive stress within the graphene is impeded for smaller islands, as the more strongly bound edge atoms of the islands act like an energy barrier, that has to be overcome by the strain energy. The over-all strain energy is just to low for small islands, and suffices to enable the slipping process for larger ones.

8.2 Rehybridisation of Graphene

As discussed in Section 1.3 metal deposition onto graphene on iridium(111) leads to a formation of a highly ordered cluster array. The structure of clusters prepared by deposition of 0.1 ML iridium can be seen in Figure 8.11(a) [28, 42]. The clusters are formed on the graphene island with mostly one level of height, while dendritical islands grow on the bare iridium. A cross section (inset) reveals that the majority of the clusters has a monoatomic thickness. In order to determine the height of the clusters above the substrate XSW measurements were performed at a fully closed graphene layer, that was covered with 0.1 ML of platinum (Sample ①). For this coverage it was shown that most of the clusters consist of one platinum layer only [28]. As shown in Figure 8.11(b) no evidence for rotational domains or superstructures is found for the sample. Therefore it can be concluded that the sample has a high structural quality.

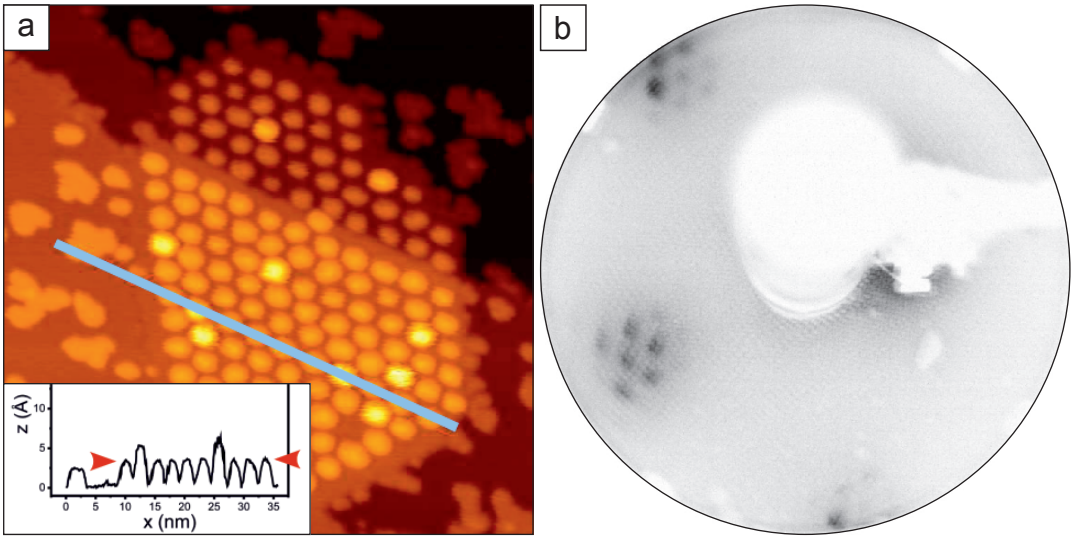

Figure 8.11: STM and LEED image of clusters on gr/Ir(111). Exemplary STM image (a) of regularly arranged Ir clusters on graphene islands (from literature). Deposited amount was 0.10 ML. Inset: cross section of the Ir clusters along the blue line in the STM image. LEED image (b) of a fully closed gr layer on which 0.1 ML of platinum was deposited. C and Ir related spots as well as moiré satellites are clearly visible. The sample reveals no evidence for rotational domains or superstructures. The sample was slightly rotated to make the carbon spots and satellites hit the screen. Image (a) reprinted with permission from Ref. [28].

An XPS survey scan reveals the chemical composition of the sample, as shown in Figure 8.12. Beside the characteristic peaks from iridium and carbon (compare Fig. 8.3) additionally platinum core level peaks can be found. As platinum and iridium are neighbours

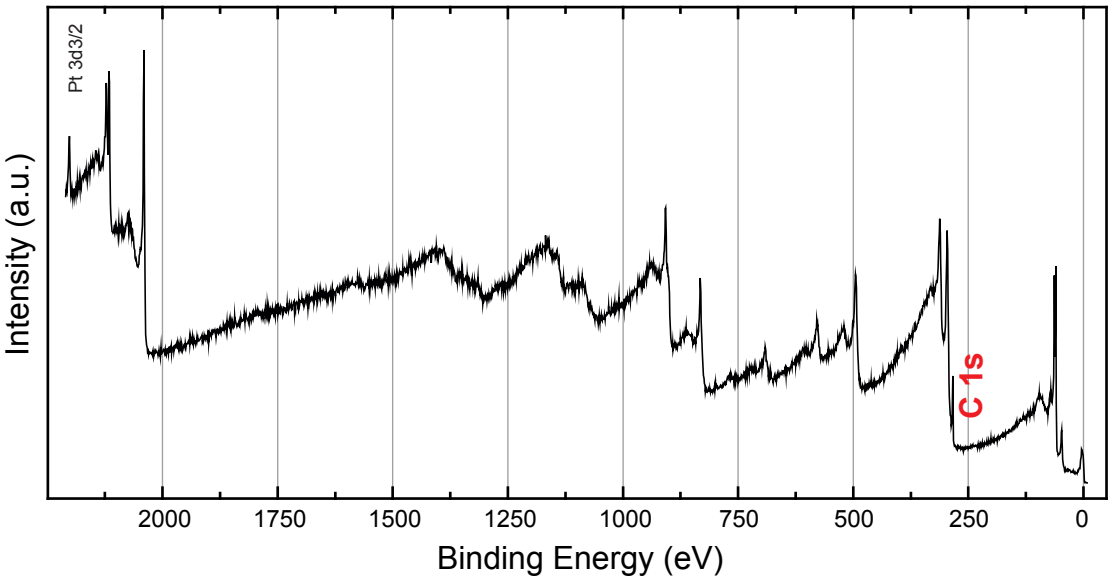

Figure 8.12: XPS survey scan of Pt/gr/Ir(111). Beside the Ir core level peaks (comp. Fig. 8.2) also the C 1s and Pt related core level can be seen. The Pt $3d_{3/2}$ core level is well seperated from the Ir peaks and therefore an ideal candidate for further XSW analysis. Photon energy was 2810 eV.

in the periodic table of elements the energetic positions of equal core level below 2000 eV are energetically very close to each other. Hence, the measured peaks can hardly be deconvolved as the energy resolution is poor at XSW measurements due to the need of high photon energy for Bragg condition.

Nevertheless, the Pt $3d_{3/2}$ core level at 2202 eV is energetically clearly separated from the iridium peaks. Thus it is used for the XSW analysis as well as the C 1s signal. These core levels were measured with higher resolution as shown in Figure 8.13 (circles). The fits of the core level peaks are shown as solid lines, indicating a good agreement with the

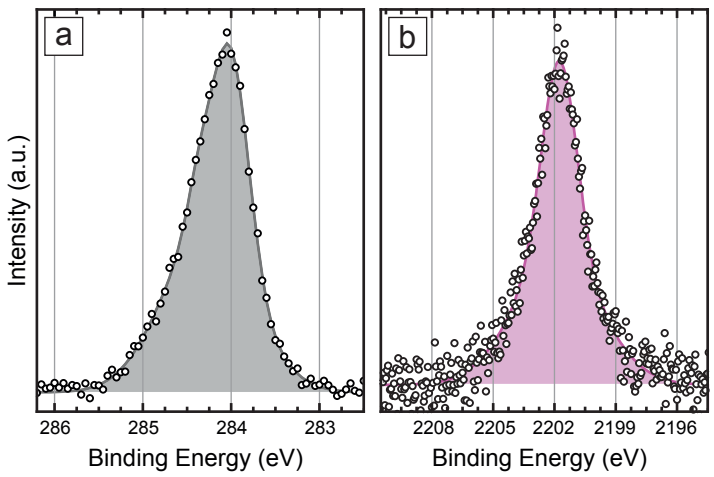

Figure 8.13: XPS core level spectra from Pt/gr/Ir(111). Raw data are shown as circles, fits to the core levels as solid lines and the total photoelectron yield as filled area. Core level spectra from C 1s (a) and Pt $3d_{3/2}$ were recorded at photon energies of 2810 eV.

original data. As the deposited amount of platinum is rather low compared to the carbon present on the sample the background noise is significantly higher for the Pt $3d_{3/2}$ core level spectrum than it is for the C 1s spectrum. For the entire series of measurements the area of the XPS fits is extracted to obtain the total photoelectron yield, leading to the XSW results presented in Figure 8.14.

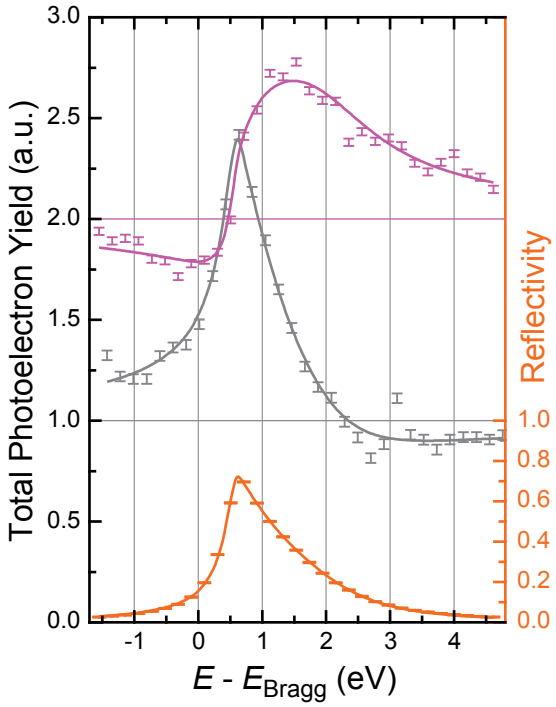

Figure 8.14:
XSW results of Pt/gr/Ir(111). Raw data are shown as circles, fits as solid lines. XSW results for the C 1s core level are shown in grey, for the Pt $3d_{3/2}$ in pink. Pt values are shifted by 1 for better presentability. For each core level the corresponding value of 1 is inserted as a horizontal line. The reflectivity is coloured in orange.

Two measurements for the (111)-reflections and one measurement for the (222)-reflection were done. The extracted values for the coherent position $P^{(\mathrm{hkl})}$ and coherent fraction $F^{(\mathrm{hkl})}$ are presented in table 8.3. In addition to the sample containing platinum clusters the results from a former beam time are added, where iridium cluster were deposited on

Table 8.3: XSW results for clusters on gr/Ir(111). For the (111)-reflection of sample ① results of two measurements are averaged, for the (222)-reflection only one measurement was performed. Samples ② and ③ were measured at a former beam time after Ir deposition onto samples ② and ③ from Section 8.1.

			C 1s		Pt $3d_{3/2}$	
Sample	**Cluster**	**Refl.**	$P^{(hkl)}$	$F^{(hkl)}$	$P^{(hkl)}$	$F^{(hkl)}$
①	0.1 ML Pt	(111)	0.52 ± 0.01	0.46 ± 0.04	0.10 ± 0.02	0.49 ± 0.05
①	0.1 ML Pt	(222)	0.09	0.36	0.18	0.38
②	0.3 ML Ir	(111)	0.51 ± 0.01	0.38 ± 0.04		
③	0.9 ML Ir	(111)	0.52 ± 0.01	0.33 ± 0.05		

graphene islands: The samples ② and ③ introduced in Section 8.1 were post-processed by iridium deposition of 0.3 ML iridium and 0.9 ML iridium, respectively.
From the coherent position the height of the platinum clusters can be determined and results to (4.65 ± 0.04) Å. This finding can be compared with a simple sphere model based on the known empirical covalent radii [80] for the involved atoms, and considering the tetrahedral angle for the carbon bonds as shown in Figure 8.15. This model leads to a height of the cluster of 4.70 Å, which is in very good agreement with our findings. Details about platinum clusters on graphene can also be found in Reference [73].

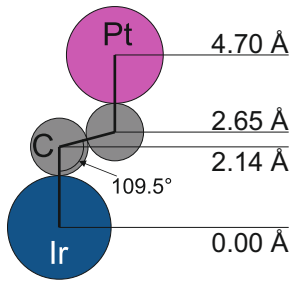

Figure 8.15: Sphere model of Pt cluster on gr/Ir(111). The height of the Pt atom above the Ir substrate atoms is modelled using empirical covalent radii of the involved atoms. Tetrahedral angles of 109.5° are assumed enclosing the bonds at the C atoms leading to a distance between Pt and the substrate of 4.70 Å.

In case of iridium clusters on graphene the height determination is difficult. Although from a theoretical point of view the core level of iridium cluster atoms differ from those of the bulk atoms due to the surface core level shift, an experimental height determination of the clusters is not possible: Firstly, the surface atoms of the iridium substrate reveal also a surface core level shift, which complicates the analysis by this uppermost layer of iridium atoms. Secondly, the low energy resolution inhibits a precise distinction of these different components.
The rehybridisation affects the carbon atoms in a rather complicated way [45]. Therefore, based on the heights of the carbon atoms from the sketch in Figure 8.15, a very simple model as depicted in Figure 8.16 was used to approximate the situation. For this model three different height levels are taken into account: the low sp^3-hybridised atoms (2.14 Å), the high sp^3-hybridised atoms (2.65 Å), and the experimental determined average height of the sp^2-hybridised carbon atoms(3.38 Å), all shown in red. The grey line represents the case that iridium atoms on top of the graphene layer rehybridise two carbon atoms, leading to a change in height for one to the low level and one to the high level. Starting from the open red circle (no rehybridised atoms) the increasing number of iridium cluster atoms in contact with the graphene layer leads to the grey line, where every 10 cluster atoms are labelled by the number and an open blue circle up to the case where all carbon atoms in the moiré unit cell are hybridised. From STM measurements it is known that for high coverages multilayer growth sets in, so that for 0.1 ML the lowest layer consists

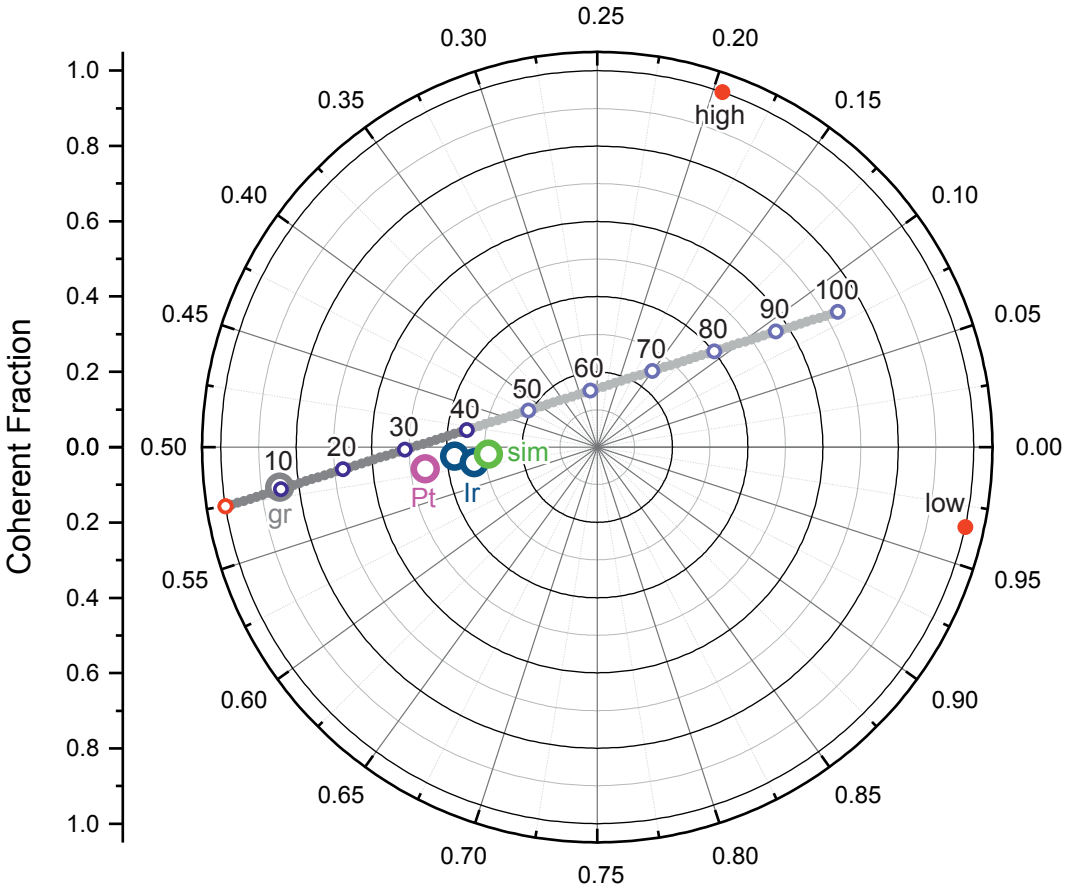

Figure 8.16: Simulation of structure parameters for gr with adsorbed clusters. In this Argand-diagram the coherent fraction $F^{(111)}$ is presented as the radial, and the coherent position $P^{(111)}$ as the angular parameter. Simulation contains three height levels (red circles): 3.38 Å for pristine gr, 2.14 Å for the lower rehybridised, and 2.65 Å for the upper rehybridised carbon atoms. Series of structure parameters for increasing amount of adatoms (grey), blue circles indicate every 10 cluster atoms, indicated by the numbers. Result for pristine gr (grey) and clusters [Pt: pink, Ir: blue (outer: 0.3 ML, inner: 0.9 ML), simulation [72]: green].

of 8 atoms, while for 1.0 ML only 40 atoms are in contact with the graphene layer [81]. The occurrence of a maximum amount of cluster atoms that are in direct contact to graphene can easily be understood, as every rehybridised carbon atom has to be on top of an iridium atom, which is definitely not the case for all carbon atoms within the moiré unit cell (comp. Fig. 1.3). For this reason the simulated values for more than 40 cluster atoms touching graphene are shown faded, as they are physically irrelevant.

As from Section 8.1 it is already known that the coherent fraction is strongly dependent on the morphology of the sample the correct starting point of the simulation is unclear. Moreover, the influence of cluster atoms is not limited to the carbon atoms directly below the cluster but also the neighbouring ones. In addition the rehybridisation generates com-

mensurability, influencing the moiré amplitude. This means, that it might be necessary to compress the simulated results towards the totally rehybridised graphene layer. However, for the simulation supposing a starting point is refrained and the simplest assumption is used instead, i.e. the measured average height with a coherent fraction of 1.
The simulation reveals, that the coherent position has an almost constant value in the region of interest, meaning that it depends only weakly on the amount of cluster atoms that are in contact with graphene. On the contrary, the coherent fraction has a strong dependence on it. In the diagram, the data points from the measurements are also shown, which are very close to the simulated values. On top of that, also the tendency of increasing amount of cluster atoms fits to the simulation: the higher the value for Θ, the more the data points are positioned to the right in the diagram.
In Reference [72] we went beyond the simple model: A combination of the Keating potential and SXRD experiments leads to the green data point, labelled 'sim'. As the deviation of this data point to the simple model is very small, it can be concluded that the simple model described above is a good approximation for the clusters deposited onto graphene. Conclusively, the XSW study complements earlier spectroscopic and theoretical studies [45] by explicit structural evidence of rehybridisation.

8.3 Graphene Intercalation Compounds

As a perfect graphene layer is impermeable even to helium atoms [82], first the intercalation process itself is discussed. We found that intercalation takes place at defects within the graphene layer [49].

LEEM (low energy electron microscopy) measurements were performed during the deposition of caesium onto a fully closed graphene layer on iridium. For the pristine graphene sample this is shown in Figure 8.17(a), where dark lines represent wrinkles and the faint lines correspond to steps of the substrate. After deposition of 0.06 ML_{gr} caesium the same region is imaged in Figure 8.17(b). The image shows two different contrasts that are labelled α and γ. In this deposition experiment the contrast changed continuously from that one seen in Figure 8.17(a) to that seen in Figure 8.17(b) on the α phase. Further deposition of caesium leads to the appearance and growth of the γ phase until the α phase has vanished.

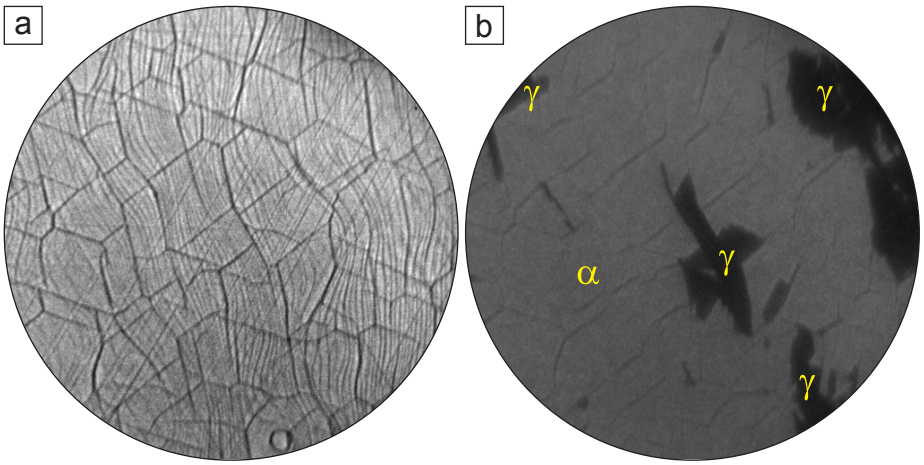

Figure 8.17: LEEM topographs of Cs-grIC during preparation. Images taken before (a) and after (b) the deposition of 0.06 ML Cs on the same spot on the sample. Two different regions are found in (b), where 0.06 ML_{gr} was deposited onto the graphene sample. Image reprinted with permission from Ref. [49].

An interesting fact of this measurement is that the appearance of the γ-phase always begins at wrinkles, mostly at wrinkle crossings. Moreover, the spread of the γ-phase is not continuous but stepwise. Whenever the γ-phase reaches step bunches of the substrate it stops until this region is homogeneously filled. Hence, step bunches of the substrate act like a barrier to the spread of the γ-phase.

A series of samples with different amount of caesium was also investigated by ARPES as shown in Figure 8.18. For pristine graphene [Fig. 8.18(a)] a sharp Dirac cone can

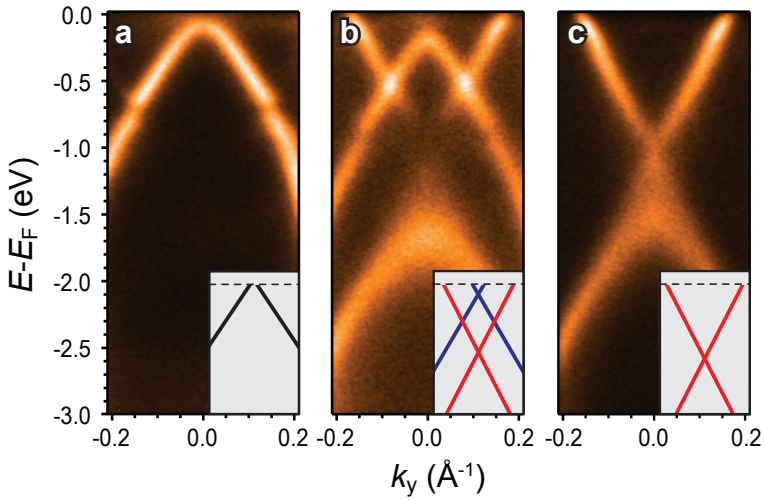

Figure 8.18: ARPES maps of graphene samples after Cs deposition. Measurements done across the K point of gr. Sample before (a), and after deposition of 0.5 ML (b), and 1 ML (c) of Cs. Insets show schematically the Dirac cones, corresponding to pristine (blue), light (green) and heavily (red) doped gr. Image reprinted with permission from Ref. [49].

be seen exhibiting slight p-doping, which is consistent with previous experiments [35, 40]. Deposition of up to 0.06 ML caesium causes an increasing n-doping of the graphene, indicated by a shift of the Dirac point down to 0.2 eV below the Fermi level. Further deposition of caesium leads to the appearance of a second cone, as shown in Figure 8.18(b) for 0.5 ML caesium. For more than 0.9 ML caesium the first, slightly doped cone disappears as shown in Figure 8.18(c) [$\theta = 1.0$ ML] ending up with only the heavily doped cone. From these deposition series the α-phase can be related to the slightly doped cone, while the heavily doped cone corresponds to the γ-phase. These results reveal, that the electron transfer to graphene is strong for the dense γ-phase and weak for the α-phase.

To determine the nature of the α- and γ-phases STM measurements were performed for a sample containing both phases, as shown in Figure 8.19. The amount of caesium was chosen to be less than necessary to show superstructure spots in LEED. Most of the surface displays adatoms as shown in Figure 8.19(a). From a self-correlation analysis the smallest nearest neighbour distance was found to be 1.16 nm, some regions show less dense adatom arrangements. An image where adatoms and another, homogeneous area could be found side by side is shown in Figure 8.19(b). While adatoms can be found in the upper right and lower left, the middle of the sample contains a flat broad stripe with some trenches inside, that have adatoms inside. Note, that this adatoms seem to be equidistant arranged within the trenches. Adatoms in regions where the trenches end up in a broad flat area could be removed by changing the tunnelling parameters. After removal of the adatoms,

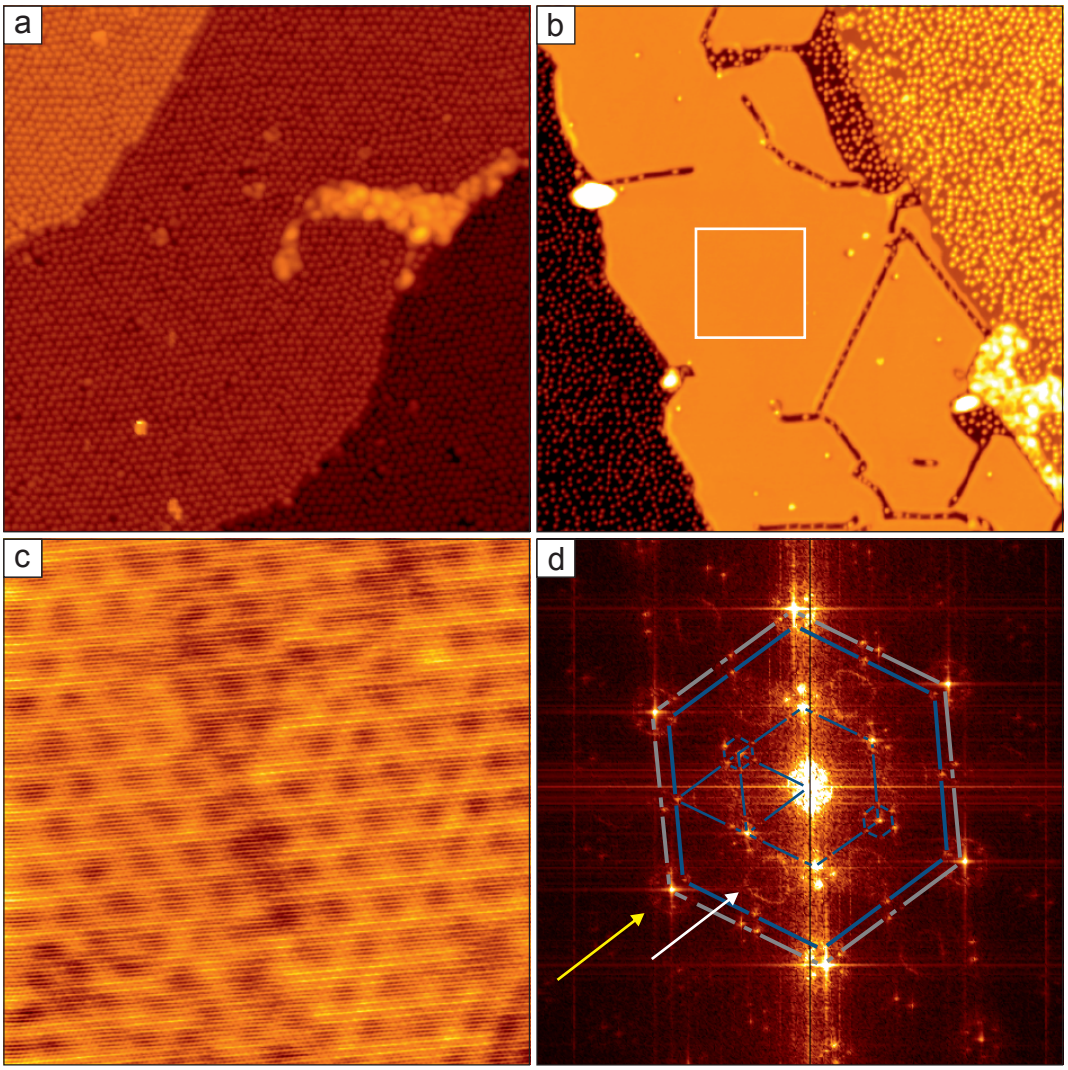

Figure 8.19: STM measurements of graphene after Cs deposition. A small amount of Cs was deposited, which was slightly less than necessary for superstructure spots in LEED. Most of the sample was covered with adatoms (a). Some regions on the sample show intercalated areas and adatoms side by side (b,c). The atomic structure of the intercalated area was atomically resolved at the white square, shown in (c). Fourier transform (d) of image (c). Bias voltage was (a) 1.1 V, (b) 1.5 V, (c) 0.04 V. Image width is (a) 74.7 nm, (b) 111 nm, (c) 18.7 nm, (d) 21 nm^{-1}. Images taken at 6.5 K.

these regions consist of pristine graphene on iridium, indicating that the graphene is still intact at the trenches . A measurement at the position of the white box in Figure 8.19(b) leads to Figure 8.19(c), where the hexagonal lattice of graphene is clearly visible [see also the enlarged image in Fig. 9.5(a), Sec. 9.2]. The Fourier transform of the atomically resolved image is shown in Figure 8.19(d). Carbon related spots are highlighted by the grey hexagon, while the outer blue hexagon represents the iridium substrate periodicity.

The spots within the hexagons can be related to a $(2 \times 2)_{\mathrm{Ir}}$ superstructure. Note, that a circular and a triangular contour is visible as depicted by the yellow and white arrow, respectively, which will be discussed in Section 9.2.

Both, the integrity of the graphene layer as well as the occurrence of trenches are strong indications that the γ region must be an intercalated area [48]. From the STM and LEEM images it can be concluded that after the graphene layer is covered with adatoms up to a critical density the atoms sweep under the graphene layer leading to an intercalated sample.

STM measurements of wrinkles from pristine graphene are presented in Figure 8.20. A first indication for defects within a wrinkle is the fact that wrinkles seem to be cracked at some sections [arrows in Fig. 8.20(a)], yet we did not obtain images in atomic resolution to rule out other explanation. However, at crossings of wrinkles the wrinkle network clearly seems to be broken, as can be seen in the STM image in Figure 8.20(b). A cross section of the wrinkle that is indicated by the arrow, is shown in Figure 8.17(c). The surface drops

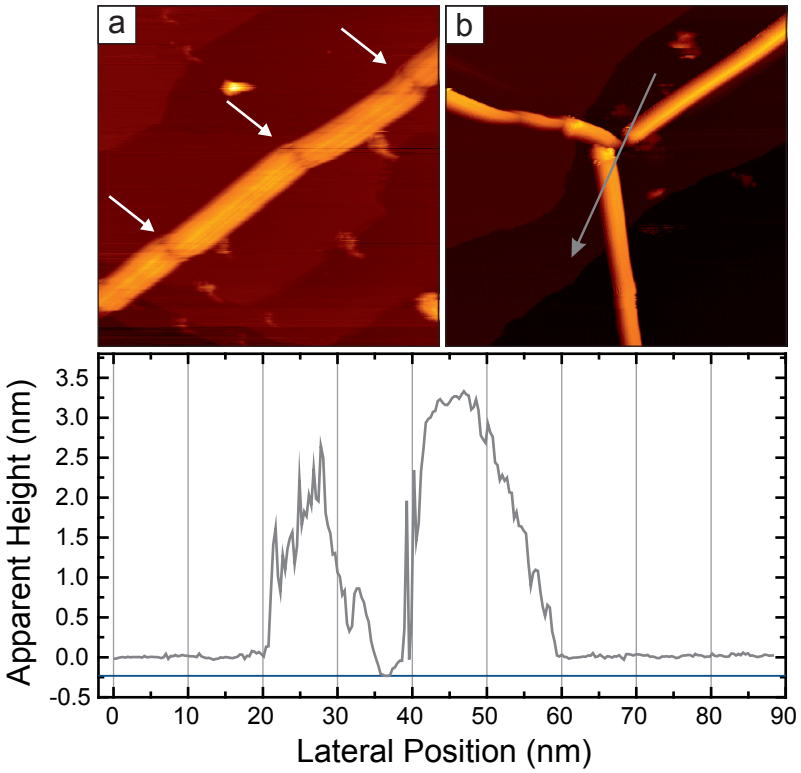

Figure 8.20: STM topographs of wrinkles. Wrinkles are splitted in several sections, as indicated by darker lines perpendicular to the wrinkle direction (a). At crossing points the wrinkle network is broken (b). A cross section (c) from image (b) reveals, that the graphene layer is partly cracked at the crossing as the height goes down to the substrate level (blue line).

down to $-0.23\,\mathrm{nm}$ in the centre where the wrinkle crossing is located. This lowering in height can be related to a hole in the graphene sheet, as iridium vacancy islands are not found on this kind of samples. The appearance of cracks and holes within the graphene layer can explain the process of intercalation of atoms even through a graphene sample with full coverage.

Conclusively, the question why intercalation takes place for graphene could be clarified. Etching of the graphene sheet due to caesium atoms can be ruled out as atomically resolved STM images reveal a perfectly intact graphene lattice [Fig. 8.19(c)]. Moreover the cracks and holes at wrinkles were seen for pristine graphene, so the explanation by this kind of holes in the sheet is not limited to specific atoms.

8.3.1 Europium Intercalated Graphene

In this section the atomic structure of europium intercalated graphene is analysed. The in-plane structure of this system was shown to arrange for increasing amount of europium intercalants in the phases $(2 \times 2)_{\mathrm{gr}}$, $\sqrt{3}_{\mathrm{Ir}}$, and $\sqrt{3}_{\mathrm{gr}}$ [48]. To get information about the out-of-plane structure XSW measurements were performed. Two samples were prepared by a single TPG step at 1400 K and CVD to full coverage at 1120 K, followed by the deposition of europium. The deposition was carried out at elevated sample temperatures to obtain intercalation of a full layer of europium as well as to enable back evaporation of residual adatoms in order to have a well defined intercalation system. The nominal deposited amount for sample ① was 2.8 $\mathrm{ML_{gr}}$ at 700 K and for sample ② it was 0.36 $\mathrm{ML_{gr}}$ at 760 K. Note, that due to the elevated sample temperature during deposition the back evaporation of adatoms lowers the amount of intercalated atoms. For sample ① a full layer in the densest structure $\sqrt{3}_{\mathrm{gr}}$ was prepared, for that the deposited amount was chosen to be almost ten times higher than necessary. The in-plane structure of both samples was investigated by LEED, while the actual amount was checked by a quantitative XPS analysis, as will be described below.

LEED images of both samples are shown in Figure 8.21. The measurement of the pristine graphene layer [Fig. 8.21(a)] reveals a high structural quality without rotational domains. While for the high amount of intercalated europium [Fig. 8.21(b)] $\sqrt{3}_{\mathrm{gr}}$ superstructure spots are clearly visible, for the low amount [Fig. 8.21(c)] no superstructure spots can be found. However, both samples show weakened moiré satellites compared to the image of pristine graphene. Hence, it is confirmed by LEED, that sample ① was prepared with the maximum amount of intercalated europium in the $\sqrt{3}_{\mathrm{gr}}$ phase. From the vanishing

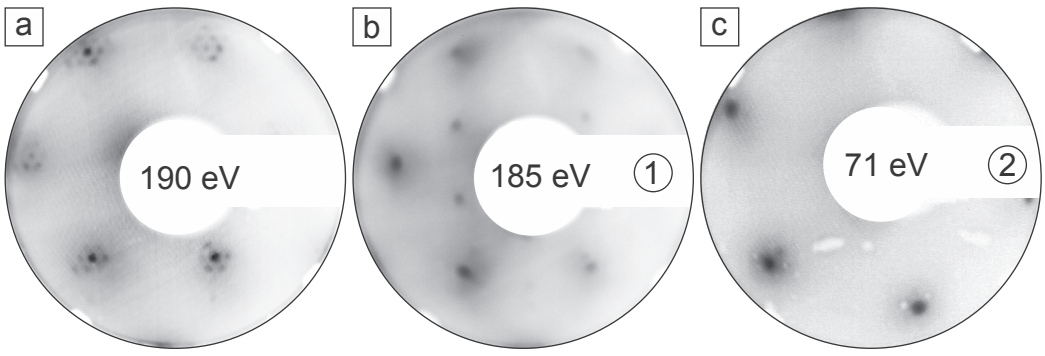

Figure 8.21: LEED images of Eu intercalated gr/Ir(111). Image (a) shows the sample before and (b,c) after the intercalation process. The deposited amount was (b) 2.8 $\mathrm{ML_{gr}}$ (sample ①) and (c) 0.36 $\mathrm{ML_{gr}}$ (sample ②).

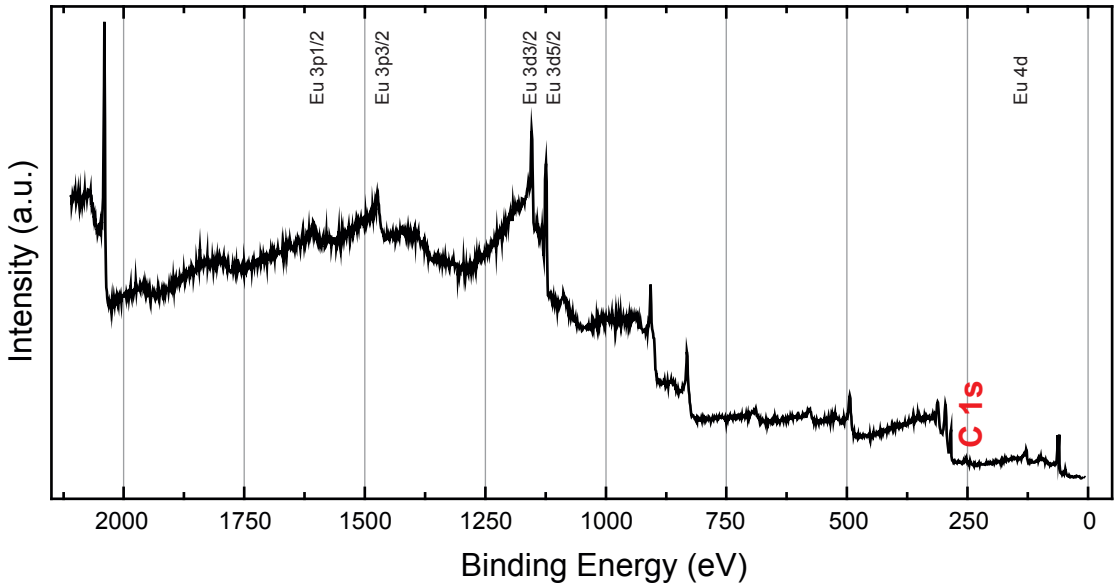

Figure 8.22: XPS survey scan of gr/Eu/Ir(111). Beside the Ir and C 1s core level peaks (comp. Fig. 8.2) newly emerged Eu related core levels can be seen. The most prominent Eu core level are labelled. Photon energy was 2810 eV.

moiré spots it can be concluded that intercalation also took place for sample ② leading to at least a high fraction of $(2 \times 2)_{\mathrm{gr}}$ structure as the moiré satellites vanished. Yet, from these LEED measurements one question remains whether sample ② is fully or just partly intercalated with the $(2 \times 2)_{\mathrm{gr}}$ interface layer.

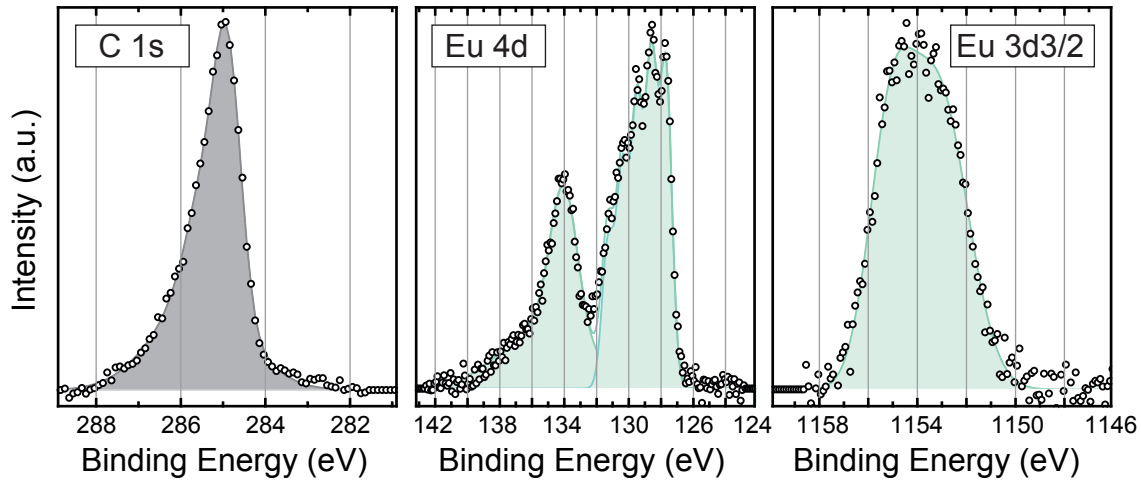

Figure 8.23: XPS measurements at gr/Eu/Ir(111). Background substracted raw data is shown as circles, the fit to the data as solid line. Europium related fits are shown in aquamarine, the C 1s core level fit in grey. Photon energy was 2810 eV.

The chemical quality of the sample was checked by an XPS survey scan, which is shown in Figure 8.22. Beside the iridium features described in Section 8.1 also europium peaks are present in the spectrum, whose most prominent ones are labelled. As the survey spectrum does not show additional peaks contaminations can be ruled out.

XSW measurements were performed at the Eu $3d_{3/2}$, Eu 4d, as well as the C 1s core level. XPS measurements with high measurement point density are shown in Figure 8.23. The raw data (circles) is well described by the fit (coloured lines). The graphene related spectrum is grey coloured while europium related ones are shown in aquamarine. The Eu 4d core level shows the characteristic splitting due to multiplet interactions [50]. The binding energy of the C 1s core level is (284.99 ± 0.06) eV in case of the $(2 \times 2)_{\mathrm{gr}}$ structure and (284.91 ± 0.07) eV for the $\sqrt{3}_{\mathrm{gr}}$. The binding energies of these core levels are discussed in Section 9.1.

To reveal the superstructure of sample ② the amount of intercalated europium of sample ① can be used as a reference. Sample ① is certainly fully intercalated exhibiting a $\sqrt{3}_{\mathrm{gr}}$-superstructure. Hence, the ratio of the total photoelectron yield of the C 1s core level to the Eu $4d_{3/2}$ can be compared for both samples as they have the same graphene coverage. Following this procedure the uncertainty of the cross sections as well as systematic ex-

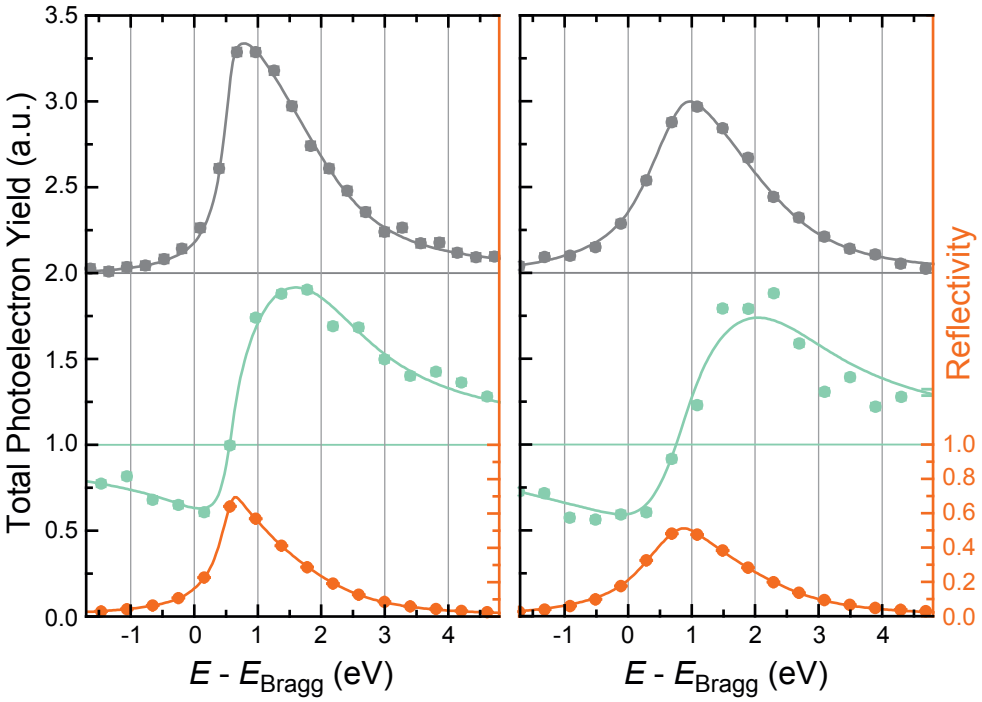

Figure 8.24: XSW results for gr/Eu/Ir(111). Graphene and europium related curves are presented in grey and aquamarine, the reflectivity curves in orange. Diagram (a) refers to sample ①, and (b) to sample ②.

perimental errors cancel out. The average ratio from sample ① is 0.085 ± 0.004, while it is 0.060 ± 0.004 for sample ②. This means, that the amount of europium of sample ② is (0.703 ± 0.055) of the amount of sample ①. Bearing in mind that the coverage for a $\sqrt{3}_{\mathrm{gr}}$ superstructure is $0.33\,\mathrm{ML_{gr}}$, while for a $(2 \times 2)_{\mathrm{gr}}$ it is $0.25\,\mathrm{ML_{gr}}$, the coverage of sample ② can be calculated to $0.7 \times 0.33 = (0.231 \pm 0.039)\,\mathrm{ML_{gr}}$. Hence, it results in a fraction of $92.4\,\%_{(2\times2)}$ in the $(2 \times 2)_{\mathrm{gr}}$ superstructure. Conclusively, the quantitative analysis of the XPS measurements verifies that sample ② is almost fully intercalated with a $(2 \times 2)_{\mathrm{gr}}$ superstructure. Note that the amount of intercalated europium can also be clarified by a quantitative XPS analysis. In general this can be done by using values of the cross section of these core levels that are tabulated in References [83, 84], but as the photon energy is significantly different from those listed in literature these values can not be used for a precise coverage determination. Interpolation of the listed data also leads to meaningless results, as the errors might be caused due to experimental details.

The XSW analysis of each series of XPS spectra of the Eu $4d_{5/2}$, Eu $4d_{3/2}$, Eu $3d_{3/2}$ as well as the C 1s core levels lead to the XSW curves depicted in Figure 8.24. The data is shown as circles and the fits as solid lines. Graphene is represented in grey, europium in aquamarine, and the reflectivity curve in orange. For better illustration the graphene related curve is shifted by one, and the corresponding values of one are shown as faint lines in respective colours. In all cases the fits are in very good agreement with the data. The average results of all XSW measurements are presented in Table 8.4.

From the measured values the height difference between the europium atoms and graphene can be determined, which is 2.60 Å in the $\sqrt{3}_{\mathrm{gr}}$ superstructure and 2.73 Å in the $(2 \times 2)_{\mathrm{gr}}$ superstructure. In Figure 8.25 these results are shown in a simple model according to the space-filling model. The atoms are depicted to scale using empirical atomic radii [80]. A comparison of the distances of europium to graphene and iridium shows that the europium atoms are significantly closer to the substrate than to the graphene layer, although the superstructure is formed with respect to graphene.

Table 8.4: XSW results of gr/Eu/Ir(111). Average results for the $\sqrt{3}_{\mathrm{gr}}$ superstructure come from five and two measurements for Eu and gr, respectively. For the $(2 \times 2)_{\mathrm{gr}}$ superstructure three and one measurements were done for Eu and gr, respectively.

Sample	**Structure**	**Species**	$P^{(111)}$	$F^{(111)}$	**height**
①	$\sqrt{3}_{\mathrm{gr}}$	Eu	0.12 ± 0.01	0.78 ± 0.04	(2.49 ± 0.02) Å
①	$\sqrt{3}_{\mathrm{gr}}$	gr	0.30 ± 0.01	0.57 ± 0.04	(5.09 ± 0.02) Å
②	$(2 \times 2)_{\mathrm{gr}}$	Eu	0.10 ± 0.01	0.88 ± 0.04	(2.43 ± 0.02) Å
②	$(2 \times 2)_{\mathrm{gr}}$	gr	0.33 ± 0.01	0.42 ± 0.04	(5.16 ± 0.02) Å

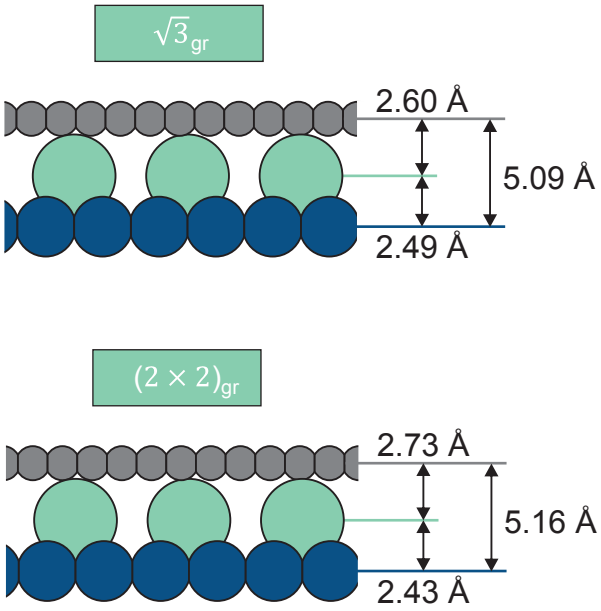

Figure 8.25: Sketch of gr/Eu/Ir(111). Simple sphere model according to the space-filling model. Atoms are printed to scale using empirical atomic radii [80]. Graphene atoms are printed in grey, europium atoms in aquamarine, and iridium atoms in midnightblue. Note, that the section view does not reproduce the real crystal structure of graphene.

The results of the XSW measurements can be compared to the distances present in the graphite intercalation compound. In analogy to the model shown in Figure 8.25 the graphite intercalation compound is modelled in Figure 8.26. The distance between the graphene layer and the europium atoms was determined from the lattice constant of the GIC unit cell (EuC_6) [85] and results to 2.44 Å. Conclusively, the influence of the intercalants for the graphene intercalation compound is weaker than for the graphite intercalation compound.

From DFT calculations for the (2×2) and the $\sqrt{3}$ superstructure [86] the positions of the europium atoms and graphene are extracted [87] and presented in Table 8.5. The calculation was performed for a commensurate unit cell where the carbon bonds are stretched, while the iridium bonds are compressed to match an equal bond length of 2.47 Å in order to reduce the computational load. In both the experimental data and the calculations, the distance of the europium atoms to the substrate as well as the distance

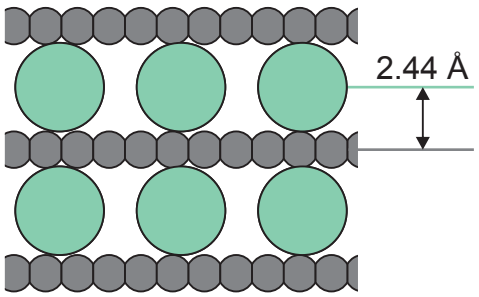

Figure 8.26: Sketch of Eu-GIC. Simple sphere model according to the space-filling model. Atoms are printed to scale using empirical atomic radii [80]. Graphene atoms are printed in grey, and europium atoms in aquamarine. Note, that the section view does not reproduces the real crystal structure of graphite. The atomic distance was extracted from Ref. [85] (see text).

Table 8.5: Comparison of theoretical and experimental results for Eu-grIC. From a DFT calculation [86] the resulting heights [87] for the Eu atoms, the gr layer, as well as the distance Δh between Eu and gr are shown for the (2×2) and the $\sqrt{3}$ superstructure. The experimental results are presented for comparison. Note that the accuracy of the XSW results is 0.02 Å.

	DFT calculation			**XSW results**		
structure	Eu	Δh	gr	Eu	Δh	gr
$\sqrt{3}$	2.68 Å	2.58 Å	5.26 Å	2.49 Å	2.60 Å	5.09 Å
(2×2)	2.66 Å	2.63 Å	5.29 Å	2.43 Å	2.73 Å	5.16 Å

between europium and graphene is larger for the $(2 \times 2)_{\mathrm{gr}}$ structure. Note that the calculated graphene-europium distances are lower, namely by 0.02 Å for $(2 \times 2)_{\mathrm{gr}}$ and by 0.10 Å for $\sqrt{3}_{\mathrm{gr}}$. As a matter of fact, it is not expected that the DFT results fit perfectly to the experimental data as the unit cell is deformed for calculability reasons.
On first sight, it is surprising, that the graphene layer resides closer to the europium atoms in case of a higher europium coverage in the $\sqrt{3}$ structure. From ARPES measurements the shift of the Dirac point is determined [88] as listed in Table 8.6. For this doping the electron transfer is extracted from an integrated density of states calculation [87], revealing the stronger charging for the $\sqrt{3}_{\mathrm{gr}}$ structure. Hence, the reduced distance can be explained by a stronger attractive electrostatic force. However, for a complete discussion the charging of the europium atoms has to be determined as well.

Table 8.6: Doping and electron transfer for Eu-grIC. The doping was determined by measuring the shift of the Dirac point in ARPES [88]. The electron transfer to the gr unit cell was extracted from integrated density of states calculations in a tight-binding approximation [87].

structure	**doping** [88]	**electron transfer** [87]
$\sqrt{3}_{\mathrm{gr}}$	$-1.43\,\mathrm{eV}$	$0.146\,\mathrm{e}^-$
$(2 \times 2)_{\mathrm{gr}}$	$-1.36\,\mathrm{eV}$	$0.127\,\mathrm{e}^-$

8.3.2 Caesium Intercalated Graphene

In order to reveal the in-plane structures of caesium intercalated graphene a series of samples with increasing caesium coverage was prepared. The determination of the deposited amount is difficult as the vapour pressure is rather high, meaning that a high portion of deposited caesium might evaporate directly back into the vacuum. This was found during rate calibration, as the rate decreases over time for constant dispenser current, which reaches the highest rate again after a long break of evaporation. Therefore the deposited amount is presented by evaporation rate at the beginning, dispenser current, and duration, as the time used for preparation is of big importance (see also Section 6.2.1 for details).

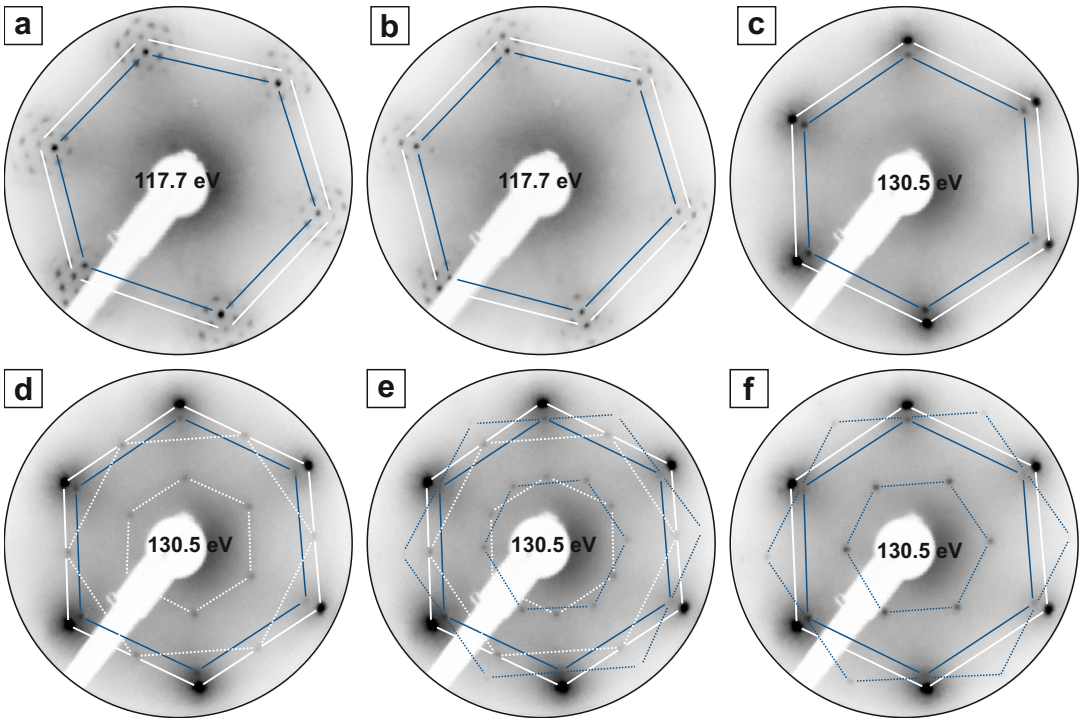

Figure 8.27: LEED measurement of a Cs deposition series. Distortion corrected LEED images of graphene before (a) and after deposition of Cs (b)-(f). Beam energies are written in the center. The blue lines correspond to Ir related spots, the white lines are graphene related. Solid lines are used for the primitive unit cells, dashed lines are used for superstructure unit cells. Pristine graphene shows the hexagonal structure with moiré spots surrounding C and Ir spots. In (b) and (c) the moiré spots are less intense. To allow direct comparison no contrast modification was done for (a) and (b). Higher amount of deposited Cs leads to superstructures in the images: (d) pure $(2 \times 2)_{\mathrm{gr}}$, (e) mixture of $(2 \times 2)_{\mathrm{gr}}$ and $\sqrt{3}_{\mathrm{Ir}}$, and (f) pure $\sqrt{3}_{\mathrm{Ir}}$. The start deposition rate was 0.53 Å/min at a dispenser current of 10.0 A (b) and 4.8 Å/min at a dispenser current of 6.0 A (c)-(f), the deposition times were (b) 180 s, (c) 10 s, (d) 300 s, (e) 450 s, (f) 600 s.

Starting with a fully closed graphene layer a caesium deposition series was measured by LEED as shown in Figure 8.27. Here, carbon related spots are highlighted by white lines and iridium related ones by blue lines. While for the fully closed layer [Fig. 8.27(a)] the moiré satellites have a rather high intensity for the deposition of a small amount of caesium [Fig. 8.27(b)] their intensity drops down and they almost vanish [Fig. 8.27(c)]. Further deposition reveals superstructures, indicated by dashed lines, that change for increasing amount of deposited caesium. A pure carbon related $(2 \times 2)_{\mathrm{gr}}$ [Fig. 8.27(d)] superstructure turns up first, followed by the appearance of an additional superstructure leading to a mixture of $(2 \times 2)_{\mathrm{gr}}$ and $\sqrt{3}_{\mathrm{Ir}}$ [Fig. 8.27(e)]. Finally the $(2 \times 2)_{\mathrm{gr}}$ disappears resulting in a pure $\sqrt{3}_{\mathrm{Ir}}$ superstructure [Fig. 8.27(f)].

Furthermore STM measurements were performed to investigate the structure of the caesium intercalants. In some regions additionally to the superstructures found by LEED also a $(2 \times 2)_{\mathrm{Ir}}$ superstructure was found by a Fourier analysis (see Fig. 8.19(d) in Sec. 8.3). Conclusively, the possible structures for the caesium intercalated graphene can be depicted in a phase diagram as shown in Figure 8.28. From this diagram the surface

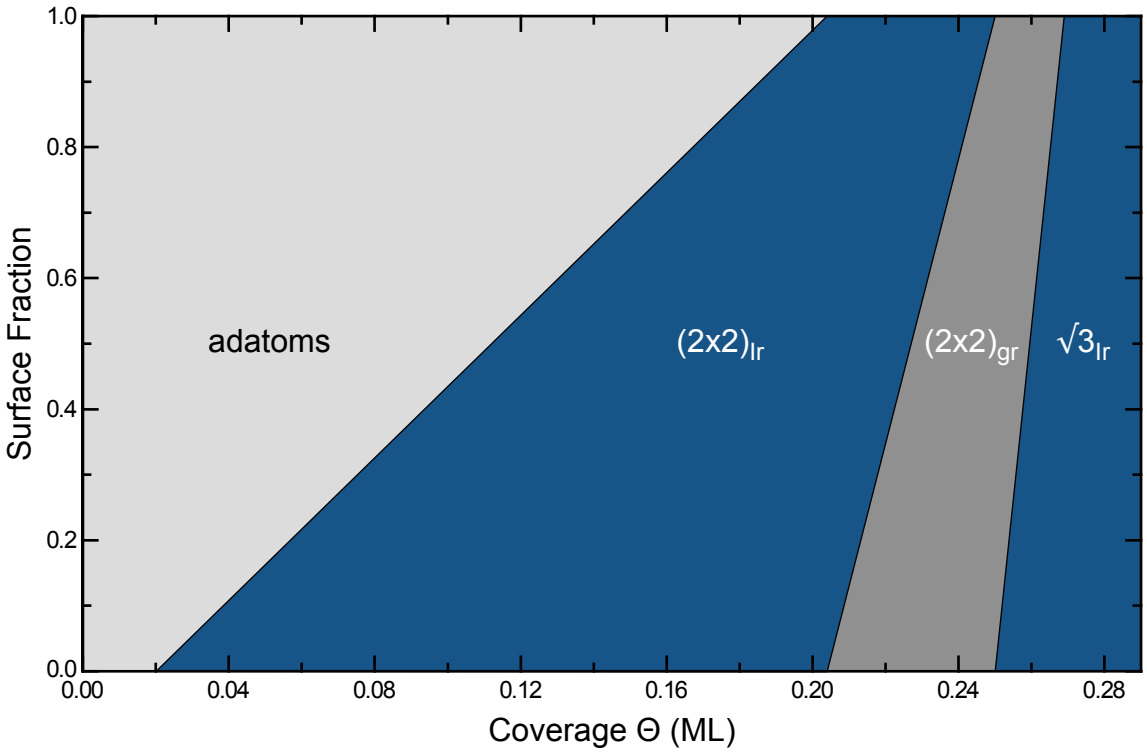

Figure 8.28: Phase diagram of the Cs-grIC. From the Cs coverage the surface fraction of the possible structures can be extracted. The light grey area corresponds to the adatom phase, the blue to Ir related supterstructures, i.e. $(2 \times 2)_{\mathrm{Ir}}$ and $\sqrt{3}_{\mathrm{Ir}}$, and the grey one to a $(2 \times 2)_{\mathrm{gr}}$.

fraction of the concurring superstructures for the deposited amount of caesium can be extracted.

During the STM experiment it was found that the superstructure seems to be not perfectly stable, leading to a change as depicted in Figure 8.29. This is remarkable, as the tip induces structural changes underneath the graphene layer, even at 6.5 K. After the measurement of the overview area [Fig. 8.29(a)] at several regions the superstructure changed like shown for the section indicated by the white square [Fig. 8.29(b)]. Further scanning leads again to a change of the newly emerged pattern [Fig. 8.29(c)]. A cross section as indicated by the arrow reveals that this pattern comes along with an increase of the apparent height of approx. 1 Å. The section inside the white box [Fig. 8.29(c)] is depicted in Figure 8.29(e) and shows also ±15° rotated contributions in the fourier transform image [Fig. 8.29(f)] beside the well-aligned $(2 \times 2)_{gr}$ superstructure.

As the increase in the apparent height of 1 Å is too low for a second intercalation layer this rearrangement of the caesium atoms might be related to a change of the local density

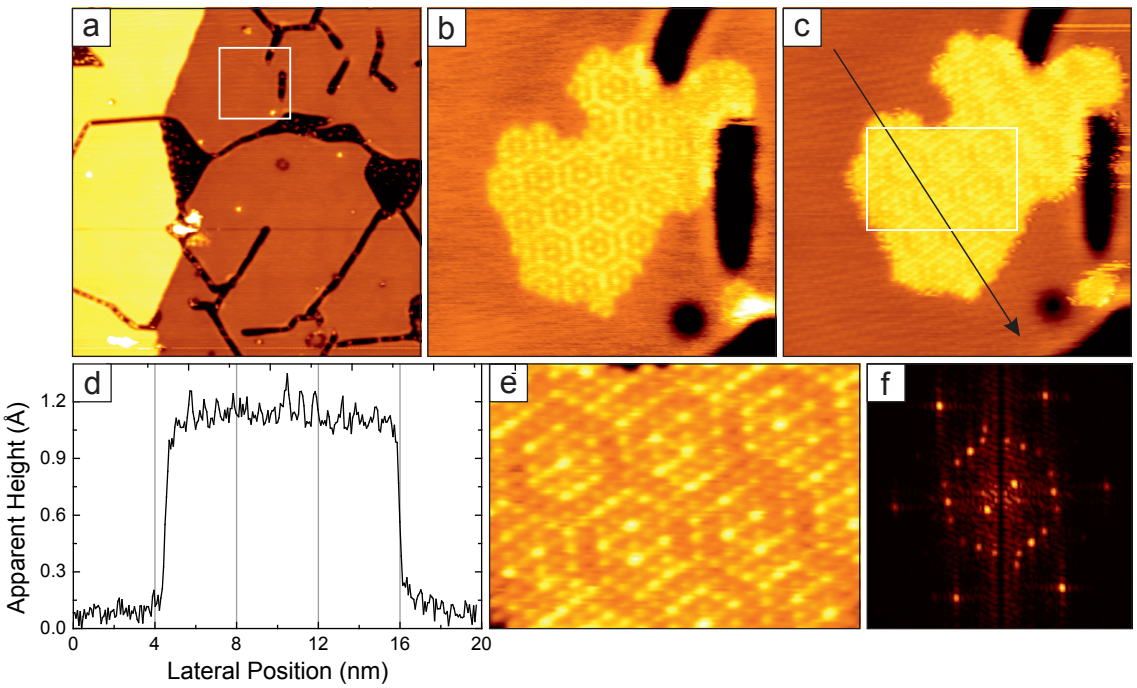

Figure 8.29: STM topographs of Cs intercalated graphene. After scanning image (a) a new structure appears in the area highlighted by a white box, shown in (b). A subsequent scan is shown in (c). A close-up topograph of the white area is shown in (e). The Fourier transform (f) shows a $(2 \times 2)_{gr}$ superstructure, aligned to graphene and also rotated by approx. ±15°. A cross section from (c) (black arrow) is shown in (d). The apparent step height is about 1 Å. The image sizes are (a) 96.3 nm × 96.3 nm, (b,c) 20 nm × 20 nm, (e) 8.3 nm × 5.9 nm, and (f) 7.2 nm^{-1} × 7.2 nm^{-1}. Tunnelling parameters are $U = 1.5$ V and $I = 0.1$ nA.

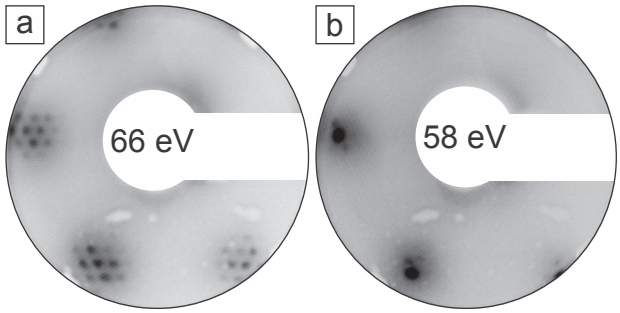

Figure 8.30: LEED images of gr/Cs/Ir(111). Images were taken at ID32 before the XSW measurements were performed. Gr sample before (a) and after (b) deposition of Cs for 230 s at a start deposition rate of 2.0 Å/min and a dispenser current of 5.2 A.

of states. However, unless this structure can not be prepared on large scales an enlarged density of states will not be detectable as e.g. stronger doping in ARPES. The real nature of this newly emerged pattern can be clarified by further tunnelling spectroscopy experiments.

After the in-plane structure is revealed by LEED and STM experiments, the out-of-plane structure is analysed by XSW. For this caesium was deposited onto a fully closed graphene layer. During the rate calibration for this experiment the rate decreased from 2.0 Å/min to 0.88 Å/min, while the dispenser current was constant at 5.2 A over this time. The deposition time was 230 s. The quality of the sample was checked by a LEED measurement, which is shown in Figure 8.30. Prior to caesium intercalation the pristine graphene sample shows the characteristic sharp carbon and iridium surrounded spots surrounded by moiré satellites. Thus, on this sample there is no indication for rotated domains. After intercalation [Fig. 8.30(b)] the contrast of the moiré satellites weakens, but no superstructure spots are visible as might be expected from the experiments discussed earlier. Hence, from LEED the superstructure of the intercalants remains unclear. However, from the estimation of the deposited amount it can be concluded that the sample should be fully intercalated with a high probability for the $\sqrt{3}_{\mathrm{Ir}}$ structure.

The chemical composition of the sample is analysed by an XPS survey scan as shown in Figure 8.31. It consists of the characteristic peaks from the iridium substrate and graphene (comp. Fig. 8.2). Furthermore, core levels from caesium can be assigned. The most prominent ones are labelled in the top row.

The C 1s, Cs 3d, and Cs $4p_{3/2}$ core levels were measured with higher density of measuring points and are shown in Figure 8.32, where data points are shown as circles and the fits by solid lines. In the diagrams the colour grey is used for graphene and purple for caesium, respectively. The data is obviously well described by the fits, whose area represents the total photoelectron yield. The C 1s binding energy is located at (285.05 ± 0.05) eV, which will be discussed in Section 9.1.

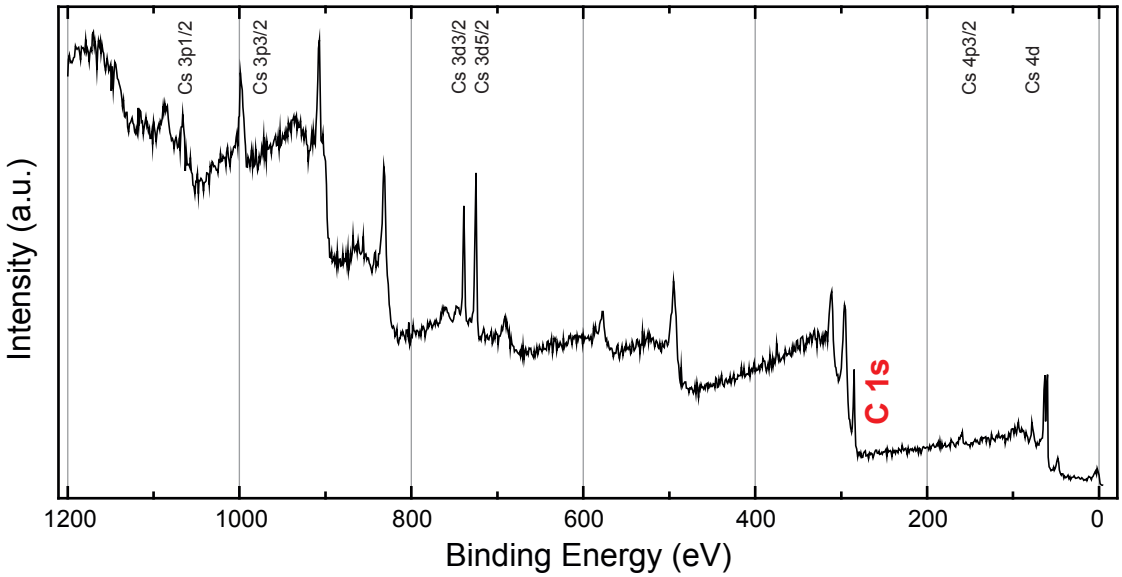

Figure 8.31: XPS survey scan of gr/Cs/Ir(111). Beside the Ir core level peaks (comp. Fig. 8.2) also the C 1s and Cs related core level can be seen. The most prominent Cs core levels are named. Photon energy was 2810 eV.

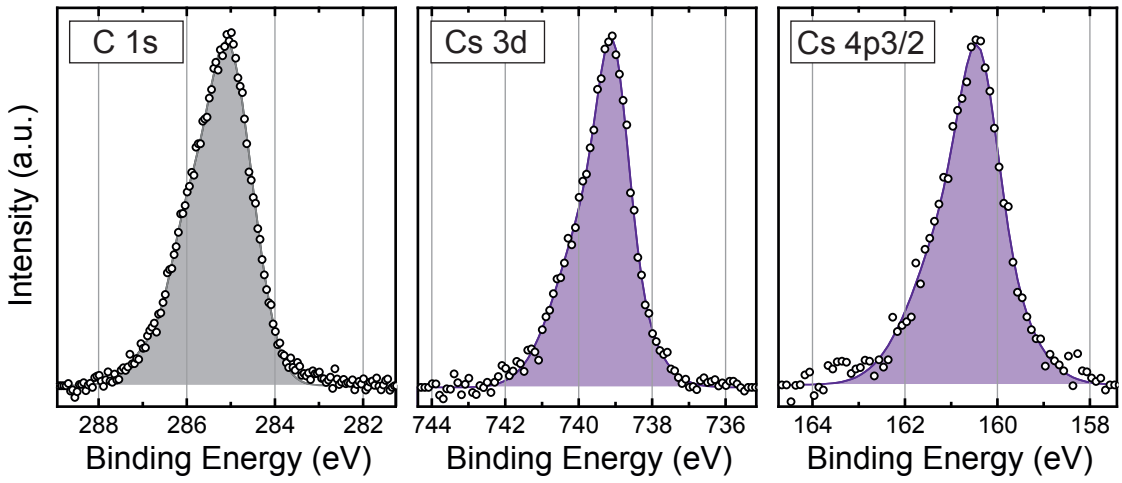

Figure 8.32: XPS measurement at gr/Cs/Ir(111). Spectra of the C 1s (grey), Cs 3d, and Cs $4p_{3/2}$ (both purple) core levels. Photon energy was 2810 eV.

Table 8.7: XSW results of gr/Cs/Ir(111). Results for gr and Cs atoms, coming from one and averaged from four single measurements.

Species	$P^{(111)}$	$F^{(111)}$	height
gr	0.83 ± 0.01	0.51 ± 0.04	(6.27 ± 0.02) Å
Cs	0.38 ± 0.01	0.54 ± 0.04	(3.05 ± 0.02) Å

The series of spectra from XPS was fitted for each core level leading to the XSW curves as presented in Figure 8.33. The fitting parameters coherent position $P^{(111)}$ and coherent fraction $F^{(111)}$ are presented in Table 8.7, where also the values for the heights of the respective atoms are given.

For better illustration the resulting heights from Table 8.7 are drawn in a sketch in Figure 8.34. The distance between graphene and the caesium intercalant layer results to 3.22 Å. This distance is significantly larger than the 2.98 Å, found in the Cs-GIC [89]. Hence, it can be concluded that the influence of the intercalant layer to the graphene sheet is smaller than in the GIC. Moreover, for the Cs-grIC Dirac electron scattering is observed, which will be presented in Section 9.2.

In order to clarify the question of the deposited amount of caesium the C 1s core level was fitted with two peaks, where one peak was fixed to the binding energy of pristine graphene, whereas no constraints were applied to the second one. This analysis leads to randomly distributed heights. Hence, it can be ruled out that non-intercalated areas were present on the sample, as in case that some areas of graphene would be not intercalated

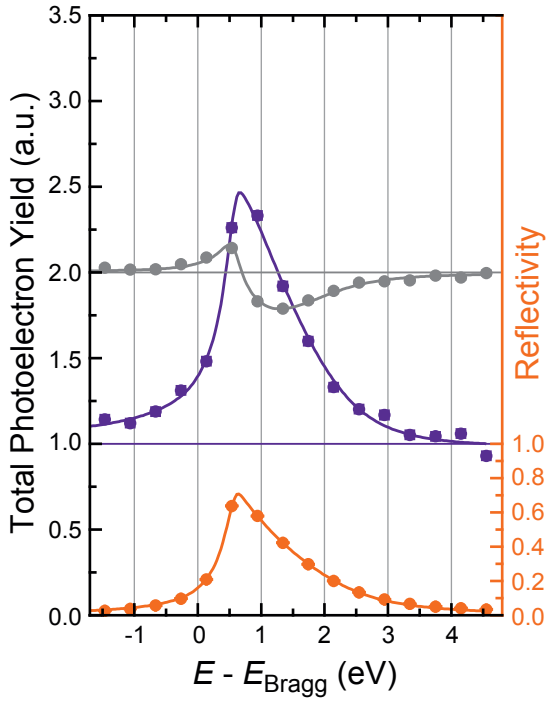

Figure 8.33: XSW curve of gr/Cs/Ir(111). XSW curve for gr (grey) and Cs (purple). The reflectivity is shown in orange. In case of gr values are shifted by 1 for better illustration. Corresponding values of 1 are shown as faint solid lines in respective colours.

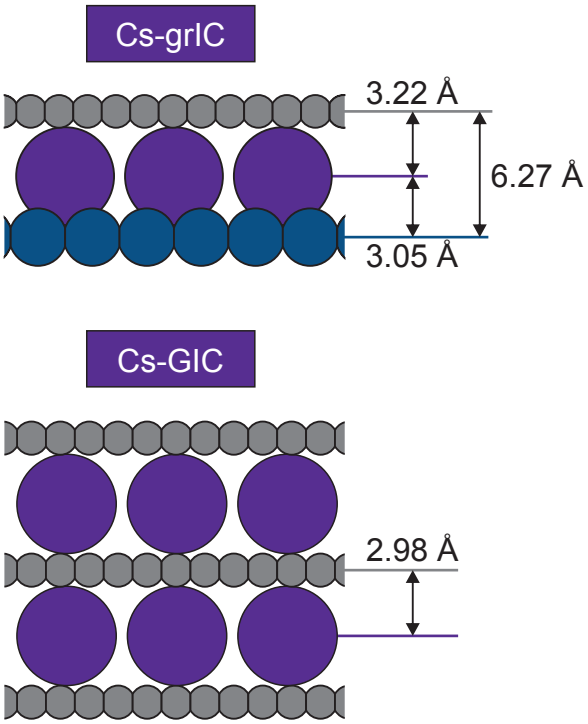

Figure 8.34: Sketch of the Cs-grIC and Cs-GIC. Simple sphere model according to the space-filling model. Empirical atom sizes [80] and distances are to scale. Ir substrate atoms are coloured blue, Cs purple, and gr grey. Distance for the GIC taken from Ref. [89].

an XSW analysis of the first peak would lead to a specific height close to the result of pristine graphene. Nevertheless, the exact type of superstructure remains unclear.

DFT calculations including van der Waals force were performed for caesium intercalated graphene using an expanded graphene sheet, while the iridium substrate is compressed in order to lead to an commensurate unit cell [49]. The results of the positions for caesium atoms, graphene, as well as the distance between the intercalants and the graphene layer for different superstructures [90] are shown in Table 8.8. As the unit cell is deformed for reasons of calculability a deviation to the experimental data is expected. Nevertheless, for the $\sqrt{3}$ structure the DFT result is in very good agreement with the experimental data,

Table 8.8: Comparison of theoretical and experimental results for Cs-grIC. From a DFT simulation [49] the resulting heights [90] for the Cs atoms, the gr layer, as well as the distance Δh between Cs and gr are shown for the $(2 \times 2)_{\mathrm{gr}}$, the $(3 \times 3)_{\mathrm{gr}}$, and the $(4 \times 4)_{\mathrm{gr}}$ superstructure. The experimental results are presented for comparison.

	DFT calculation			XSW results		
structure	Cs	Δh	gr	Cs	Δh	gr
(4×4)	3.40 Å	3.33 Å	6.73 Å			
(3×3)	3.40 Å	3.34 Å	6.74 Å			
(2×2)	3.21 Å	3.50 Å	6.71 Å	3.05 Å	3.22 Å	6.27 Å
$\sqrt{3}$	3.14 Å	3.20 Å	6.34 Å			

Table 8.9: Doping and electron transfer for Cs-grIC. The doping was determined by measuring the shift of the Dirac point in ARPES [88]. The electron transfer to the gr unit cell was extracted from integrated density of states calculations in a tight-binding approximation [87].

structure	**doping** [88]	**electron transfer** [87]
$\sqrt{3}_{\mathrm{gr}}$	$-1.20\,\mathrm{eV}$	$0.094\,\mathrm{e}^-$
$(2\times 2)_{\mathrm{gr}}$	$-1.13\,\mathrm{eV}$	$0.082\,\mathrm{e}^-$

which gives rise to the assumption that a high fraction of the intercalated caesium has formed the $\sqrt{3}$ structure. This assumption is further supported by DFT, as there is a big difference to the heights determined for the (2×2) or less denser structures. Moreover, intercalated stuctures less dense than in the (2×2) structure are not observed by STM and LEED measurements as described above.

The doping level was extracted from ARPES measurements for both superstructures of interest by measuring the shift of the Dirac cone [88]. The doping as well as the corresponding charge transfer is listed in Table 8.9. For the $\sqrt{3}_{\mathrm{gr}}$-structure the electron transfer is larger than for the $(2\times 2)_{\mathrm{gr}}$-structure. Note, that the distances between graphene and caesium calculated by DFT shows that the distance decreases for increasing amount of intercalants. Hence, it can be concluded that beside the van-der-Waals force also the electrostatic force is important for the binding of the graphene layer to the intercalants, as it was also the case for the europium intercalated samples.

8.3.3 Oxygen Intercalated Graphene

In this section the distance between the oxygen intercalants and the covering graphene layer is investigated. For this purpose XSW measurements were performed revealing the layer positions above the substrate. A sample with a graphene coverage of 53 %, prepared by three TPG steps at a flash anneal temperature of 1390 K, was intercalated by oxygen dosing ($p_{O_2} = 10^{-5}$ hPa, 100 s) at a temperature between 530 K and 620 K (see Sec. 6.2.3). To prove the success of the intercalation process LEED measurements were performed before and after oxygen dosing (see Figure 8.35). While the pristine graphene islands show the typical sharp carbon and iridium related spots surrounded by moiré satellites [see Fig. 8.35(a)], the intensity of the moiré satellites weakens significantly after oxygen intercalation [see Fig. 8.35(b)], similar as in case of the other graphene intercalation compounds (compare Sec. 8.3.2 and Sec. 8.3.1).

The chemical composition of the sample was investigated by XPS survey scans, as shown in Figure 8.36. Beside the iridium related core levels (compare Fig. 8.2) the C 1s and O 1s core levels can clearly be seen. As there are only the expected core level peaks present contaminations can be ruled out.

The C 1s and O 1s core levels were measured with higher measurement point density for the associated XSW analysis, as depicted in Figure 8.37. The XPS data is shown as circles and nicely described by the fits (solid lines). The O 1s spectrum shows two seperated peaks: A broad one at about 532 eV (light red) and a sharp one at about 530 eV (dark red). The dark red peak can be assigned to O 1s from O/Ir(111), as the binding energy of the O 1s electron for oxygen adsorbed on iridium is 529.9 eV [21]. For completeness both peaks found in the O 1s spectrum are analysed separately within the XPS series for the XSW experiment. The binding energy of the C 1s core level is (284.13 ± 0.10) eV, which is discussed in Section 9.1.

The results of the XSW measurements for the oxygen intercalated sample are shown in Figure 8.38. The data is shown as circles, the fits as solid lines. From these fits the values

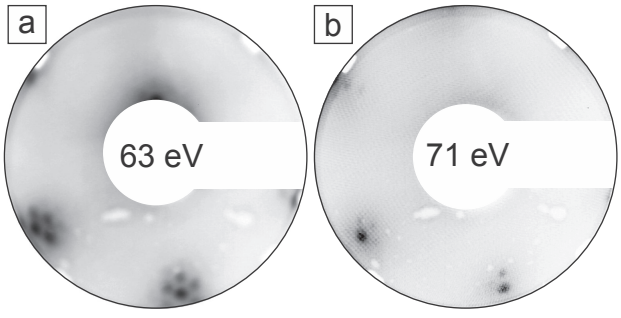

Figure 8.35: LEED images of gr/O/Ir(111). Image taken before (a) and after (b) O intercalation.

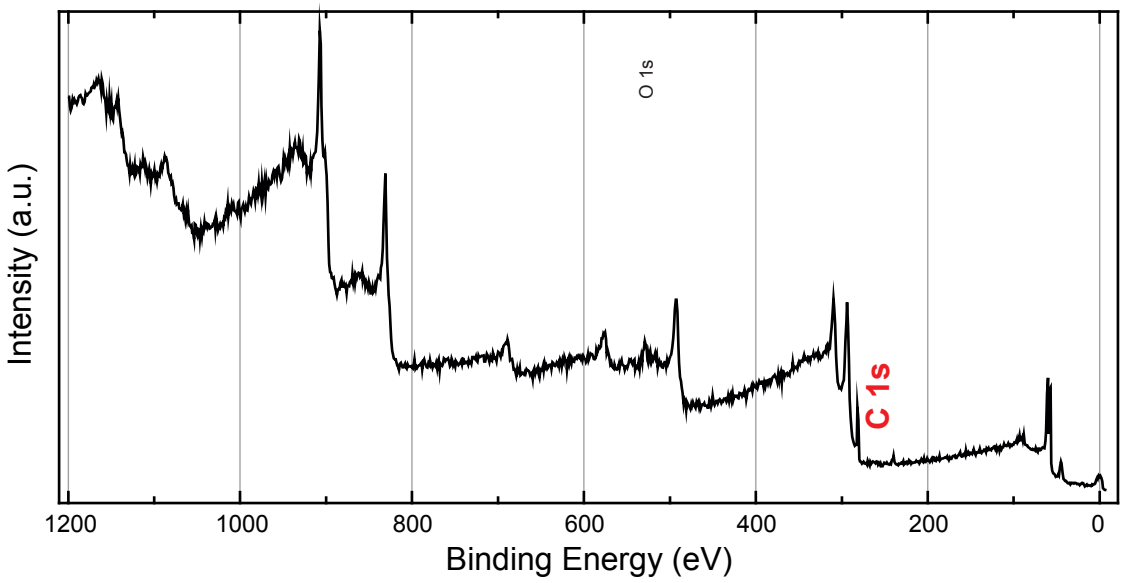

Figure 8.36: XPS survey scan of gr/O/Ir(111). Beside the Ir core level peaks (comp. Fig. 8.2) and the C 1s also the newly emerged O 1s core levels can be seen. Photon energy was 2810 eV.

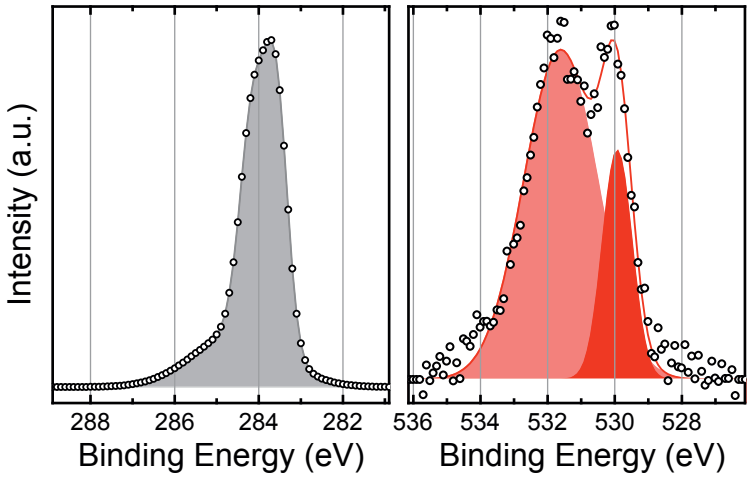

Figure 8.37: XPS measurement of the C 1s and O 1s core levels of gr/O/Ir(111). C 1s core level (grey) and O 1s core level (red). Fits are shown as solid lines, data as circles. Two components were found at the O 1s position. The dark red one is assigned to O/Ir, the light red one remains unclear. Photon energy was 2810 eV.

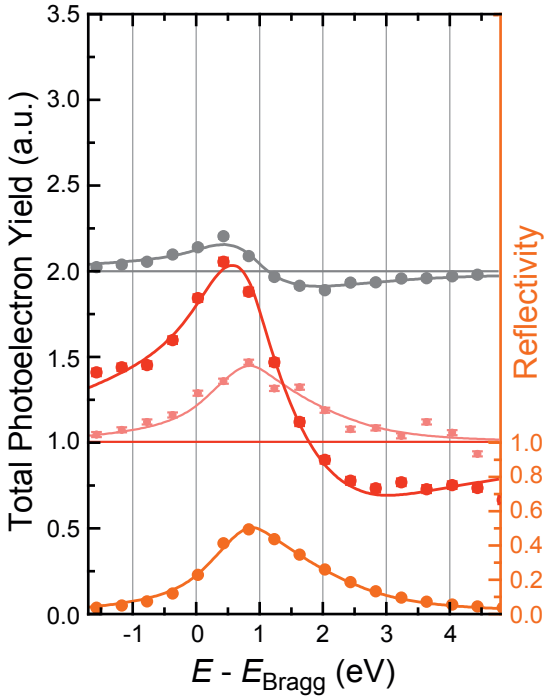

Figure 8.38: XSW results for gr/O/Ir(111). Data is presented as circles, fits as solid lines. Graphene is shown in grey, oxygen in red, and the reflectivity in orange. The light red line corresponds to the unassigned peak at 532 eV [comp. Fig. 8.37(b)]. The XSW curve for gr is shifted by 1 for better illustration. For each core level the corresponding value of 1 is shown by a horizontal line.

for the coherent position and coherent fraction are extracted and translated into heights above the iridium substrate. These results are carried together in Table 8.10.

While the small peak in the O 1s spectrum (Fig. 8.37) has a meaningful value, the coherent fraction for the broad light red peak is extremely low. Therefore a meaningful height can not be assigned to this peak. Hence, it can be concluded that this peak is not related to adsorbed or intercalated oxygen.

A sketch of the results is presented in Figure 8.39. The distance between graphene and oxygen calculates to 2.69 Å. A direct comparison of the height of the oxygen atoms above the substrate can be done with results from adsorbed oxygen on a clean iridium crystal. From literature this distance is known to be 1.30 Å [91]. The measured distance for our sample differs by just 0.05 Å from the value for adsorbed oxygen. Therefore one can conclude that the oxygen atoms are almost unaffected by the overlying graphene, as slight binding between graphene and oxygen would reduce the binding strength to the substrate,

Table 8.10: XSW results of gr/O/Ir(111). Results for the C 1s and O 1s core levels as well as the unassigned peak from Fig. 8.37. Results are averaged from two, two, and one measurements for the C 1s, O 1s, and the unassigned peak.

Species	$P^{(111)}$	$F^{(111)}$	**height**
gr	0.79 ± 0.01	0.41 ± 0.04	(3.96 ± 0.02) Å
O	0.58 ± 0.01	0.58 ± 0.04	(1.27 ± 0.02) Å
unassigned	0.77 ± 0.01	0.06 ± 0.04	*undefined*

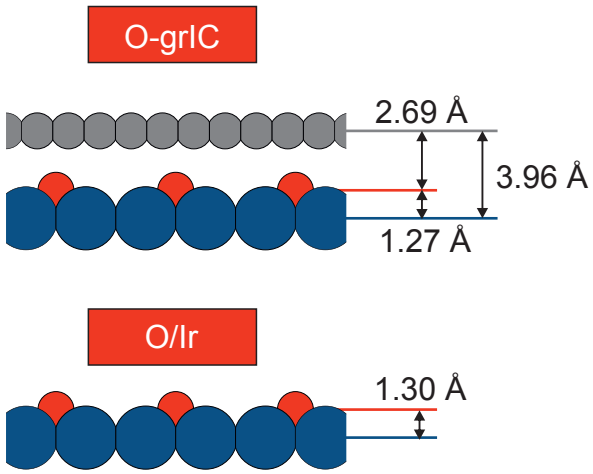

Figure 8.39: Sketch of grIC and O/Ir. Simple sphere model according to the space-filling model. Empirical atom sizes [80] and distances are to scale. Ir substrate atoms are coloured blue, O red, and gr grey.

and, in consequence, leading to an enlarged distance of the oxygen to the substrate. Quite the contrary, the oxygen resides slightly closer to the substrate. As graphene seems not to affect the underlying oxygen, this finding works also vice versa. Conclusively, intercalated oxygen serves as a quasi non-interacting buffer layer, which corroborates the assumption that oxygen intercalated graphene is quasi freestanding [22] by geometrical arguments.

As mentioned before the position of the C 1s core level for the oxygen intercalated graphene sample is shifted by +0.22 eV compared to pristine graphene measured under the same conditions (see Section 9.1 for details). A relation between the core level shift and the density of intercalated oxygen atoms can be found in Reference [22]. The core level shift found for this intercalated sample fits to an oxygen coverage of approximately 0.27 ML.

Results from DFT calculations are presented in Table 8.8, where average heights of the oxygen atoms and graphene at the three high symmetry regions fcc, hcp, and top are determined [92]. To achieve a periodic supercell commensurate superstructures with an oxygen coverage of 1/9 ML and 1/3 ML, and 1/2 ML were simulated. This findings are in

Table 8.11: Comparison of theoretical and experimental results for O-grIC. From a DFT calculation the resulting heights [92] for the O atoms, the gr layer, as well as the distance Δh between O and gr are shown for O coverages of 1/9 ML and 1/3 ML. The experimental results of the(2×2) superstructure are presented for comparison.

DFT calculation					**XSW results**			
coverage	O	Δh	gr		**coverage**	O	Δh	gr
0.11 ML	1.23 Å	2.68 Å	3.90 Å	}	0.27 ML	1.27 Å	2.69 Å	3.96 Å
0.33 ML	1.33 Å	2.87 Å	4.18 Å					
0.50 ML	1.25 Å	2.99 Å	4.24 Å					

very good agreement with the experimental results. However, in contrast to the results for the europium and caesium intercalation compounds the tendency of decreasing distance for increasing intercalant coverage does not hold for the case of oxygen and is not explainable by electrostatic forces.

8.4 Conclusion

In Section 8.1 the coverage dependent morphology of graphene on iridium was investigated. For this, first the influence of contaminations, wrinkles, iridium step edges, and graphene edges was discussed. It could be shown, that influences of contaminations can be ruled out as their impact would decrease for increasing graphene coverage, which is in strong contradiction to the results. A simple model for wrinkles indicates that the amount of incoherent carbon atoms is below 1.2 %, while for the case of substrate step edges the upper limit is 4.4 %. The influence of graphene edges is strongly dependent on the flake size. For our case it leads to 1.1 % of incoherent carbon atoms. The XSW analysis results a constant value for the coherent position, which is in good agreement with DFT calculations for a commensurate moiré unit cell. However, a large discrepancy to the calculations was found for the coherent fraction. While for medium sized islands the coherent fraction reveals the highest value, it is lower for small islands and decreases for higher coverages. By taking the approximations for wrinkles, step edges, and graphene edges into account the peak-to-peak corrugation results to at least 0.73 Å for 0.22 ML, 0.36 Å for 0.39 ML, 0.86 Å for 0.63 ML, and 1.33 Å for 1.00 ML. The different amplitudes of the moiré corrugation are caused by the compressive stress during the cool down of the sample from the preparation temperature. For medium sized islands the flake edges are able to slip over the substrate to release stress efficiently. For small islands, in contrast, the elastic energy of the entire flake is too small to overcome the strong bonding of the edge atoms. In case of the percolated graphene sheet the stress relaxation is inhibited, and impossible for the fully closed layer. Hence, the stress is released by buckling of the graphene layer, which in turns means an increase in the peak-to-peak amplitude of the moiré unit cell.

In Section 8.2 the atomic structure of clusters adsorbed on gr/Ir(111) is investigated. From XSW measurements the distance of the platinum atoms to the iridium substrate atoms results to 4.65 Å, which is in good agreement with the calculated height of 4.70 Å from a simple sphere model for covalent bound atoms. This finding as well as the results from iridium cluster experiments are compared to a simple model of three defined carbon heights: the average value for pristine graphene as well as the high and low atom in the rehybridised case. The tendency of the change in the structure parameters of graphene for an increasing amount of rehybridised carbon atoms is in good agreement with our data. Furthermore, a simulation utilising a combination of the Keating potential and SXRD measurements [72] joins the tendency, indicating the good applicability of this

approximation. Hence, the idea of rehybridisation of the carbon atoms is supported by the performed structure analysis. By this complete structure determination of the clusters from the combination of XSW and XSRD measurements the basis for investigating ongoing catalytic processes is established [29].

For caesium deposition on a fully covered graphene sample the intercalation process was analysed by STM, LEEM, and ARPES. It could be demonstrated that intercalation takes place at defects which form at wrinkle crossings and cracks in wrinkles. Due to the presence of defects in the graphene layer it can be concluded, that the process is not limited to caesium but also enables the intercalation of other atom species.

The possible in-plane structures of the caesium intercalant layer have been investigated by LEED and STM measurements. It turned out that intercalation sets in after formation of an adatom gas. For increasing amount of deposited caesium the intercalants arrange in a $(2 \times 2)_{\mathrm{Ir}}$, a $(2 \times 2)_{\mathrm{gr}}$, and finally in a $\sqrt{3}_{\mathrm{Ir}}$ superstructure. From STM measurement it was shown that the $(2 \times 2)_{\mathrm{gr}}$ superstructure can be manipulated by the STM tip even at 6.5 K leading to additional rotated phases.

The intercalation compounds including europium, caesium, and oxygen intercalants were investigated by XSW measurements revealing the heights of the intercalant atoms as well as of the covering graphene layer. For europium and caesium a comparison with the graphite intercalation compounds shows that the distances between graphene and the intercalants are enlarged, meaning that the interaction of the intercalants to the graphene layer must be weaker than in the respective graphite intercalation compounds. In case of oxygen the height of the intercalated atoms does not differ from the pure adsorbed state on clean iridium. This means that also from structural reasons the graphene layer is quasi freestanding, corroborating the results from ARPES measurements in literature [22].

In case of intercalated europium it is demonstrated experimentally that the distance between the graphene sheet and the intercalants depends on the superstructure. For a high europium coverage in the $\sqrt{3}_{\mathrm{gr}}$ superstructure the graphene layer resides closer to the europium atoms as in case of a $(2 \times 2)_{\mathrm{gr}}$. This tendency is supported by DFT calculations, which show the same behaviour also for caesium intercalants. From the doping of the intercalated graphene sheet determined by ARPES measurements, the electron transfer to graphene was calculated, which reveals that the high coverage sample is stronger doped and in turn more electrons from the europium atoms are transferred to it. Hence, for systems interacting mainly via van-der-Waals force it could be shown that the distance between graphene and intercalants is noticeable depending on the charge transfer. How-

ever, for the oxygen intercalated sample DFT calculations reveal an opposing tendency, where the distance increases for more dense intercalants.

CHAPTER 9

Investigation of the Electronic Structure

Parts of Section 9.1 are also presented in Reference [93].
Parts of Section 9.2 are also presented in Reference [94]. All experiments discussed in the following were carried out by myself with assistance of Marin Petrović. They were planned and interpreted with support of Carsten Busse.

In the previous chapter the graphene intercalation compounds are discussed regarding its structure, which was investigated by STM, LEED, and XSW. For the XSW measuments preceded XPS measurements were presented, revealing different binding energies for the C 1s core levels of different graphene intercalation compounds. This core level shifts are discussed in Section 9.1.
The effect of decoupling the graphene layer by caesium intercalation is shown by STM measurements in Section 9.2 by an analysis of Dirac electron scattering.

9.1 Doping in Graphene Intercalation Compounds

In Figure 9.1 the C 1s core level spectra for the graphene intercalation compounds that were investigated, namely caesium (purple), europium (aquamarine), and oxygen (red) are shown and compared to pristine graphene (grey). While the electron donors (Eu, Cs) lead to a core level shift to higher binding energies, an electron acceptor (O) shifts the core level to lower binding energies. The same effect was found by high-resolution XPS measurements in References [81, 93]. In our cases the peaks have an asymmetric shape and appear broadened according to the low resolution during the XSW experiments.
The peak positions of the C 1s core levels are listed in Table 9.1. The core level shift is given as the difference in the measured C 1s binding energy of pristine graphene to that of the respective intercalation compound. From ARPES measurements the doping of samples with different superstructures or coverages of the intercalants is reported from References [22, 88] and presented for comparison. Note, that the position of the C 1s core level for pristine graphene is slightly displaced with respect to the values around

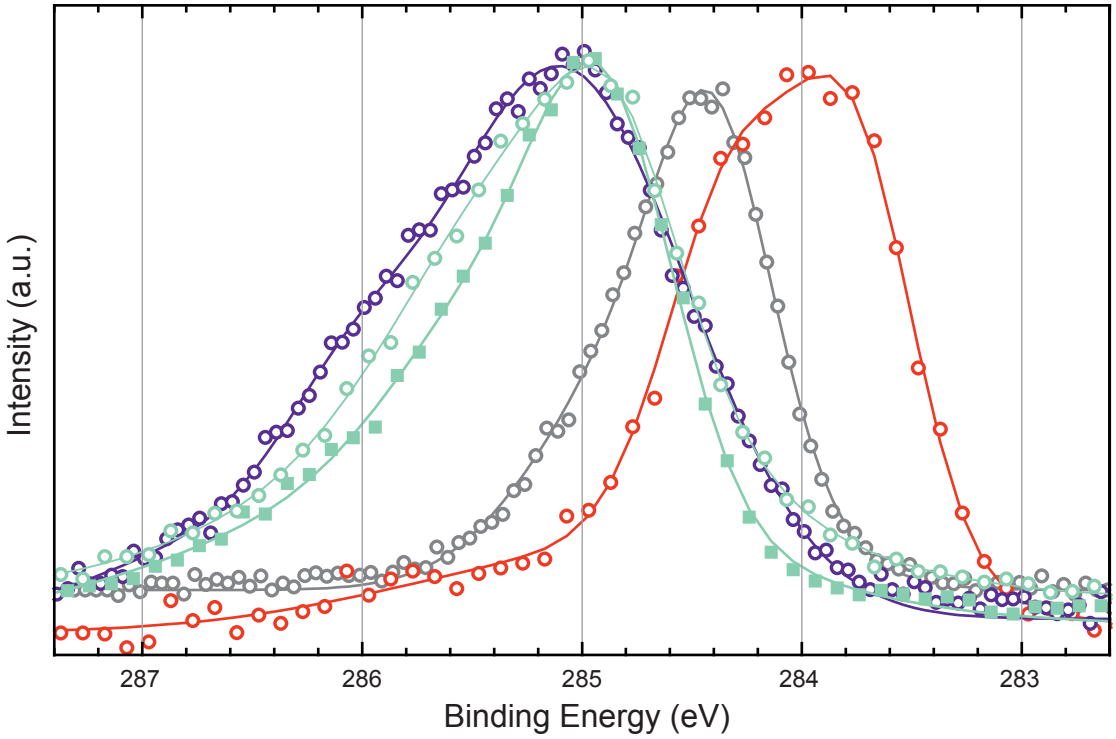

Figure 9.1: C 1s core level shifts for grICs compared to pristine graphene. The C 1s core levels are shown for pristine gr (grey), O-grIC (red), Cs-grIC (purple), and Eu-grIC (aquamarine). Data is shown as circles, fits as solid lines. For Eu-grIC the $(2 \times 2)_{gr}$ structure is presented by open circles and the faint line, the $\sqrt{3}_{gr}$ structure with filled squares and the solid line. Photon energy was 2810 eV.

Table 9.1: C 1s CLSs and doping of grICs. Average positions of the maxima of the C 1s core levels from XPS measurements (see main text). The CLS $\Delta E_\mathrm{B} = E_\mathrm{B} - E_\mathrm{B}^\mathrm{prist}$ was determined as the difference between the respective core level to the one of pristine graphene. Doping values $E_\mathrm{dop} = E_\mathrm{F} - E_\mathrm{D}$ from Refs. [22, 88] presented as relative positions of the Fermi energy with respect to the Dirac point. For the Eu-grIC results both structures are presented. For Cs and O the superstructure is not perfectly clear in our experiments, therefore doping values are given of several intercalation structures for comparison. The * marks that the structure is unknown and the measurement was done at maximum coverage.

Intercalant	E_B (eV)	ΔE_B (eV)	**Structure**	E_dop (eV)
Eu	284.99 ± 0.06	$+0.64$	$(2\times2)_\mathrm{gr}$	$+1.36$ [88]
	284.91 ± 0.07	$+0.56$	$\sqrt{3}_\mathrm{gr}$	$+1.43$ [88]
Cs	285.05 ± 0.05	$+0.70$	$(2\times2)_\mathrm{gr}$	$+1.13$ [88]
			$\sqrt{3}_\mathrm{gr}$	$+1.20$ [88]
O	284.13 ± 0.10	-0.22	$\sqrt{3}_\mathrm{Ir}$	-0.40 [96]
			$0.38\,\mathrm{ML}^*$	-0.64 [22]
			$(2\times1)_\mathrm{Ir}$	-0.68 [93]
pristine gr	284.35 ± 0.08	0	—	-0.07 [22]

284.1 eV reported in literature [21, 22, 81, 93, 95]. Due to the asymmetric broadness and the low resolution caused by the XSW measuring conditions the exact determination of the peak position is much less accurate than in pure XPS measurements. While in these high resolution measurements one gaussian can be used to fit the data, this does not hold for our experiments. Hence, the analysis is done by a determination of the maxima of the core level peaks and their shift with respect to the one of pristine graphene.

A comparison of the doping $E_\mathrm{dop} = E_\mathrm{F} - E_\mathrm{D}$ with the core level shifts ΔE_B reveals, that these values shift in the same direction. This can be explained by a rigid-band model shown in Figure 9.2 for n-, and p-doped as well as for pristine graphene. In this model the Dirac cone and the C 1s core level are fixed with respect to the vacuum level E_vac, i.e. $\Phi^* = E_\mathrm{vac} - E_\mathrm{D} = \mathrm{const}$ [97] and $E_\mathrm{B}^* = E_\mathrm{D} - E_\mathrm{C1s} = \mathrm{const}$. As a consequence the *measured* binding energy E_B can be splitted into a constant part E_B^* and the doping E_dop. A similar expression can be derived for the *measured* work function Φ. Following a charge transfer towards the graphene sheet (doping) the position of the Fermi level is *not* conserved. In consequence, the experimentally accessible values Φ and E_B change as the Fermi energy level is the reference energy of XPS, ARPES, and STS.

Qualitatively the results presented in Table 9.1 are in good agreement with the rigid-band model, while quantitatively a deviation occurs. For the binding energy this model

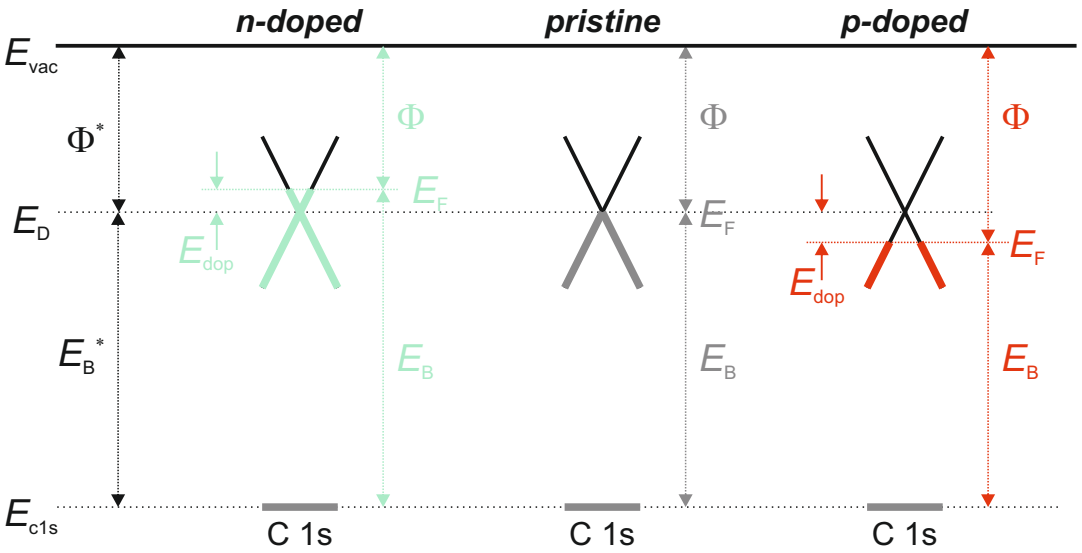

Figure 9.2: Sketch of a rigid band model for doped and undoped gr. The Fermi energy E_F, doping E_{dop}, work function Φ, and the binding energy E_B differ for n-doped (aquamarine), pristine (grey), and p-doped gr (red). For each case occupied states are marked in the respective colours on top of the cut through the Dirac cone (black). The position of the Dirac cone E_D and of the C 1s core level are fixed to the joint vacuum level E_{vac}, leading to a constant distance E_B^* (see text). Note, that the energy scale is non-linear.

is just valid for slight doping. The charge transfer becomes more and more important for increasing doping as the electron transfer to (from) the graphene layer leads to a higher (lower) charge density at the carbon atoms and in turns increasing (decreasing) screening of the nuclei. Thus, the core level shift due to screening becomes more and more important and compensates for the shift originating from this rigid-band model. The reason why the screening effect is insignificant for small doping is caused by the low density of states at the Dirac point, meaning, that a small charge transfer has a high impact on the doping level.

9.2 Dirac Electron Mapping in Intercalated Graphene

As mentioned in Section 8.3.2 the Fourier transform of a topograph from an caesium intercalated area reveals constant energy contours [see Fig. 8.19(d)]. The origin of these contours is discussed in the following.

In Figure 9.3 an atomically resolved STM topograph is shown. At the lower edge of the image a point defect can be seen, while the residual surface is defect free. Zoom-ins into a region apart from the defect as well as close to the defect (indicated by the white boxes) are shown in Figures 9.3(b,d) and the respective Fourier transforms in Figures 9.3(c,e). While the region close to the defect reveals $(2 \times 2)_{\mathrm{gr}}$ superstructure spots, in Figure 9.3(e) additional contours can be seen, resembling the situation presented in Figure 8.19(d). Such kind of structures originate from graphene electron scattering processes at defects, leading to corresponding scattering vectors in the Brillouin zone, which are directly associated with the structures in the Fourier transform [98]. The standing electron waves caused by the scattering at this defect are damped in such a way that they can not be observed 11 nm apart the defect, as this is the distance of the centre of Figure 9.3(b) to the defect.

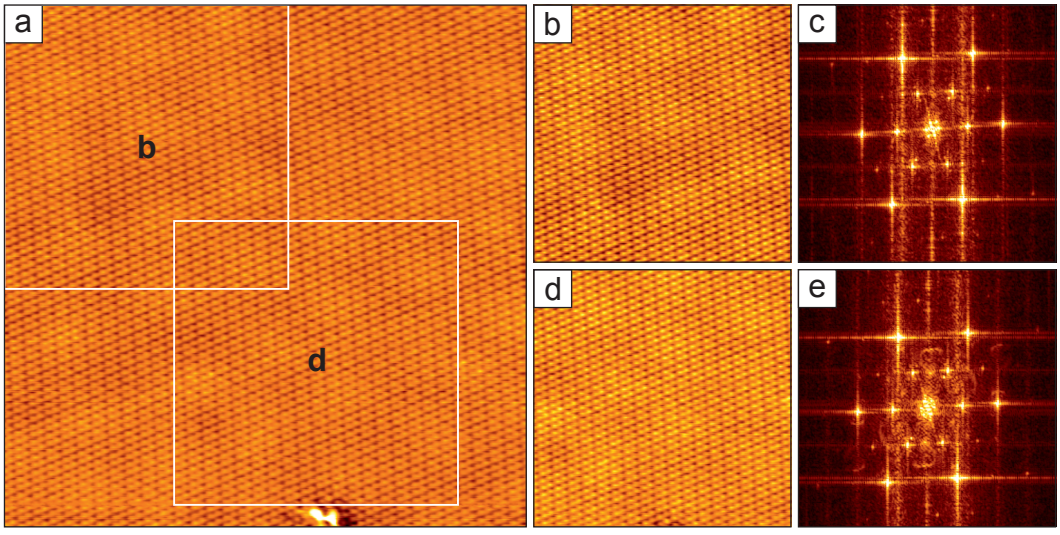

Figure 9.3: STM measurement close to a defect. The overview image (a) contains a defect in the lower end of the image. Two sections are presented in (b,d), which are at the positions of the white squares labelled (b) and (d), respectively. The fourier transform of this images are to the right of the topographs, where (c) corresponds to (b) and (e) to (d), respectively. Image sizes are (a) 13.8 nm, (b,d) 7.5 nm, and (c,e) 1.9 nm^{-1}. Bias voltage was 40 mV.

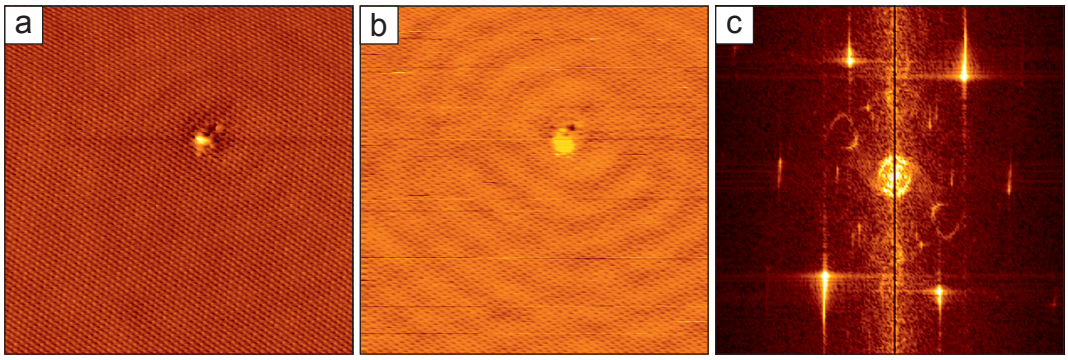

Figure 9.4: Spectroscopy measurement at a defect. Topograph (a) and dI/dU-map (b) at a defect in the graphene layer. Fourier transform (c) of image (b) reveals constant energy contours from Dirac electrons. Image width is (a,b) 146 nm, (c) 14.3 nm^{-1}. Measuring conditions were $U = -0.1\,\mathrm{V}$, $I = 300\,\mathrm{pA}$.

A second spectroscopy measurement at a defect is presented in Figure 9.4. The topograph [Fig. 9.4(a)] shows a point defect on a atomically resolved area. In the spectroscopy image [Fig. 9.4(b)] a circular standing wave pattern surrounding the defect is clearly visible. The Fourier transform of the spectroscopy image is shown in Figure 9.4(c). It shows triangular contours as well as a circle around the centre, which is related to the standing wave pattern in real space. Furthermore, the Fourier transform reveals spots of a $(2 \times 2)_{\mathrm{gr}}$ superstructure.

The high-resolution STM topograph presented in Section 8.3 is shown enlarged in Figure 9.5(a). In this atomically resolved image the entire area reveals a perfectly intact graphene layer without any defects. However, the moiré pattern is obviously disturbed by a grain boundary of the intercalant layer in the middle of the image. The fourier transform of the STM image is shown in Figure 9.5(b). Circular and triangular contours can be seen, which are highlighted by the yellow and white arrows. These contours are depicted enlarged in Figure 9.5(c) and Figure 9.5(d), respectively. In a contrast enhanced image the symmetry of the contours is illustrated by the yellow and white overlays: The triangular contours appear with hexagonal symmetry, while for the circular contour one direction is almost invisible.

The origin of these contours shown in Figures 9.3(e), 9.4(c), and 9.5(b-e) can be related to Dirac electron scattering [99]. The strong doping due to the intercalated caesium causes a shift of the Fermi energy out of the linear regime into that one of trigonal warping [31] of the constant energy contours. As presented in this section point defects as well as line defects (intercalant grain boundaries) cause the appearance of constant energy contours in Fourier transforms. However, this was not observed at substrate step edges.

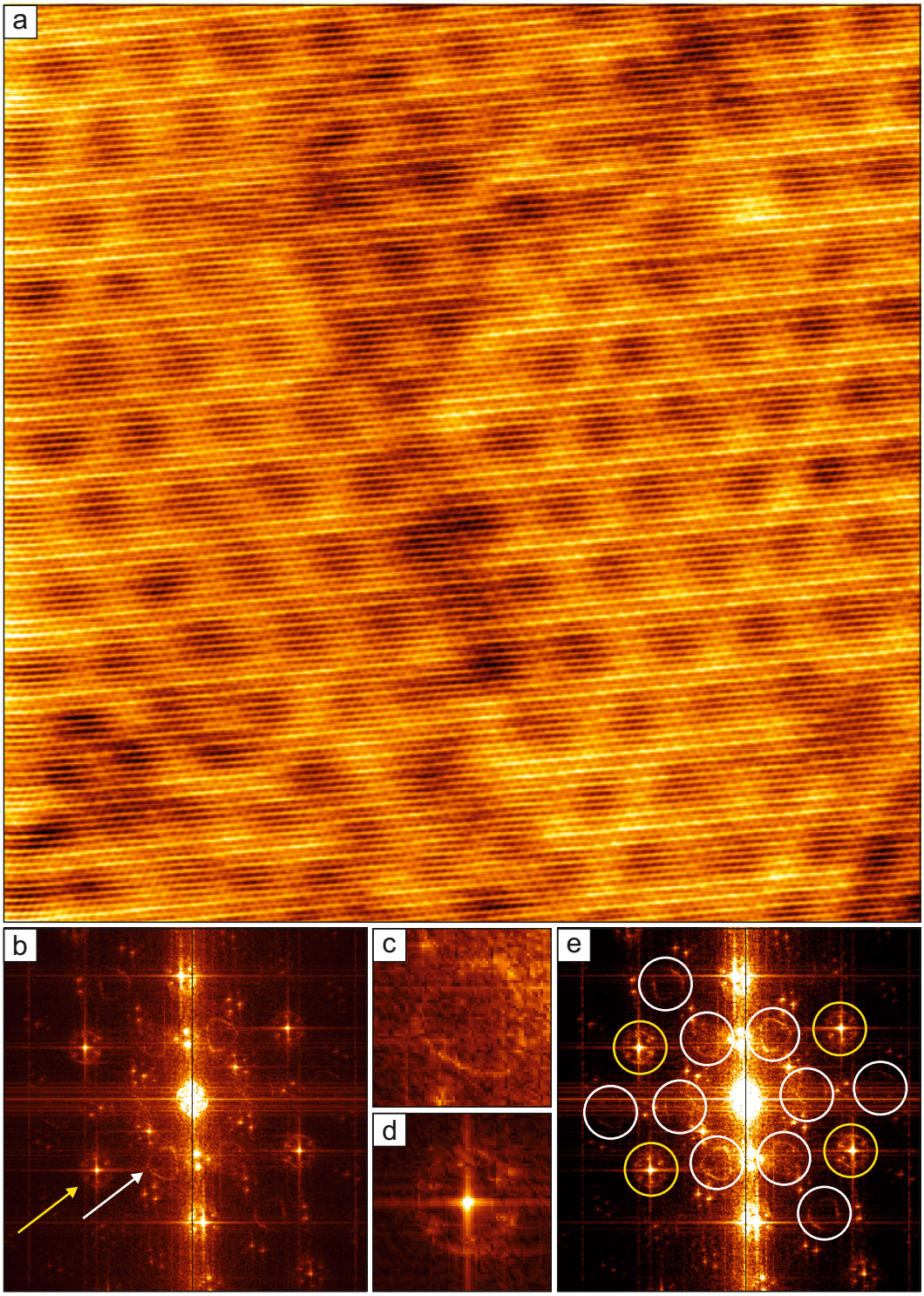

Figure 9.5: Grain boundary on the Cs-grIC. (a) STM Topograph of an intercalated area of the Cs-grIC. Image details are $U = 0.04\,\mathrm{V}$, $I = 300\,\mathrm{pA}$, 18.7 nm (2048 px). Image was taken at the position of the white square of Fig. 8.19(b). (b) Fourier transform of image (image size $21\,\mathrm{nm}^{-1}$). The magnifications shown in (c) and (d) are indicated by the white and yellow arrow, respectively. Image (e) shows the contours of (c,d) with better contrast than in (b), highlighted by white triangles and yellow circles, respectively.

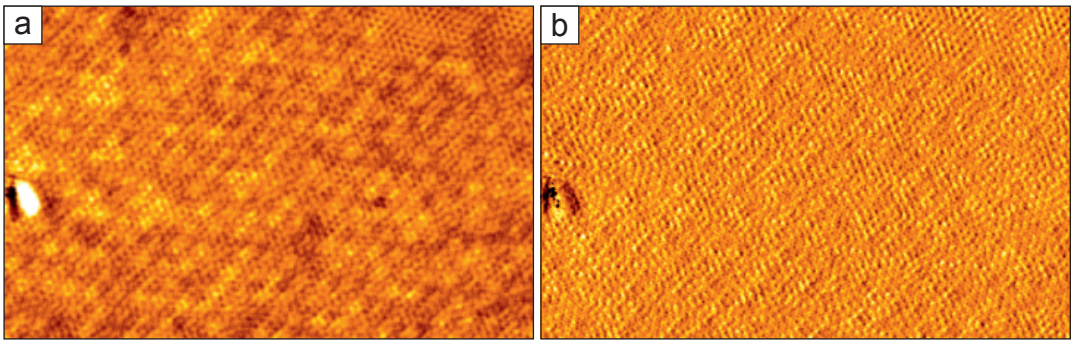

Figure 9.6: Spectroscopy map of gr/Cs/Ir(111). Topograph (a) and spectroscopy map (b) on a $\sqrt{3}_{\mathrm{gr}}$ intercalated area. Image size is (a,b) 27.5 nm × 15.4 nm, Bias voltage 300 mV.

The occurrence of constant energy contours as highlighted in Figures 9.3(e), 9.4(c), and 9.5(b-e) was reported to result from intervalley and intravalley scattering of the Dirac electrons [99]. As the model is done for slightly doped graphene the contours are both circular, while in our case triangular contours are present. This can be explained by the strong doping, meaning that the trigonal warping has set in.

In case of pseudo-spin conservation the contours highlighted by the triangles in Figure 9.5(e) are expected to exhibit a gap, while no gap is predicted for the scattering process without pseudo-spin conservation, which is accompanied with the occurrence of a ring around the centre of the Fourier transform.

While the measurements in Figures 9.5 and 9.3 reveal gap-less contours with a high intensity in the centre, in Figure 9.4 shows additionally a pronounced ring around the centre. Hence, there is a high possibility that our measurements reveal both intervalley and intravelley scattering without conservation of pseudo-spin. However, concerning the observation of intravalley scattering, scattering processes between the carbon layer and the underlying atoms have to be ruled out.

A spectroscopy measurement on a caesium intercalated sample with $\sqrt{3}_{\mathrm{gr}}$ superstructure is shown in Figure 9.6. The topography image [Fig. 9.7(a)] of this area reveals a highly disordered structure, which is also visible in the spectroscopy map [Fig. 9.7(b)]. On this

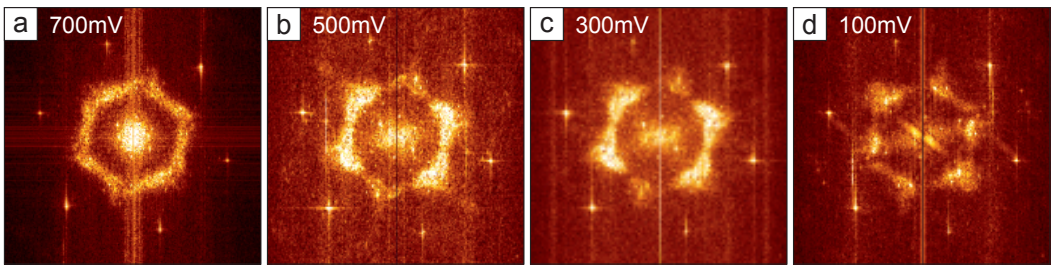

area a series of spectroscopy maps was performed, which resulting Fourier transforms are presented in Figure 9.7.

The appearance of elongated structures gives rise to the assumption the we entered already the region of the van-Hove singularity. While the approximation by a Dirac cone becomes difficult for the case of trigonal warping already, for this case the model collapses. To get a full understanding of the features in the Fourier transform series theoretical support is needed.

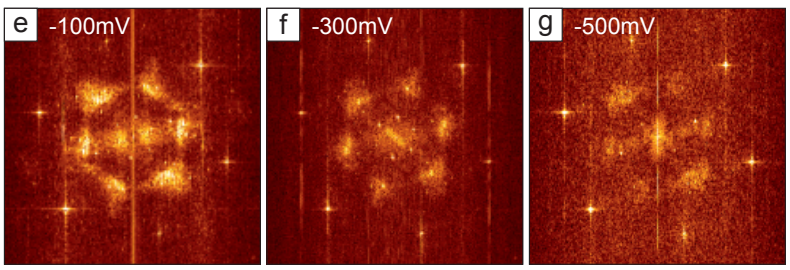

Figure 9.7: Spectroscopy Fourier transform series of gr/Cs/Ir(111). Series taken at position shown in Fig. 9.6. Images processed by equalising and flattening by line. Image sizes are 12.4 nm^{-1}.

9.3 Conclusion

In Section 9.1 the shifts of the C 1s core level is discussed. While for n-doped graphene due to europium or caesium intercalation a shift to higher binding energies occurs, a shift to the opposite direction is found for the p-doped oxygen intercalated sample. This was also shown by high resolution XPS measurements presented in References [81, 93]. As also the work function is dependend on the doping [97] a rigid-band model is presented, that combines both effects. The Dirac point and the core levels are at a fixed positions with respect to the joint vacuum energy. As for experimental results the Fermi energy is used as a reference the work function as well as the binding energy are shifted by the doping energy. While the work function follows strict this model for the binding energy it is more complicated in case of strong doping. In this case the commonly known core level shift due to screening of the nuclei gains increasing influence and partial compensates the influence of doping. The strong influence of the doping on the work function and the core level shifts is caused by the low density of states.
Spectroscopy measurements on the caesium intercalated graphene reveal constant energy contours in the Fourier transform caused by electron scattering. It could be shown that these contours vanish within 11 nm from the point defect. A standing wave pattern at a point defect can even be seen in real space in a spectroscopy map. Moreover, the contours appear at a structural intact graphene layer, that covers domain boundaries of intercalants residing on different adsorption sites. The origin of the contours could be related to intervalley and intravalley scattering of Dirac electrons. Due to the absence of a gap in the contours the scattering process reveals a non-conserved pseudo-spin. While the constant energy contours reveal trigonal warping further spectroscopy measurements were performed close to the van-Hove singularity.

PART V

Summary and Outlook

Summary

The morphology of graphene was investigated regarding the coverage. It was shown, that graphene on iridium(111) has a substantially larger corrugation than predicted by DFT calculations. Moreover, the amplitude of the corrugation depends on the strain state of the graphene sheet, which varies for different topographies. An increase of the height modulation from the moiré pattern accommodates the external stress acting on the graphene layer.

The distance between platinum clusters and the substrate proves the rehybridisation of carbon atoms in graphene by geometrical arguments. It was shown that the structural parameters for a variable amount of cluster atoms can be described by a simple model.

Cracks and holes at wrinkles and wrinkle crossings in the graphene layer enable the intercalation process. The phase diagram of superstructures formed in a caesium intercalation compound could be resolved. The superstructure of the underlying caesium atoms can be influenced by an STM tip even at low temperatures. The analysis of the heights in intercalation compounds reveal a weaker interaction of the graphene layer with the intercalants than in graphite intercalation compounds. The distance between graphene and the intercalants is dependent on the charge transfer for systems interacting mainly via van der Waals forces. In case of oxygen intercalation the graphene layer was found to be quasi freestanding by geometrical arguments.

A rigid-band model was expressed combining the effect of doping dependent work functions and core level shifts. In case of graphene this effect is rather strong due to the low density of states. The deviation from this model in case of strong doping and in turns a high charge transfer is caused by in increasing impact of screening.

Tunnelling spectroscopy measurements on caesium intercalated graphene reveal trigonal warped constant energy contours in Fourier transforms. These signatures are related to intervalley and intravalley scattering processes at defects. Moreover, it is shown that electron scattering is caused by both point defects and grain boundaries in the intercalant layer. Furthermore, due to the strong doping even the region of van-Hove singularities was measured by spectroscopy.

Outlook

As it was shown that the moiré amplitude is dependent on the morphology due to different stress states this might influence the minigaps in the π-bands and could lead to a

possibility to relate the size of the gaps to a certain stress state. An detailed comparison of the energetic costs for buckling and bond compression would allow for quantitative analysis of the buckling and may lead to understand pattern formation in more complex situations due to the knowledge of the influence of stress.
Further XSW measurements at caesium intercalated graphene should be done in order to confirm the argument that the electrostatic force leads to a reduced distance between the graphene layer and an increasing amount of intercalated atoms. Of course, other intercalants that interact via van der Waals forces can be measured for different structures as well in order to support this arguments. In case of oxygen intercalated graphene a series of increasing intercalant coverage would reveal the dependence of the graphene-oxygen distance on the intercalant coverage.
The presented spectroscopy data might also carry information on the Dirac electron dispersion relation. Yet, further analysis as well as theoretical support is need

PART VI

Bibliography

[1] F. Schwierz: "Graphene transistors." *Nature Nanotechnology* **5.7** (2010), 487. DOI: 10.1038/nnano.2010.89. (Cit. on p. 3).

[2] M. I. Katsnelson, K. S. Novoselov, and A. K. Geim: "Chiral tunnelling and the Klein paradox in graphene". *Nature Physics* **2.9** (2006), 620–625. DOI: 10.1038/nphys384. (Cit. on p. 3).

[3] Y. Zhang, Y.-W. Tan, H. L. Stormer, and P. Kim: "Experimental observation of the quantum Hall effect and Berry's phase in graphene." *Nature* **438.7065** (2005), 201. DOI: 10.1038/nature04235. (Cit. on p. 3).

[4] C. Berger, Z. Song, T Li, and X. Li: "Ultrathin epitaxial graphite: 2D electron gas properties and a route toward graphene-based nanoelectronics". *Journal of Physical Chemistry B* **108.52** (2004), 19912–19916. (Cit. on p. 3).

[5] A. K. Geim: "Graphene: status and prospects." *Science* **324.5934** (2009), 1530–4. DOI: 10.1126/science.1158877. (Cit. on p. 3).

[6] M. Dragoman, D. Dragoman, G. Deligiorgis, G. Konstantinidis, D. Neculoiu, a. Cismaru, and R. Plana: "Current oscillations in a wide graphene sheet". *Journal of Applied Physics* **106.4** (2009), 044312. DOI: 10.1063/1.3208061. (Cit. on p. 3).

[7] Y. Lin, C Dimitrakopoulos, and K. Jenkins: "100-GHz transistors from wafer-scale epitaxial graphene". *Science* **327** (2010), 662. (Cit. on p. 3).

[8] F. Schedin, A. K. Geim, S. V. Morozov, and E. W. Hill: "Detection of individual gas molecules adsorbed on graphene". *Nature Materials* **6.9** (2007), 652. DOI: 10.1038/nmat1967. (Cit. on p. 3).

[9] Q. Zhou and A. Zettl: "Electrostatic graphene loudspeaker". *Applied Physics Letters* **102.22** (2013), 223109. DOI: 10.1063/1.4806974. (Cit. on p. 3).

[10] K. S. Novoselov, A. K. Geim, S. V. Morozov, D. Jiang, Y. Zhang, S. V. Dubonos, I. V. Grigorieva, and A. A. Firsov: "Electric field effect in atomically thin carbon films." *Science* **306** (2004), 666. DOI: 10.1126/science.1102896. (Cit. on p. 3).

[11] C. Busse, P. Lazić, R. Djemour, J. Coraux, T. Gerber, N. Atodiresei, V. Caciuc, R. Brako, A. T. N'Diaye, S. Blügel, J. Zegenhagen, and T. Michely: "Graphene on Ir(111): Physisorption with Chemical Modulation". *Physical Review Letters* **107.3** (2011), 036101. DOI: 10.1103/PhysRevLett.107.036101. (Cit. on pp. 3, 10, 11, 58, 62–66).

[12] C. Riedl, C. Coletti, T. Iwasaki, A. A. Zakharov, and U. Starke: "Quasi-Free-Standing Epitaxial Graphene on SiC Obtained by Hydrogen Intercalation". *Physical Review Letters* **103.24** (2009), 246804. DOI: 10.1103/PhysRevLett.103.246804. (Cit. on pp. 3, 13).

[13] Y. Li, G. Zhou, J. Li, J. Wu, B.-L. Gu, and W. Duan: "Lithium Intercalation Induced Decoupling of Epitaxial Graphene on SiC(0001): Electronic Property and Dynamic Process". *The Journal of Physical Chemistry C* **115.48** (2011), 23992–23997. DOI: 10.1021/jp208747q. (Cit. on pp. 3, 13).

[14] C. Virojanadara, S. Watcharinyanon, a. a. Zakharov, and L. I. Johansson: "Epitaxial graphene on 6H-SiC and Li intercalation". *Physical Review B* **82.20** (2010), 205402. DOI: 10.1103/PhysRevB.82.205402. (Cit. on pp. 3, 13).

[15] A. L. Walter, K.-J. Jeon, A. Bostwick, F. Speck, M. Ostler, T. Seyller, L. Moreschini, Y. S. Kim, Y. J. Chang, K. Horn, and E. Rotenberg: "Highly p-doped epitaxial graphene obtained by fluorine intercalation". *Applied Physics Letters* **98.18** (2011), 184102. DOI: 10.1063/1.3586256. (Cit. on pp. 3, 13).

[16] S. Wong, H. Huang, Y. Wang, L. Cao, and D. Qi: "Quasi-free-standing epitaxial graphene on SiC (0001) by fluorine intercalation from a molecular source". *ACS nano* **5.9** (2011), 7662. DOI: 10.1021/nn202910t. (Cit. on pp. 3, 13).

[17] I. Gierz, T. Suzuki, R. T. Weitz, D. S. Lee, B. Krauss, C. Riedl, U. Starke, H. Höchst, J. H. Smet, C. R. Ast, and K. Kern: "Electronic decoupling of an epitaxial graphene monolayer by gold intercalation". *Physical Review B* **81.23** (2010), 235408. DOI: 10.1103/PhysRevB.81.235408. (Cit. on pp. 3, 13).

[18] A. Shikin, G. Prudnikova, V. Adamchuk, F. Moresco, and K.-H. Rieder: "Surface intercalation of gold underneath a graphite monolayer on Ni(111) studied by angle-resolved photoemission and high-resolution electron-energy-loss spectroscopy". *Physical Review B* **62.19** (2000), 13202–13208. DOI: 10.1103/PhysRevB.62.13202. (Cit. on pp. 3, 13).

[19] A. Varykhalov, J. Sánchez-Barriga, A. Shikin, C. Biswas, E. Vescovo, A. Rybkin, D. Marchenko, and O. Rader: "Electronic and Magnetic Properties of Quasifree-standing Graphene on Ni". *Physical Review Letters* **101.15** (2008), 157601. DOI: 10.1103/PhysRevLett.101.157601. (Cit. on pp. 3, 13).

[20] A. Varykhalov, M. R. Scholz, T. K. Kim, and O. Rader: "Effect of noble-metal contacts on doping and band gap of graphene". *Physical Review B* **82.12** (2010), 121101. DOI: 10.1103/PhysRevB.82.121101. (Cit. on pp. 3, 13).

[21] E. Grå näs, J. Knudsen, U. a. Schröder, T. Gerber, C. Busse, M. a. Arman, K. Schulte, J. N. Andersen, and T. Michely: "Oxygen Intercalation under Graphene on Ir(111): Energetics, Kinetics, and the Role of Graphene Edges". *ACS nano* **6.11** (2012), 9951. DOI: 10.1021/nn303548z. (Cit. on pp. 3, 13, 48, 92, 103).

[22] R. Larciprete, S. r. Ulstrup, P. Lacovig, M. Dalmiglio, M. Bianchi, F. Mazzola, L. Hornekæ r, F. Orlando, A. Baraldi, P. Hofmann, and S. Lizzit: "Oxygen switching of the epitaxial graphene-metal interaction." *ACS nano* **6.11** (2012), 9551–8. DOI: 10.1021/nn302729j. (Cit. on pp. 3, 13, 95, 98, 102, 103).

[23] K. V. Emtsev, A. A. Zakharov, C. Coletti, S. Forti, and U. Starke: "Ambipolar doping in quasifree epitaxial graphene on SiC(0001) controlled by Ge intercalation". *Physical Review B* **84.12** (2011), 125423. DOI: 10.1103/PhysRevB.84.125423. (Cit. on pp. 3, 13).

[24] L. Meng, R. Wu, H. Zhou, G. Li, Y. Zhang, L. Li, Y. Wang, and H.-J. Gao: "Silicon intercalation at the interface of graphene and Ir(111)". *Applied Physics Letters* **100.8** (2012), 083101. DOI: 10.1063/1.3687688. (Cit. on pp. 3, 13).

[25] C. Herbig, M. Kaiser, N. Bendiab, S. Schumacher, D. F. Förster, J. Coraux, K. Meerholz, T. Michely, and C. Busse: "Mechanical exfoliation of epitaxial graphene on Ir(111) enabled by Br2 intercalation". *Journal of Physics: Condensed Matter* **24.31** (2012), 314208. DOI: 10.1088/0953-8984/24/31/314208. (Cit. on p. 4).

[26] S. Lizzit, R. Larciprete, P. Lacovig, M. Dalmiglio, F. Orlando, A. Baraldi, L. Gammelgaard, L. Barreto, M. Bianchi, E. Perkins, and P. Hofmann: "Transfer-free electrical insulation of epitaxial graphene from its metal substrate." *Nano Letters* **12.9** (2012), 4503. DOI: 10.1021/nl301614j. (Cit. on p. 4).

[27] R. van Gastel, A. T. N'Diaye, D. Wall, J. Coraux, C. Busse, N. M. Buckanie, F.-J. Meyer zu Heringdorf, M. Horn von Hoegen, T. Michely, and B. Poelsema: "Selecting a single orientation for millimeter sized graphene sheets". *Applied Physics Letters* **95.12** (2009), 121901. DOI: 10.1063/1.3225554. (Cit. on pp. 4, 8, 64).

[28] A. T. N'Diaye, T. Gerber, C. Busse, J. Mysliveček, J. Coraux, and T. Michely: "A versatile fabrication method for cluster superlattices". *New Journal of Physics* **11.10** (2009), 103045. DOI: 10.1088/1367-2630/11/10/103045. (Cit. on pp. 4, 11, 12, 65, 67).

[29] S. Billinge: "Nanoparticle structures served up on a tray". *Nature* **495** (2013), 453. (Cit. on pp. 4, 98).

[30] A. K. Geim and K. S. Novoselov: "The rise of graphene." *Nature materials* **6.3** (2007), 183–91. DOI: 10.1038/nmat1849. (Cit. on pp. 7, 8).

[31] A. H. Castro Neto, N. M. R. Peres, K. S. Novoselov, and A. K. Geim: "The electronic properties of graphene". *Reviews of Modern Physics* **81.1** (2009), 109–162. DOI: 10.1103/RevModPhys.81.109. (Cit. on pp. 7, 9, 106).

[32] M. Katsnelson: "Graphene: carbon in two dimensions". *Materials Today* **10.1** (2007), 20–27. DOI: 10.1016/S1369-7021(06)71788-6. (Cit. on p. 7).

[33] "IUPAC. Compendium of Chemical Terminology, 2nd ed. (the "Gold Book"). Compiled by A. D. McNaught and A. Wilkinson. Blackwell Scientific Publications, Oxford (1997). XML on-line corrected version: http://goldbook.iupac.org (2006-) created by M. Nic, J. Jir" (2012). DOI: doi:10.1351/goldbook. (Cit. on p. 7).

[34] P. Wallace: "The band theory of graphite". *Physical Review* **71.9** (1947), 622–634. DOI: 10.1103/PhysRev.71.622. (Cit. on p. 7).

[35] I. Pletikosić, M. Kralj, P. Pervan, R. Brako, J. Coraux, A. N'Diaye, C. Busse, and T. Michely: "Dirac Cones and Minigaps for Graphene on Ir(111)". *Physical Review Letters* **102.5** (2009), 1–4. DOI: 10.1103/PhysRevLett.102.056808. (Cit. on pp. 8, 74).

[36] E. Starodub, A. Bostwick, L. Moreschini, S. Nie, F. E. Gabaly, K. F. McCarty, and E. Rotenberg: "In-plane orientation effects on the electronic structure, stability, and Raman scattering of monolayer graphene on Ir(111)". *Physical Review B* **83.12** (2011), 125428. DOI: 10.1103/PhysRevB.83.125428. (Cit. on p. 8).

[37] J. Coraux, A. T. N'Diaye, M. Engler, C. Busse, D. Wall, N. Buckanie, F.-J. Meyer zu Heringdorf, R. van Gastel, B. Poelsema, and T. Michely: "Growth of graphene on Ir(111)". *New Journal of Physics* **11.2** (2009), 023006. DOI: 10.1088/1367-2630/11/2/023006. (Cit. on pp. 8, 9, 62, 64).

[38] A. T. N'Diaye, J. Coraux, T. N. Plasa, C. Busse, and T. Michely: "Structure of epitaxial graphene on Ir(111)". *New Journal of Physics* **10.4** (2008), 043033. DOI: 10.1088/1367-2630/10/4/043033. (Cit. on pp. 9, 10, 64).

[39] J. Coraux, A. T. N'Diaye, C. Busse, and T. Michely: "Structural coherency of graphene on Ir(111)." *Nano Letters* **8.2** (2008), 565–70. DOI: 10.1021/nl0728874. (Cit. on pp. 9, 61, 64).

[40] M. Kralj, I. Pletikosić, M. Petrović, P. Pervan, M. Milun, A. NâĂŹDiaye, C. Busse, T. Michely, J. Fujii, and I. Vobornik: "Graphene on Ir(111) characterized by angle-resolved photoemission". *Physical Review B* **84.7** (2011), 075427. DOI: 10.1103/PhysRevB.84.075427. (Cit. on pp. 11, 74).

[41] A. N'Diaye, S. Bleikamp, P. Feibelman, and T. Michely: "Two-Dimensional Ir Cluster Lattice on a Graphene Moiré on Ir(111)". *Physical Review Letters* **97.21** (2006), 215501. DOI: 10.1103/PhysRevLett.97.215501. (Cit. on p. 11).

[42] A. T. N'Diaye: "Epitaxial Graphene and Cluster Lattices on Iridium(111)". PhD-Thesis. RWTH Aachen University, 2010 (cit. on pp. 11, 67).

[43] P. Feibelman: "Pinning of graphene to Ir(111) by flat Ir dots". *Physical Review B* **77.16** (2008), 165419. DOI: 10.1103/PhysRevB.77.165419. (Cit. on p. 12).

[44] P. Feibelman: "Onset of three-dimensional Ir islands on a graphene/Ir(111) template". *Physical Review B* **80.8** (2009), 085412. DOI: 10.1103/PhysRevB.80.085412. (Cit. on p. 12).

[45] J. Knudsen, P. Feibelman, T. Gerber, E. Grå näs, K. Schulte, P. Stratmann, J. Andersen, and T. Michely: "Clusters binding to the graphene moiré on Ir(111): X-ray photoemission compared to density functional calculations". *Physical Review B* **85.3** (2012), 035407. DOI: 10.1103/PhysRevB.85.035407. (Cit. on pp. 12, 70, 72).

[46] S. Rusponi, M. Papagno, P. Moras, S. Vlaic, M. Etzkorn, P. Sheverdyaeva, D. Pacilé, H. Brune, and C. Carbone: "Highly Anisotropic Dirac Cones in Epitaxial Graphene Modulated by an Island Superlattice". *Physical Review Letters* **105.24** (2010), 246803. DOI: 10.1103/PhysRevLett.105.246803. (Cit. on p. 12).

[47] M. S. Dresselhaus and G. Dresselhaus: "Intercalation compounds of graphite". *Advances in Physics* **51.1** (2002), 1–186. DOI: 10.1080/00018730110113644. (Cit. on p. 12).

[48] D. F. Förster: "EuO and Eu on metal crystals and graphene: interface effects and epitaxial films". PhD-Thesis. University of Cologne, 2011 (cit. on pp. 13, 76, 78).

[49] M. Petrović, S. Runte, C. Busse, J. T. Sadowski, P Lazić, I Pletikosić, Z Pan, M Milun, P Pervan, and N Atodiresei: "The Mechanism of Caesium Intercalation of Graphene". *Nature Communications (accepted)* (2013). DOI: 10.1038/ncomms3772. arXiv: 1311.3811. (Cit. on pp. 13, 55, 61, 73, 74, 90, 161).

[50] Stefan Hüfner: *Photoelectron Spectroscopy: Principles and Applications*. Springer, 2003 (cit. on pp. 15, 80).

[51] D. P. Woodruff: "Surface structure determination using x-ray standing waves". *Reports on Progress in Physics* **68.4** (2005), 743–798. DOI: 10.1088/0034-4885/68/4/R01. (Cit. on p. 16).

[52] J. Zegenhagen: "Surface structure determination with X-ray standing waves". *Surface Science Reports* **18.7-8** (1993), 202–271. DOI: 10.1016/0167-5729(93)90025-K. (Cit. on pp. 16, 63).

[53] J. Zegenhagen: "X-ray standing waves imaging". *Surface Science* **554.2-3** (2004), 77–79. DOI: 10.1016/j.susc.2003.12.057. (Cit. on p. 16).

[54] J. Zegenhagen, B. Detlefs, T.-L. Lee, S. Thiess, H. Isern, L. Petit, L. André, J. Roy, Y. Mi, and I. Joumard: "X-ray standing waves and hard X-ray photoelectron spectroscopy at the insertion device beamline ID32". *Journal of Electron Spectroscopy and Related Phenomena* **178-179** (2010), 258–267. DOI: 10.1016/j.elspec.2009.09.008. (Cit. on p. 16).

[55] G. Binnig, H. Rohrer, C. Gerber, and E. Weibel: "Tunneling through a controllable vacuum gap". *Applied Physics Letters* **40.2** (1982), 178. DOI: 10.1063/1.92999. (Cit. on p. 17).

[56] K. Urban, C. M. Schneider, T. Brückel, and S. Blügel: *Probing the Nanoworld*. Forschungszentrum Jülich, 2007 (cit. on p. 17).

[57] R. Wiesendanger: *Scnanning Probe Microscopy and Spectroscopy*. Cambridge University Press, 1994 (cit. on p. 17).

[58] K. Oura, V. G. Lifshits, A. A. Saranin, and M. Katayama: *Surface Science*. Springer, 2003 (cit. on pp. 17, 133).

[59] J. Bardeen: "Tunnelling from a many-particle point of view". *Physical Review Letters* **6.2** (1961), 57–59. (Cit. on p. 17).

[60] J. Tersoff and D. R. Hamann: "Theory of the scanning tunneling microscope". *Physical Review B* **31.2** (1985), 805. DOI: 10.1103/PhysRevB.31.805. (Cit. on p. 17).

[61] J. Tersoff and D. R Hamann: "Theory and application for the scanning tunneling microscope". *Physical Review Letters* **50.25** (1983), 1998–2001. DOI: 10.1103/PhysRevLett.50.1998. (Cit. on p. 17).

[62] D. Subramaniam, F. Libisch, Y. Li, C. Pauly, V. Geringer, R. Reiter, T. Mashoff, M. Liebmann, J. Burgdörfer, C. Busse, T. Michely, R. Mazzarello, M. Pratzer, and M. Morgenstern: "Wave-Function Mapping of Graphene Quantum Dots with Soft Confinement". *Physical Review Letters* **108**.**4** (2012), 046801. DOI: 10.1103/PhysRevLett.108.046801. (Cit. on p. 18).

[63] *Website: Pneumatic vibration Isolators with Automatic Re-Leveling - Specifications* (cit. on pp. 21, 29).

[64] J. Klinkhammer: "Electronic Structure and Magnetism of Thin Films of the Ferromagnetic Semiconductor EuO on the Nanometer Scale". PhD-Thesis. University of Cologne, 2013 (cit. on pp. 23, 25, 26, 28, 32, 45).

[65] *Website: ESRF ID32 - Source characteristics*. 2008 (cit. on p. 37).

[66] A. J. Martínez-Galera: *Private Communication* (cit. on p. 47).

[67] T. Gerber: *Private Communication* (cit. on p. 49).

[68] C. D. Wagner, W. M. Riggs, L. E. Davis, J. F. Moulder, and G. E. Muilenberg: *Handbook of X-Ray Photoelectron Spectroscopy*. Eden Prairie, Minnesota 55344, 1979 (cit. on p. 51).

[69] J. A. Bearden and A. F. Burr: "Reevaluation of X-Ray Atomic Energy Levels". **39**.**1** (1967), 125. DOI: 10.1103/RevModPhys.39.125. (Cit. on p. 51).

[70] I. Horcas, R. Fernández, J. M. Gómez-Rodríguez, J. Colchero, J. Gómez-Herrero, and A. M. Baro: "WSxM: a Software for Scanning Probe Microscopy and a Tool for Nanotechnology." *The Review of Scientific Instruments* **78**.**1** (2007), 013705. DOI: 10.1063/1.2432410. (Cit. on p. 52).

[71] S. Runte, C. Vo-Van, J. Coraux, J. Zegenhagen, T. Michely, and C. Busse: "Graphene buckles under strain". *in preparation* **1**.**111** (2013), 1–7. (Cit. on pp. 55, 161).

[72] D. Franz, S. Runte, C. Busse, S. Schumacher, T. Gerber, T. Michely, M. Mantilla, V. Kilic, J. Zegenhagen, and a. Stierle: "Atomic Structure and Crystalline Order of Graphene-Supported Ir Nanoparticle Lattices". *Physical Review Letters* **110**.**6** (2013), 065503. DOI: 10.1103/PhysRevLett.110.065503. (Cit. on pp. 55, 71, 72, 97, 161).

[73] D. Franz, N Blanc, S. Runte, J. Coraux, U Hejral, T. Gerber, C. Busse, T. Michely, and A. Stierle: "Structure of Graphene/Ir(111) Supported Pt Clusters During CO/O2 Exposure". *in preparation* (). (Cit. on pp. 55, 70, 161).

[74] S. Runte, C. Vo-Van, J. Coraux, J. Zegenhagen, T. Michely, and C. Busse: "XSW Study of Graphene Intercalation Compounds". *in preparation* (2013), 3–5. (Cit. on pp. 55, 161).

[75] R. Djemour: "Structure of Graphene on Ir(111)". Diploma thesis. University of Cologne, 2009 (cit. on pp. 56, 57, 64).

[76] A. T. N'Diaye, R. V. Gastel, A. J. Martínez-Galera, J. Coraux, H. Hattab, D. Wall, F.-J. M. Z. Heringdorf, M. H.-v. Hoegen, J. M. Gómez-Rodríguez, B. Poelsema, C. Busse, and T. Michely: "In situ observation of stress relaxation in epitaxial graphene". *New Journal of Physics* **11.11** (2009), 113056. DOI: 10.1088/1367-2630/11/11/113056. (Cit. on pp. 60, 61).

[77] P. Lacovig, M. Pozzo, D. Alfè, P. Vilmercati, A. Baraldi, and S. Lizzit: "Growth of Dome-Shaped Carbon Nanoislands on Ir(111): The Intermediate between Carbidic Clusters and Quasi-Free-Standing Graphene". *Physical Review Letters* **103.16** (2009), 14–17. DOI: 10.1103/PhysRevLett.103.166101. (Cit. on pp. 61, 62).

[78] Y. Li, D. Subramaniam, N. Atodiresei, P. Lazić, V. Caciuc, C. Pauly, A. Georgi, C. Busse, M. Liebmann, S. Blügel, M. Pratzer, M. Morgenstern, and R. Mazzarello: "Absence of edge states in covalently bonded zigzag edges of graphene on Ir(111)." *Advanced Materials* **25.14** (2013), 1967. DOI: 10.1002/adma.201204539. (Cit. on p. 62).

[79] J. A. Robinson, C. P. Puls, N. E. Staley, J. P. Stitt, and M. a. Fanton: "Raman topography and strain uniformity of large-area epitaxial graphene." *Nano Letters* **9.3** (2009), 964. DOI: 10.1021/nl802852p. (Cit. on p. 65).

[80] *Website: Webelements* (cit. on pp. 70, 81, 82, 90, 95).

[81] T. Gerber: "Interaction of Graphene and Templated Cluster Arrays with CO, H2, and O2". PhD-Thesis. University of Cologne, 2013 (cit. on pp. 71, 102, 103, 110).

[82] J. Bunch and S. Verbridge: "Impermeable atomic membranes from graphene sheets". *Nano Letters* **8.8** (2008), 2458. (Cit. on p. 73).

[83] J. J. Yeh and I. Lindau: "Atomic subshell photoionization cross sections and asymmetry parameters". *Atomic Data and Nuclear Data Tables* **32** (1985), 1–155. DOI: 10.1016/0092-640X(85)90016-6. (Cit. on p. 81).

[84] M. Trzhaskovskaya, V. Nefedov, and V. Yarzhemsky: "Photoelectron Angular Distribution Parameters for Elements Z=55 to Z=100 in the Photoelectron Energy Range 100-5000 eV". *Atomic Data and Nuclear Data Tables* **82.2** (2002), 257–311. DOI: 10.1006/adnd.2002.0886. (Cit. on p. 81).

[85] H. Rida, S. Cahen, C. Hérold, and P. Lagrange: "Bulk synthesis and crystal structure of the first stage europium-graphite intercalation compound". *Carbon* **48.11** (2010), 3190–3195. DOI: 10.1016/j.carbon.2010.04.056. (Cit. on p. 82).

[86] S. Schumacher, T. O. Wehling, P. Lazić, S. Runte, D. F. Förster, C. Busse, M. Petrović, M. Kralj, S. Blügel, N. Atodiresei, V. Caciuc, and T. Michely: "The backside of graphene: manipulating adsorption by intercalation." *Nano Letters* **13.11** (2013), 5013. DOI: 10.1021/nl402797j. (Cit. on pp. 82, 83, 161).

[87] T. O. Wehling: *Private Communication* (cit. on pp. 82, 83, 91).

[88] M. Petrović: *Private Communication* (cit. on pp. 83, 91, 102, 103).

[89] S. Leung, M. Dresselhaus, C Underhill, T Krapchev, G Dresselhaus, and B. J. Wuensch: "Structural studies of graphite intercalation compounds using (00l) X-ray diffraction". *Physical Review B* **24.6** (1981), 3505–3518. (Cit. on pp. 89, 90).

[90] P. Lazić: *Private Communication* (cit. on p. 90).

[91] C. Chan and W. Weinberg: "Low-energy electron diffraction structural analysis of the (2x2) oxygen overlayer on the iridium (111) surface". *The Journal of Chemical Physics* **71.111** (1979), 2788–2792. (Cit. on p. 94).

[92] N. Atodiresei: *Private Communication* (cit. on p. 95).

[93] T. Gerber, S. Runte, F. Craes, J. Coraux, C. Vo-van, P. Pervan, C. Busse, M. Kralj, J. Knudsen, and T. Michely: "Understanding core level shifts of doped graphene" (), 1–9. (Cit. on pp. 101–103, 110, 162).

[94] S. Runte, F. Craes, J. Klinkhammer, M. Petrović, M. Kralj, T. Michely, and C. Busse: "STS Investigations on Caesium Intercalated Graphene". *in preparation* (). (Cit. on pp. 101, 162).

[95] A. Preobrajenski, M. Ng, A. Vinogradov, and N. Må rtensson: "Controlling graphene corrugation on lattice-mismatched substrates". *Physical Review B* **78.7** (2008), 073401. DOI: 10.1103/PhysRevB.78.073401. (Cit. on p. 103).

[96] F. Craes, S. Runte, J. Klinkhammer, M. Kralj, T. Michely, and C. Busse: "Mapping Image Potential States on Graphene Quantum Dots". *Physical Review Letters* **111.5** (2013), 056804. DOI: 10.1103/PhysRevLett.111.056804. (Cit. on pp. 103, 162).

[97] G. Giovannetti, P. Khomyakov, G. Brocks, V. Karpan, J. van den Brink, and P. Kelly: "Doping Graphene with Metal Contacts". *Physical Review Letters* **101.2** (2008), 026803. DOI: 10.1103/PhysRevLett.101.026803. (Cit. on pp. 103, 110).

[98] L. Petersen, P. T. Sprunger, P. Hofmann, E. Laegsgaard, B. G. Briner, M. Doering, H.-P. Rust, A. M. Bradshaw, F. Besenbacher, and E. W. Plummer: "Direct imaging of the two-dimensional Fermi contour : Fourier-transform STM". *Physical Review B* **57.12** (1998), R6858–R6861. (Cit. on p. 105).

[99] P. Mallet, I. Brihuega, S. Bose, M. M. Ugeda, J. M. Gómez-Rodríguez, K. Kern, and J. Y. Veuillen: "Role of pseudospin in quasiparticle interferences in epitaxial graphene probed by high-resolution scanning tunneling microscopy". *Physical Review B* **86.4** (2012), 045444. DOI: 10.1103/PhysRevB.86.045444. (Cit. on pp. 106, 108).

[100] J. Klinkhammer, M. Schlipf, F. Craes, S. Runte, T. Michely, and C. Busse: "Spin-Polarized Surface State in EuO (100)". *accepted in Physical Review Letters* (2013). (Cit. on p. 162).

[101] V. Geringer, M. Liebmann, T. Echtermeyer, S. Runte, M. Schmidt, R. Rückamp, M. Lemme, and M. Morgenstern: "Intrinsic and extrinsic corrugation of monolayer graphene deposited on SiO2". *Physical Review Letters* **102.7** (2009), 1–4. DOI: 10.1103/PhysRevLett.102.076102. (Cit. on p. 162).

[102] A. Reinholdt, R. Pecenka, A. Pinchuk, S. Runte, a. L. Stepanov, T. E. Weirich, and U. Kreibig: "Structural, compositional, optical and colorimetric characterization of TiN-nanoparticles". *The European Physical Journal D* **31.1** (2004), 69–76. DOI: 10.1140/epjd/e2004-00129-8. (Cit. on p. 162).

PART VII

Appendix

APPENDIX A

LEED Analysis

The LEED system has a high sensitivity for low beam currents because the diffracted electrons are not accelerated to an ordinary fluorescent screen but to microchannel plates which boost the intensity. However, as the microchannel plates are mounted in a planar arrangement the LEED images are distorted. The distortion correction procedure is described in section A.1 as an instructions manual. A way to determine lattice constants from LEED images is presented in section A.2.

A.1 The Distortion Correction

The LEED images can be deskewed using the software *MCPdeskew* by Julian Ikonomov (Universität Bonn), which creates a new image by bending the raw image to a sphere. The center of the sphere has to be defined by drawing a circle into the image with the mouse - the diameter is set by using the left mouse button, the position of the circle by using the right mouse button. The curvature is defined by the parameter *distance* x_{MCP}, which is the distance (in pixel) of the microchannel plates to the sample and has to be determined, as will be discussed in the next paragraph. The corrected image is shrinked due to the projection which can be compensated by the parameter *zoom*.

The determination of the distance x_{MCP} was done by LEED measurements with a tilted sample as shown in a sketch in Figure A.1. An electron beam (grey line) is accelerated from the electron gun (center of the LEED) to the sample, which is tilted by an angle α to a normal incident electron beam. Due to the tilt of the sample the specular spot does not hit the center of the LEED but is displaced by d_{dis} under an angle 2α.

As samples are usually mounted with a small misalignment the specular spot is not reflected perfectly to the center of the screen for an angle $\alpha = 0°$. Averaging of d_{dis} for tilting in both directions ($\pm\alpha$) compensates for this error.

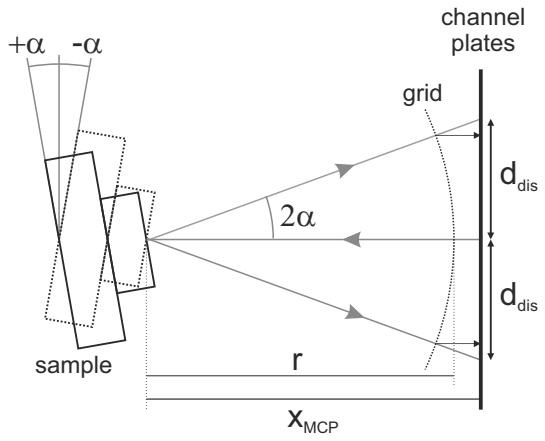

Figure A.1: Schematic drawing of the distortion correction procedure. The sample is tilted by $\pm\alpha$, resulting in an angle 2α between incoming beam and specular spot. The radius of the grid is r, the distance between microchannel plates and sample is x_{MCP}, and the displacement of the specular beam is d_{dis}. The black arrows marks the position where spots would be visible in common LEED systems.

For a distance x_{MCP} between sample and microchannel plates and a displacement d_{dis} of the specular spot in y-direction the distance x_{MCP} is given by

$$x_{\mathrm{MCP}}[\mathrm{px}] = \frac{\mathrm{d_{dis}[px]}}{\tan(2\alpha)} \tag{A.1}$$

All lengths are given in pixel, as indicated by [px]. This is just for practical reasons, as the displacement d_{dis} is measured from a digital image and no further conversion is necessary. From this analysis the distance is found to be $x_{\mathrm{MCP}} = (207.4 \pm 14.9)\,\mathrm{px}$ at a manipulator position of $x_{\mathrm{Man}} = 2.3\,\mathrm{mm}$ and a fully extracted LEED. Note that not only for different manipulator positions the distance d_{dis} changes.
If the camera is moved the ratio px/cm in the images might change by some factor. In consequence a new calibration has to be done.

A.2 Lattice Parameter Determination

From the position of LEED spots the in-plane lattice parameter can be determined. In real space the in-plane primitive unit cell is defined by two vectors $\underline{a}_1$ and $\underline{a}_2$ enclosing an angle α. In reciprocal space the unit cell is defined by the corresponding vectors $\underline{a}_1^*$ and $\underline{a}_2^*$ enclosing an angle α^*. For a hexagonal system like Ir(111) this is shown in Figure A.2 ($\alpha = 120°$, $\alpha^* = 60°$).
The real space vectors $\underline{a}_1$ and $\underline{a}_2$ can be expressed by unit vectors $\hat{e}_1$, $\hat{e}_2$ (in-plane), and a normal unit vector $\hat{n}$ (out-of-plane):

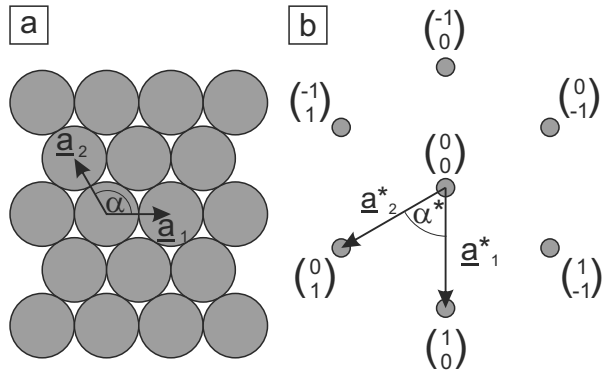

Figure A.2: Sketch of atoms in a hexagonal surface in real space (a) with vectors $\underline{a}_1$ and $\underline{a}_2$ of the primitive unit cell, enclosing an angle α. The corresponding vectors in reciprocal space (b) are $\underline{a}_1^*$ and $\underline{a}_2^*$, resp., enclosing an angle α^*. The Miller indices are shown for each spot.

$$\underline{a}_1 = |a_1| \cdot \hat{e}_1 \tag{A.2}$$

$$\underline{a}_2 = |a_2| \cdot \hat{e}_2 \tag{A.3}$$

$$\underline{a}_3 = \hat{n} \tag{A.4}$$

From the vector products

$$\underline{a} \times \underline{b} = |\underline{a}||\underline{b}| \sin(\sphericalangle(\underline{a},\underline{b}))\hat{n} \tag{A.5}$$

$$\underline{a} \cdot \underline{b} = |\underline{a}||\underline{b}| \cos(\sphericalangle(\underline{a},\underline{b})) \tag{A.6}$$

the corresponding reciprocal vectors result to

$$\underline{a}_1^* = 2\pi \frac{\underline{a}_2 \times \hat{n}}{\underline{a}_1 \cdot (\underline{a}_2 \times \hat{n})} = 2\pi \frac{|\underline{a}_2|(\hat{e}_2 \times \hat{n})}{|\underline{a}_1||\underline{a}_2| \sin\alpha} = 2\pi \frac{\hat{e}_2 \times \hat{n}}{|\underline{a}_1| \sin\alpha} \tag{A.7}$$

$$\underline{a}_2^* = 2\pi \frac{\hat{n} \times \underline{a}_1}{\underline{a}_1 \cdot (\underline{a}_2 \times \hat{n})} = 2\pi \frac{|\underline{a}_1|(\hat{e}_1 \times \hat{n})}{|\underline{a}_1||\underline{a}_2| \sin\alpha} = 2\pi \frac{\hat{n} \times \hat{e}_1}{|\underline{a}_2| \sin\alpha} \tag{A.8}$$

with

$$|\underline{a}_1^*| = |\underline{a}_2^*| = \frac{2\pi}{|\underline{a}_1| \sin\alpha} = |\underline{a}^*|, \quad \text{if} \quad |\underline{a}_1| = |\underline{a}_2| \tag{A.9}$$

In LEED the spots from Figure A.2b appear due to diffraction under the Laue condition $\underline{k^{\text{out}}} - \underline{k^{\text{in}}} = \underline{G}$. For the two dimensional case each vector can be split up into components parallel and perpendicular to the surface as shown in Figure A.3, and the Laue condition becomes $\underline{k}_{\shortparallel}^{\text{out}} = \underline{k}_{\shortparallel} = \underline{G}_{\shortparallel}$. From the free electron wavevector $\underline{k} = \sqrt{\frac{2mE}{\hbar^2}}$ and $k_{\shortparallel} = k \sin\beta$ it results to

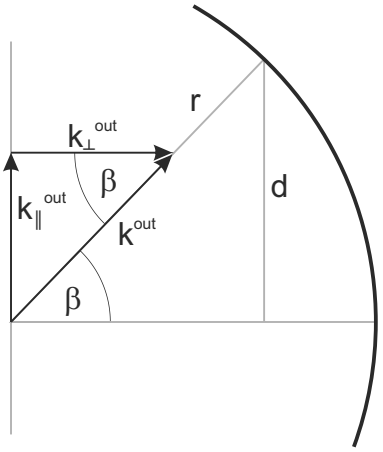

Figure A.3: Schematic drawing of the diffracted electron beam in LEED. The momentum k^{out} of the diffracted electron can be splitted into $k_{\shortparallel}^{\text{out}}$ and $k_{\perp}^{\text{out}}$. Reflections are visible in LEED images at the distance x to the center, which are diffracted under an angle β. The screen radius is r.

$$G_{\shortparallel} = \frac{\sqrt{2mE}}{\hbar}\sin\beta \tag{A.10}$$

$$G_{\shortparallel} = \frac{\sqrt{2mE}}{\hbar}\frac{d}{r} \tag{A.11}$$

with an angle β between incoming and diffracted electron beam, d the distance of the spot to the specular spot in the image and r the radius of the screen. To link $G_{\shortparallel}$ to the in-plane vectors it can be described by using the equations A.7-A.9 as

$$G_{\shortparallel} = |h\underline{a}_1^* + k\underline{a}_2^*| = \sqrt{h\underline{a}_1^* + k\underline{a}_2^*)^2} \tag{A.12}$$

$$= \sqrt{(h^2|\underline{a}_1^*|^2 + k^2|\underline{a}_2^*|^2 + 2hk|\underline{a}_1^*||\underline{a}_2^*|\cos\alpha^*} \tag{A.13}$$

$$= \frac{2\pi}{\sin\alpha}\sqrt{\frac{h^2}{|\underline{a}_1|^2} + \frac{k^2}{|\underline{a}_2|^2} + \frac{2hk\cos\alpha^*}{|\underline{a}_1||\underline{a}_2|}} \tag{A.14}$$

$$= \frac{2\pi}{\sin\alpha}\frac{1}{|\underline{a}|}\sqrt{h^2 + k^2 + 2hk\cos\alpha^*} \tag{A.15}$$

The real space angle α can be expressed by the reciprocal angle α^* by $\alpha^* = 180° - \alpha$. For symmetry reasons $\sin\alpha = \sin(180° - \alpha)$ and therefore $\sin\alpha = \sin\alpha^*$. Combined with eq. A.11 this leads to

$$\frac{\sqrt{2mE}}{\hbar}\frac{d}{r} = \frac{2\pi}{\sin\alpha^*}\frac{1}{|\underline{a}|}\sqrt{h^2 + k^2 + 2hk\cos\alpha^*} \tag{A.16}$$

$$\Leftrightarrow |\underline{a}| = \frac{2\pi}{\sin\alpha^*}\frac{\hbar}{\sqrt{2mE}}\frac{r}{d}\sqrt{h^2 + k^2 + 2hk\cos\alpha^*} \tag{A.17}$$

For a hexagonal surface like Ir(111) where $\alpha^* = 60°$ (see Figure A.2) we obtain

$$|\underline{a}| = \frac{4\pi}{\sqrt{3}} \frac{\hbar}{\sqrt{2mE}} \frac{r}{d} \sqrt{h^2 + k^2 + hk} \tag{A.18}$$

Note that the value r is not determined by the distortion correction, as r is the radius of the grid and x_{MCP} is the distance of the microchannel plates (see Figure A.1). The ratio r/x_{MCP} can be determined by calibration with a reference sample. Also the value *zoom* has to be taken into account for determination of the lattice constants, as it is not necessarily the same as for the reference image. With the new parameters d' and c

$$d = \frac{d'}{\mathrm{zoom}} \tag{A.19}$$

$$c = \frac{a_{\mathrm{lit}}^{\mathrm{ref}}}{a_{\mathrm{exp}}^{\mathrm{ref}}} \tag{A.20}$$

with the lattice constant $a_{\mathrm{lit}}^{\mathrm{ref}}$ from literature, $a_{\mathrm{exp}}^{\mathrm{ref}}$ the measured one, and d', a final equation for our setup can be written

$$|\underline{a}| = c \frac{4\pi}{\sqrt{3}} \frac{\hbar}{\sqrt{2mE}} \frac{x_{\mathrm{MCP}}}{\frac{d'}{\mathrm{zoom}}} \sqrt{h^2 + k^2 + hk} \tag{A.21}$$

For my analysis the position of the manipulator x_{Man} and the parameters are

$$x_{\mathrm{Man}} = 2.3\,\mathrm{mm} \tag{A.22}$$

$$\mathrm{zoom} = 1.7 \tag{A.23}$$

$$c = 0.835 \tag{A.24}$$

Further information about LEED can be found e.g. in [58].

APPENDIX B

Technical Drawings

LT-STM Sample Holder: e-beam

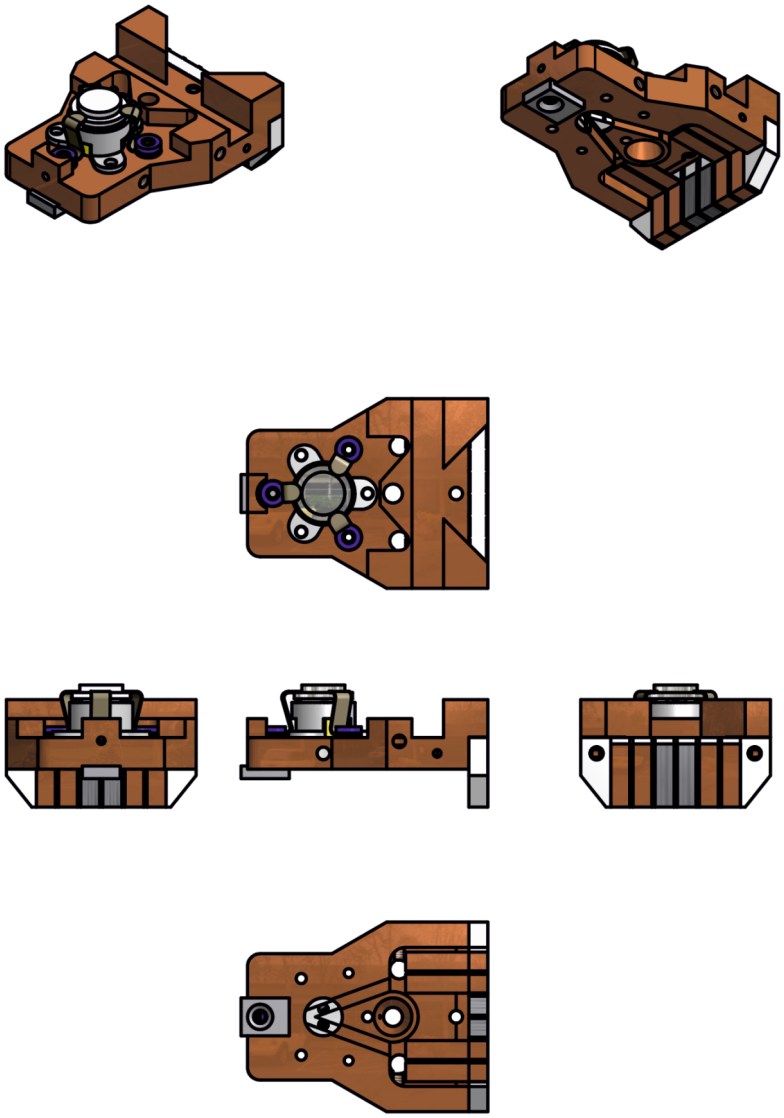

Sample holder e-beam: overview

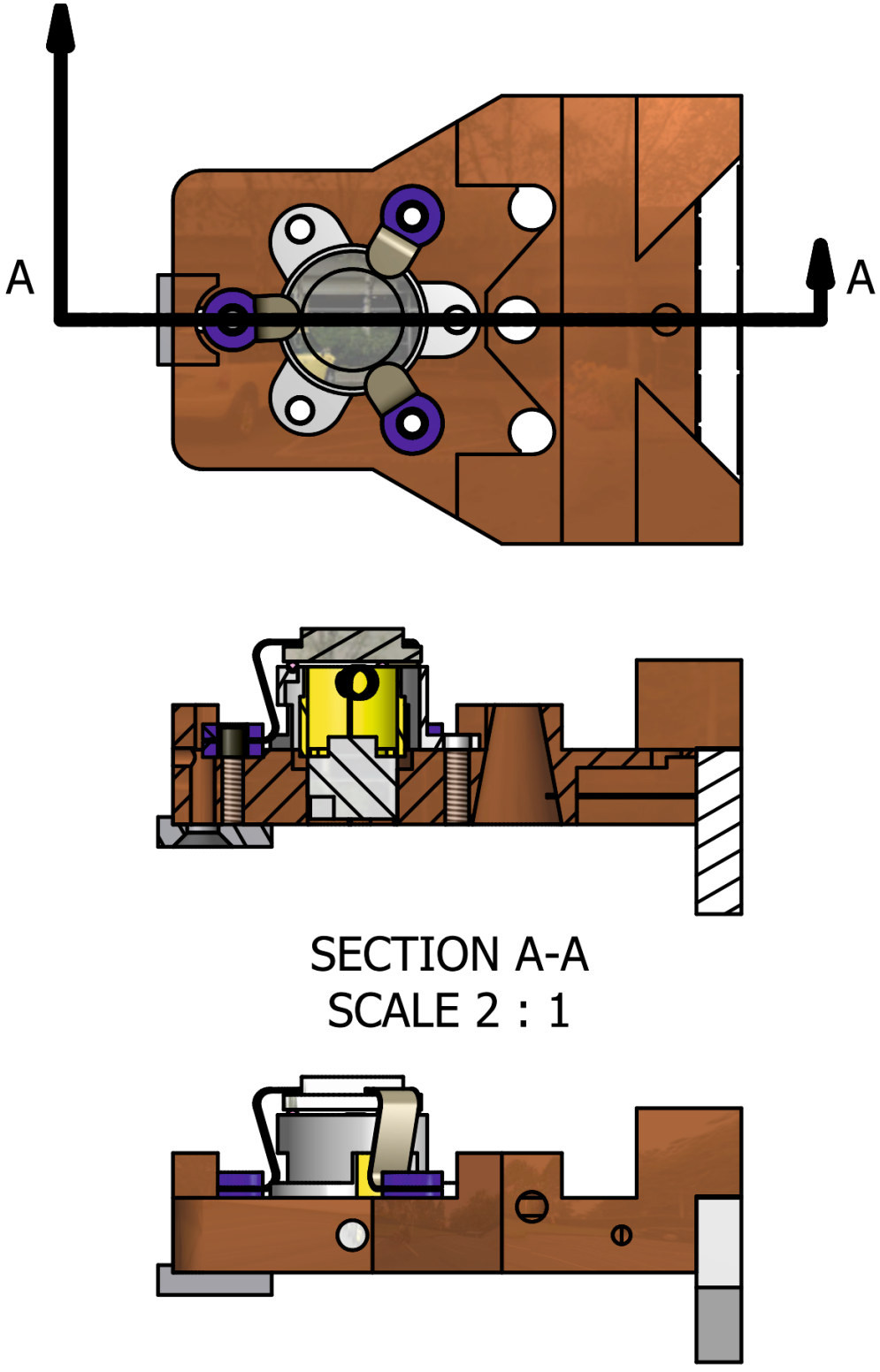

Sample holder e-beam: body

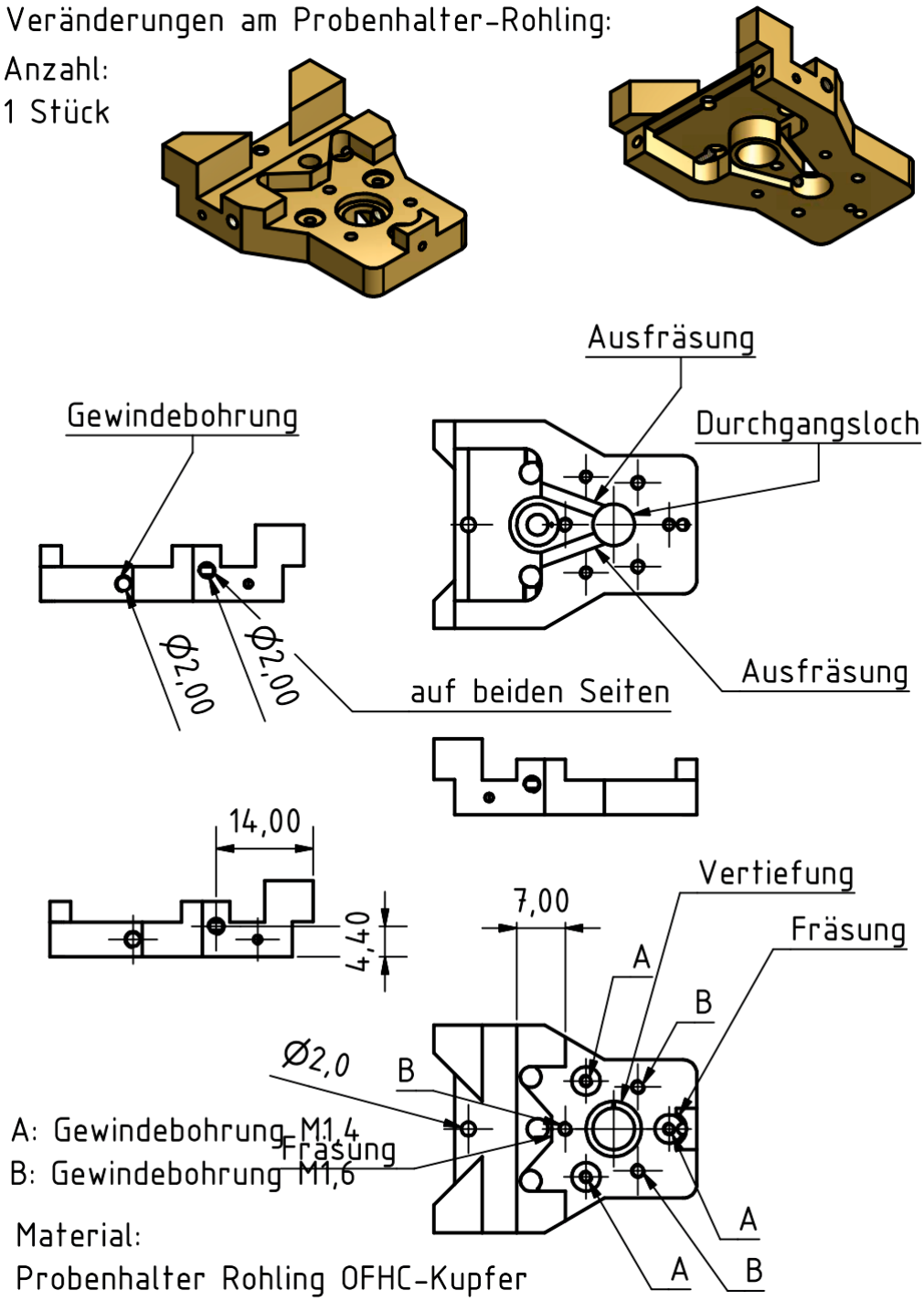

Sample holder e-beam: body

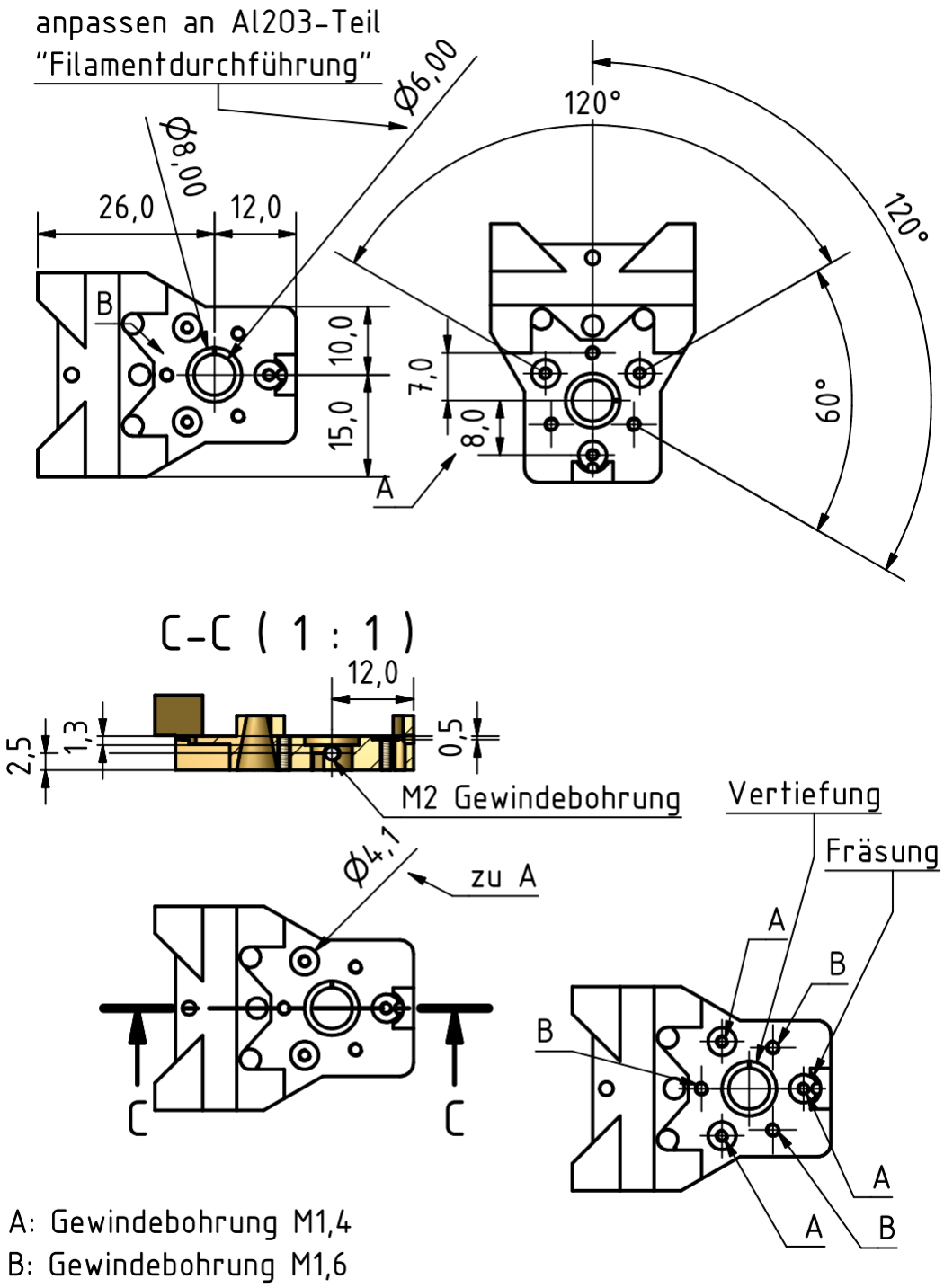

Sample holder e-beam: body

Fräsungen oben

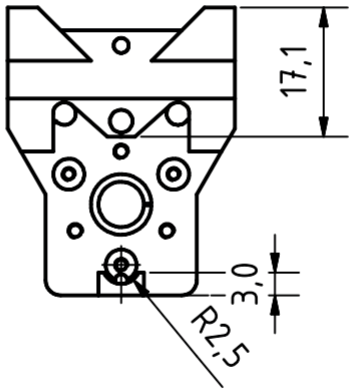

Fräsungen unten

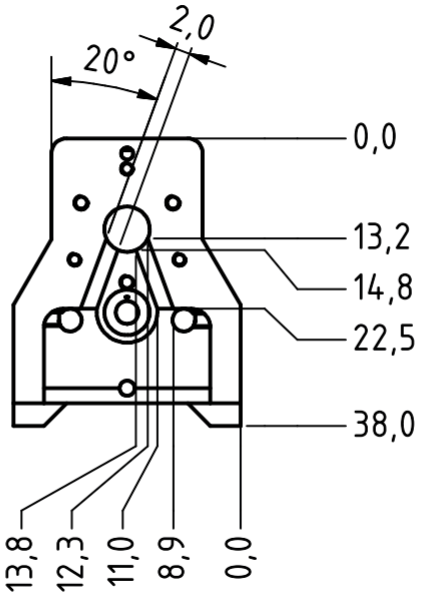

Sample holder e-beam: body

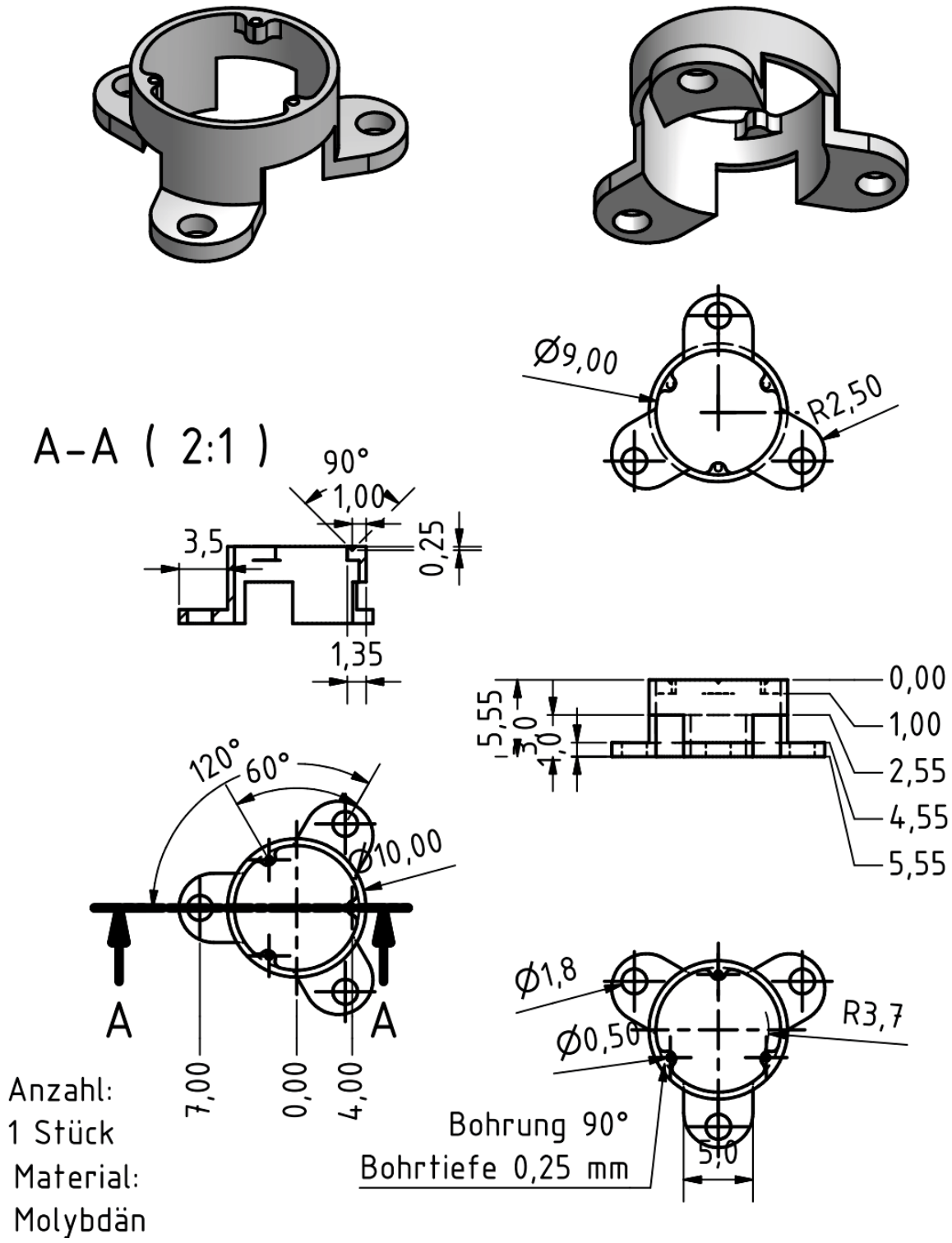

Sample holder e-beam: sample support

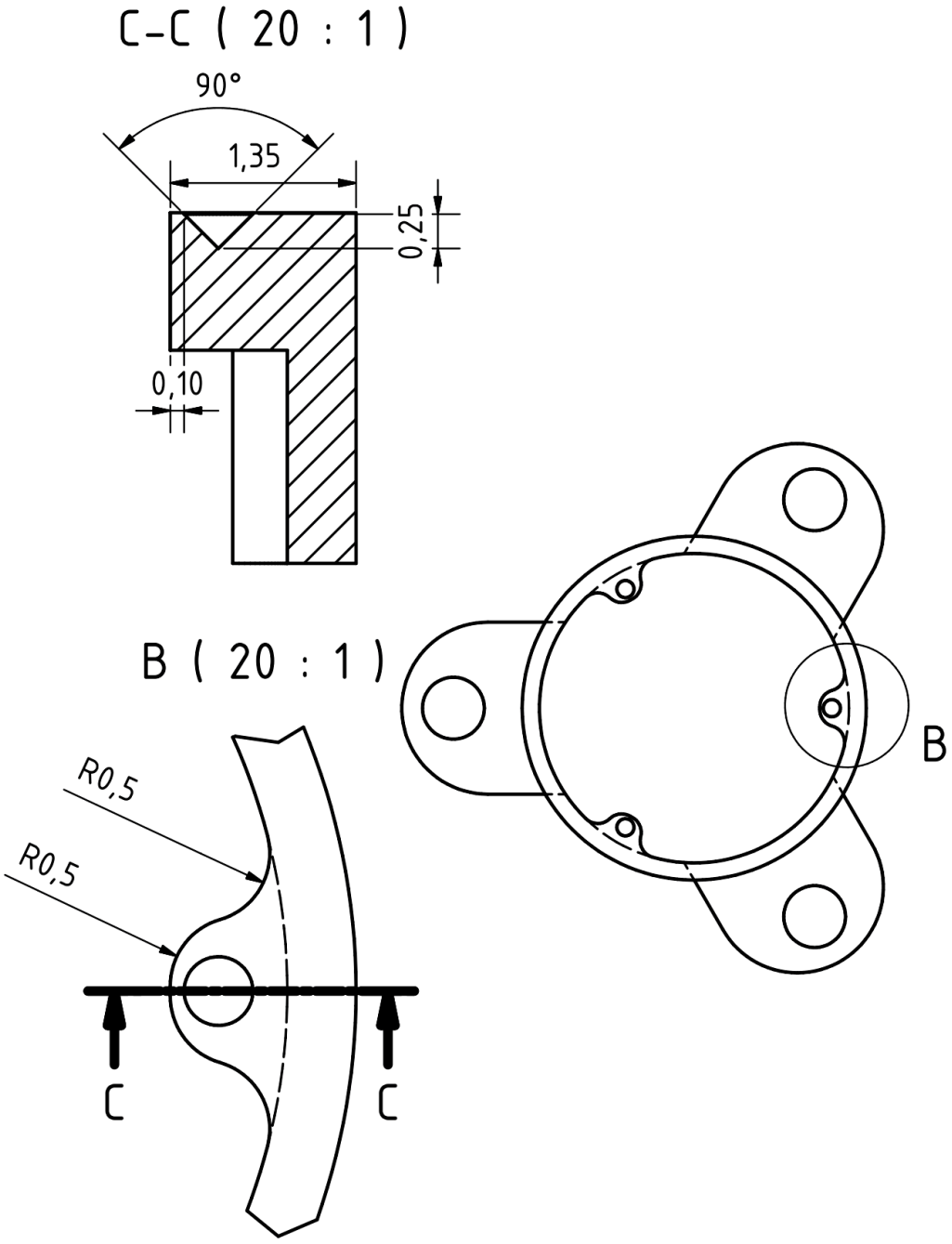

Sample holder e-beam: sample support

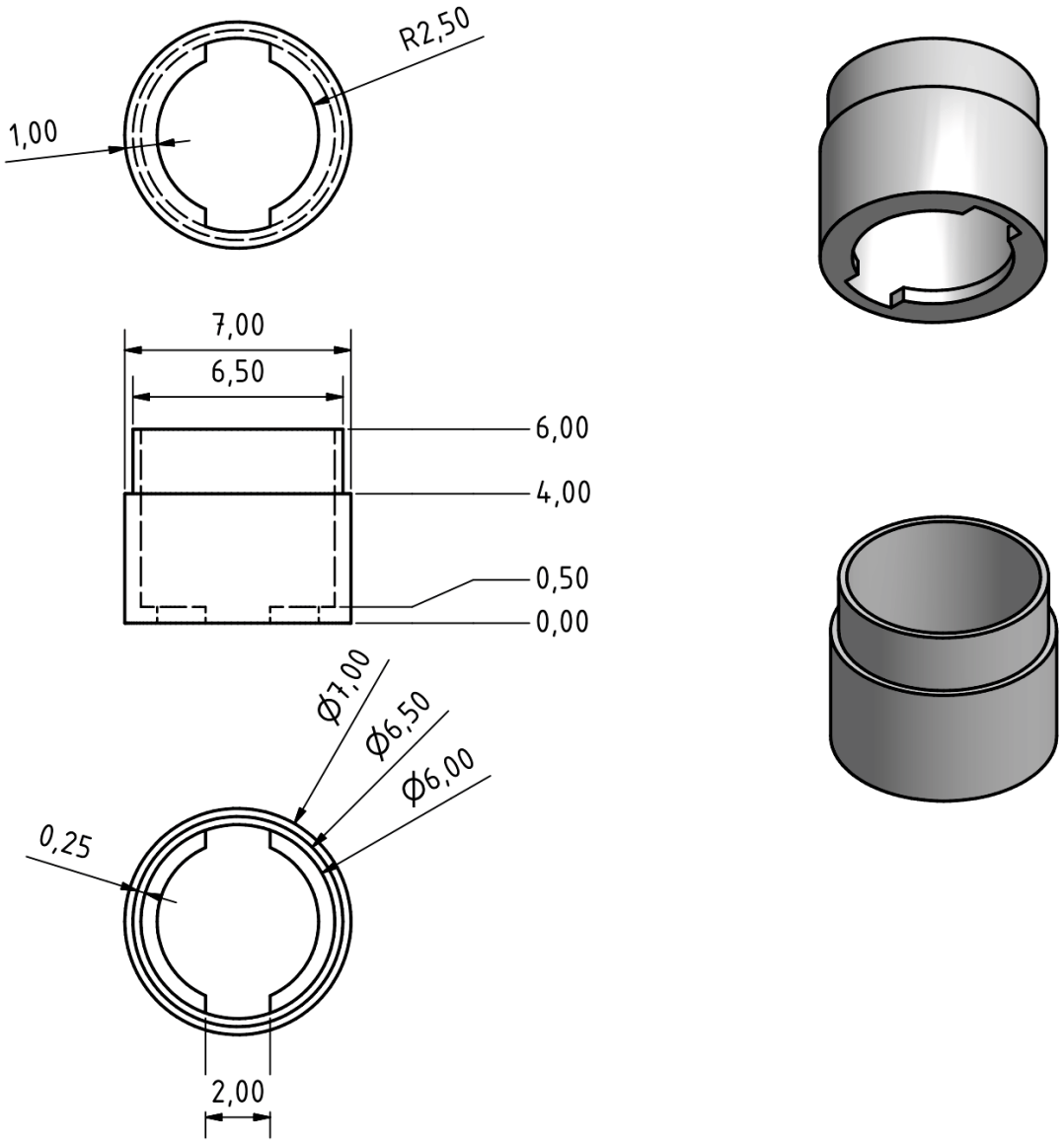

Sample holder e-beam: Wehnelt cylinder

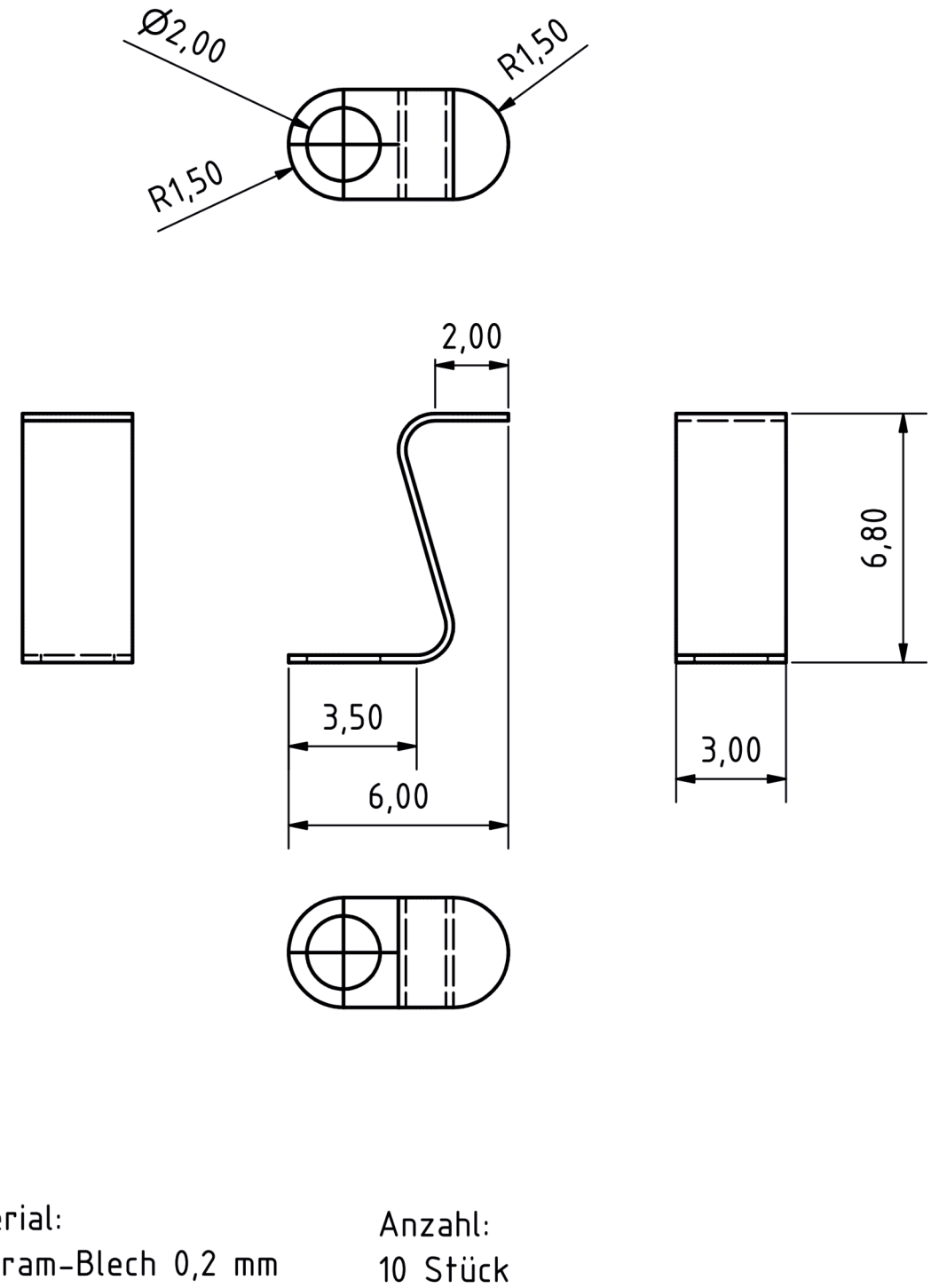

Sample holder e-beam: Tungsten springs

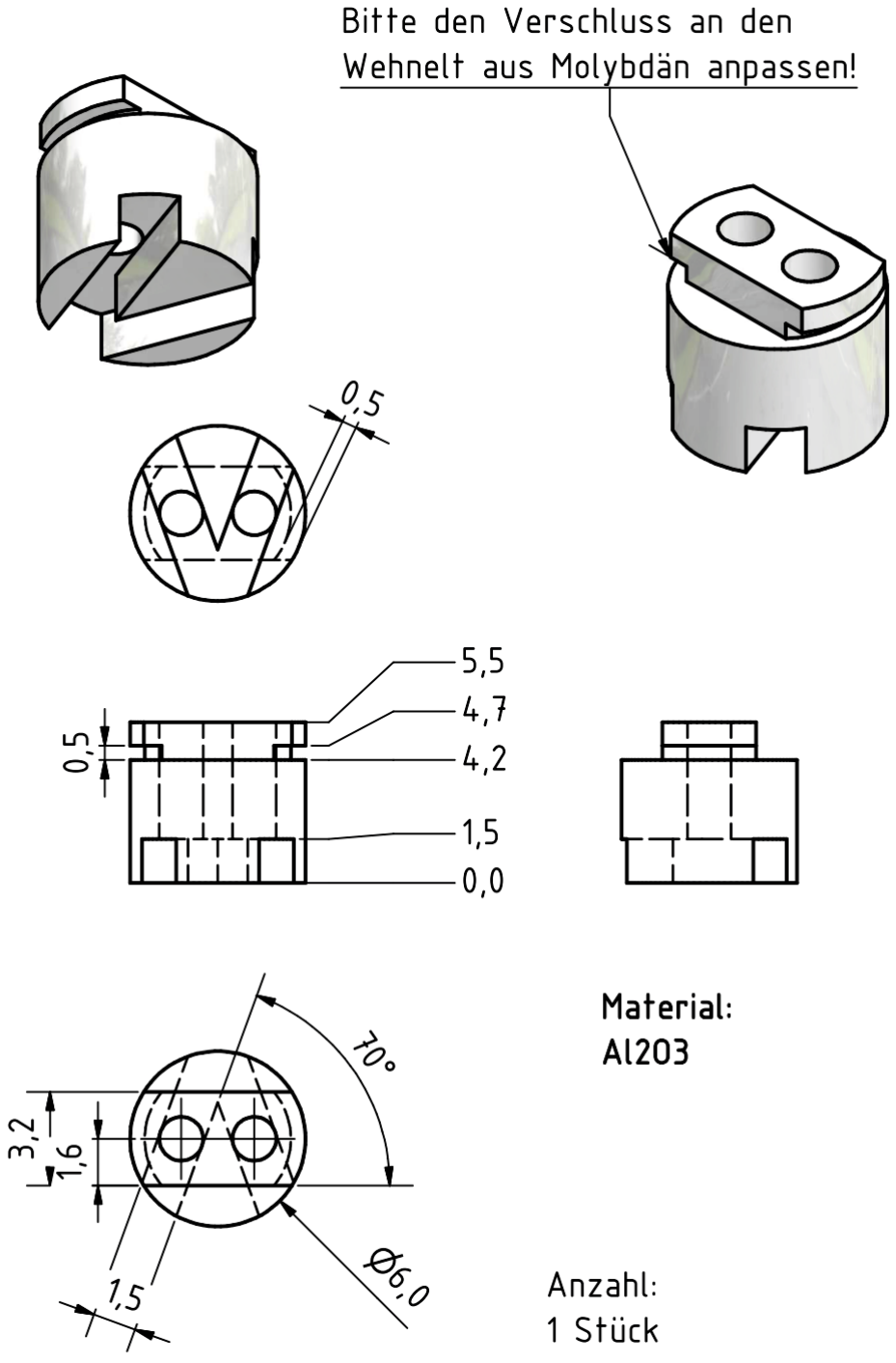

Sample holder e-beam: Ceramics

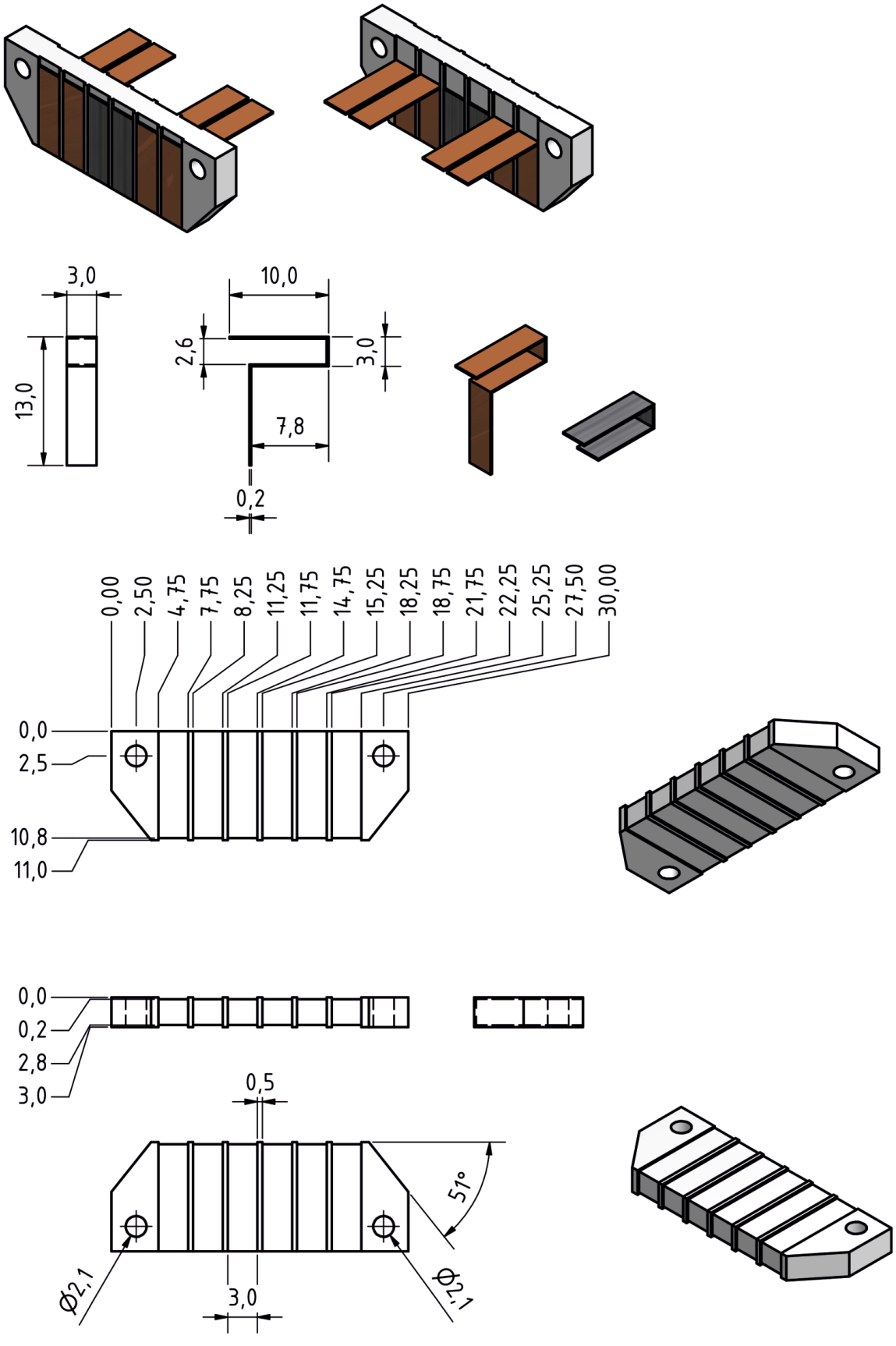

Sample holder e-beam: contact plate

Manipulator Contacts

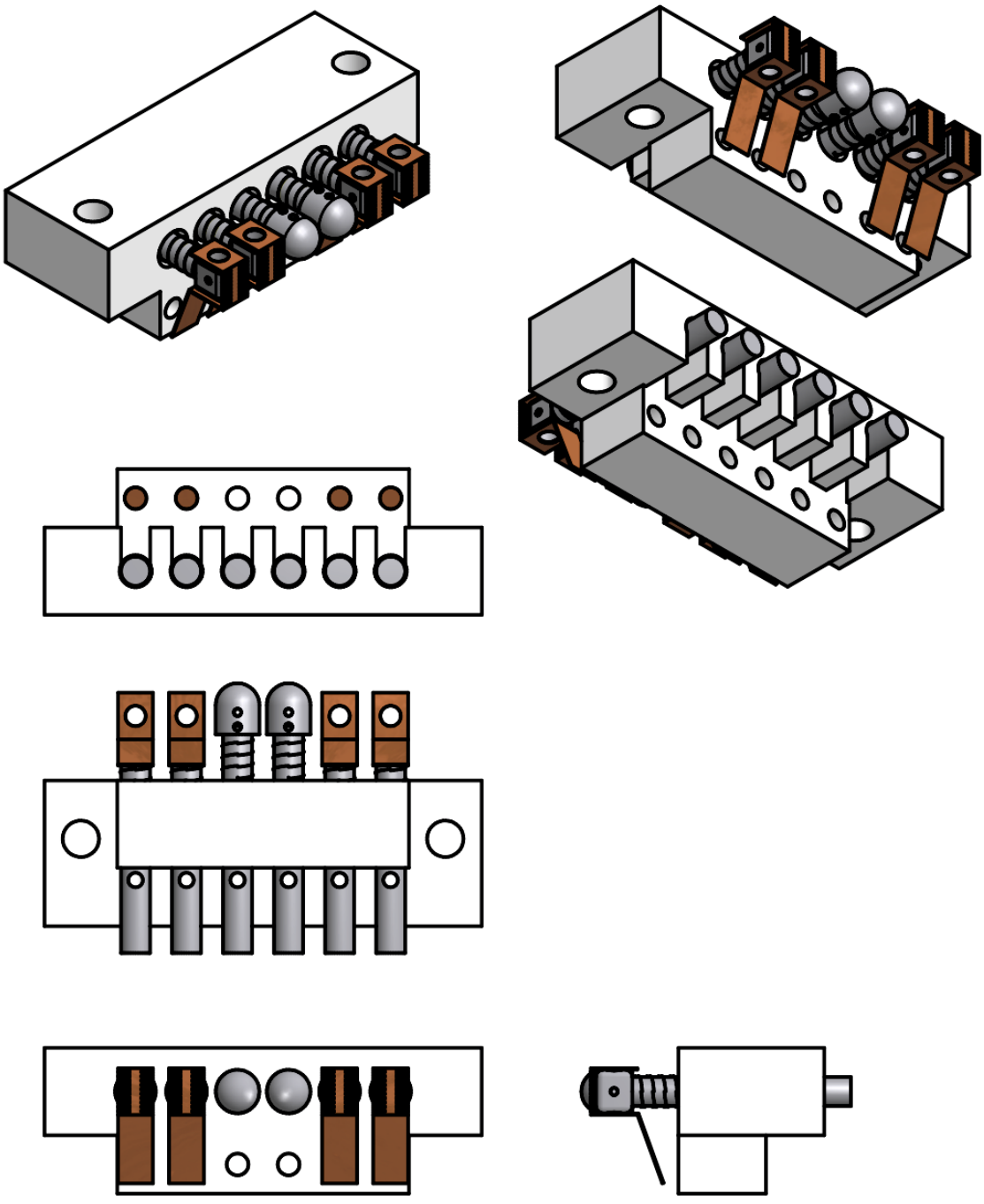

Manipulator contacts: overview

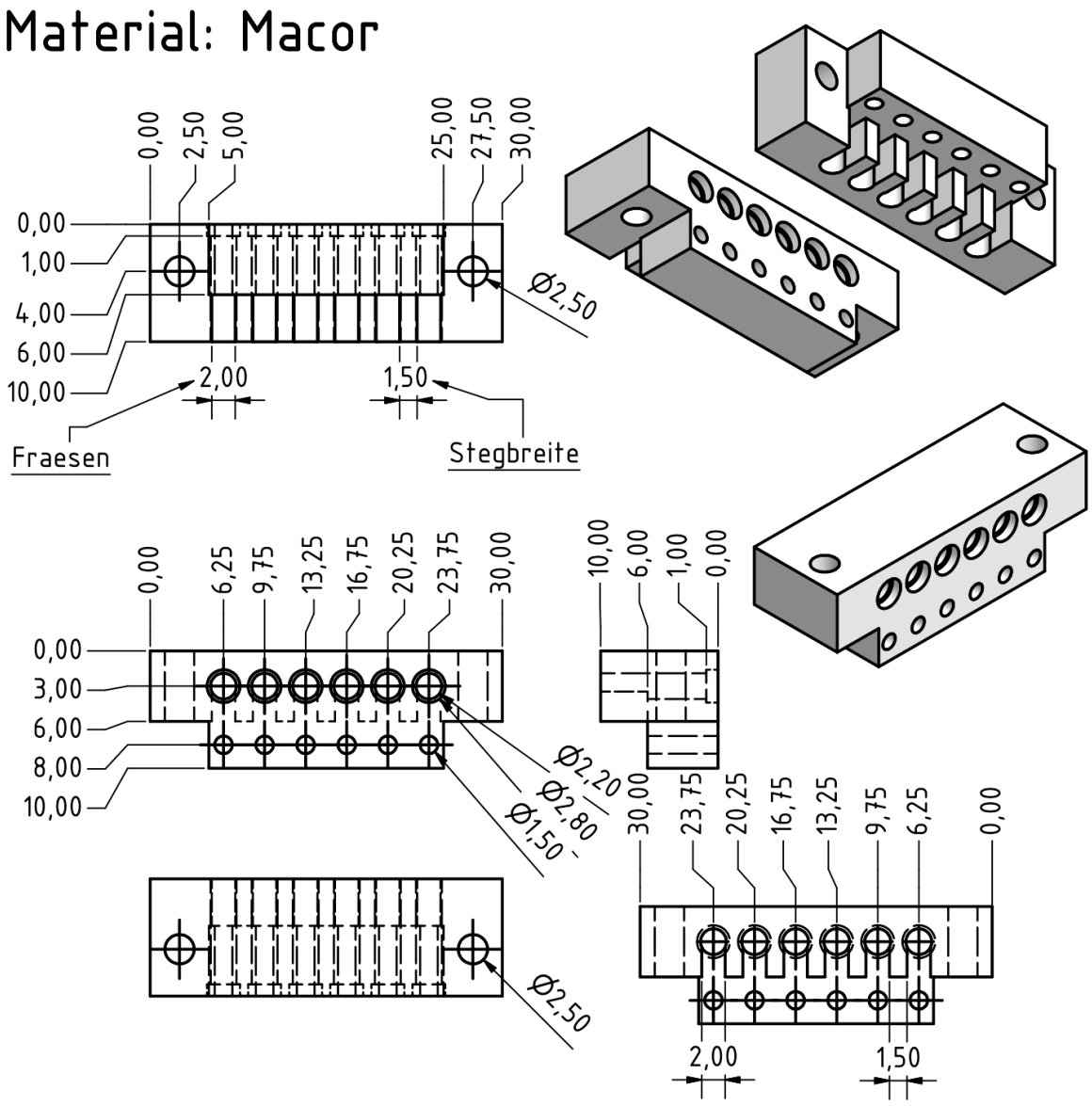

Manipulator contacts: MACOR body

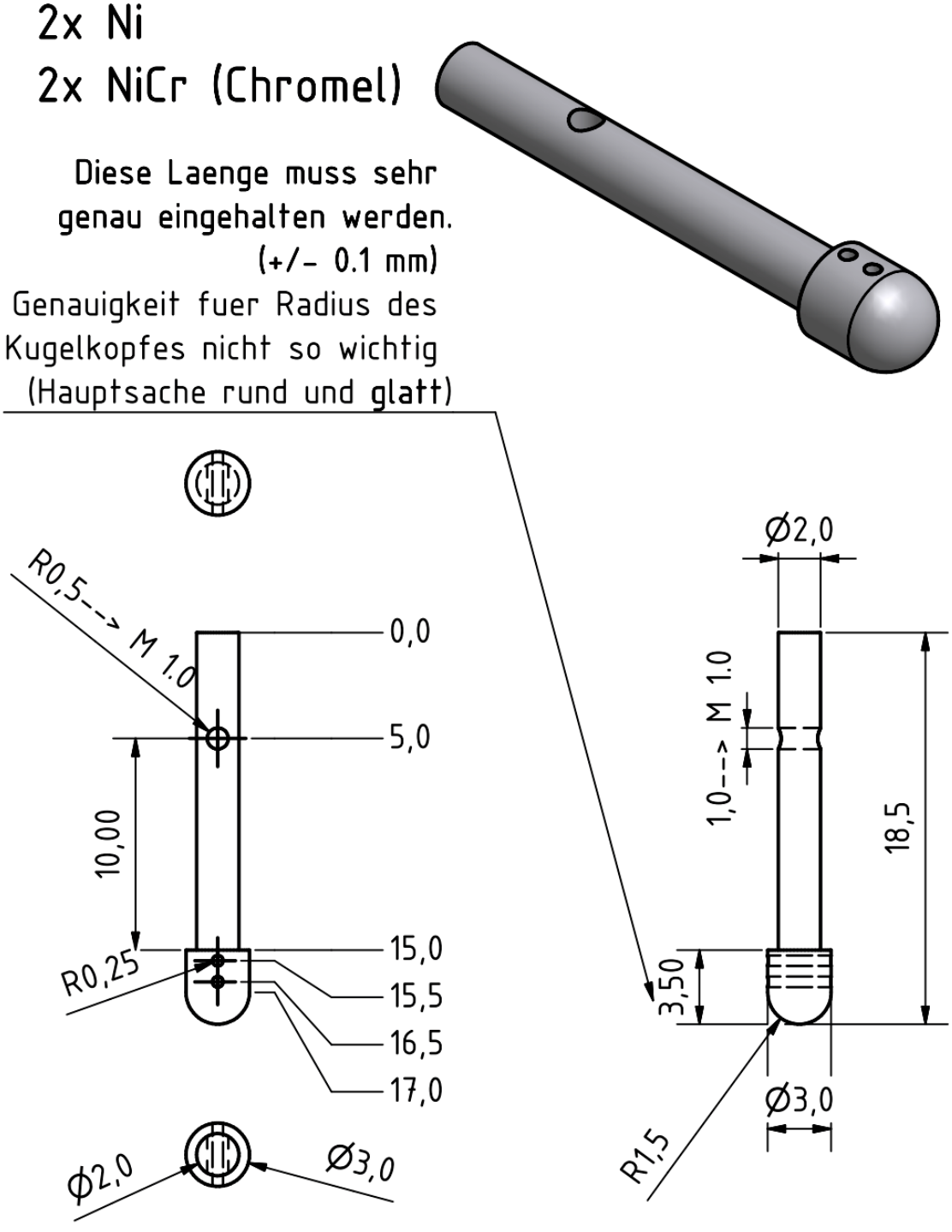

Manipulator contacts: Electrical contacts

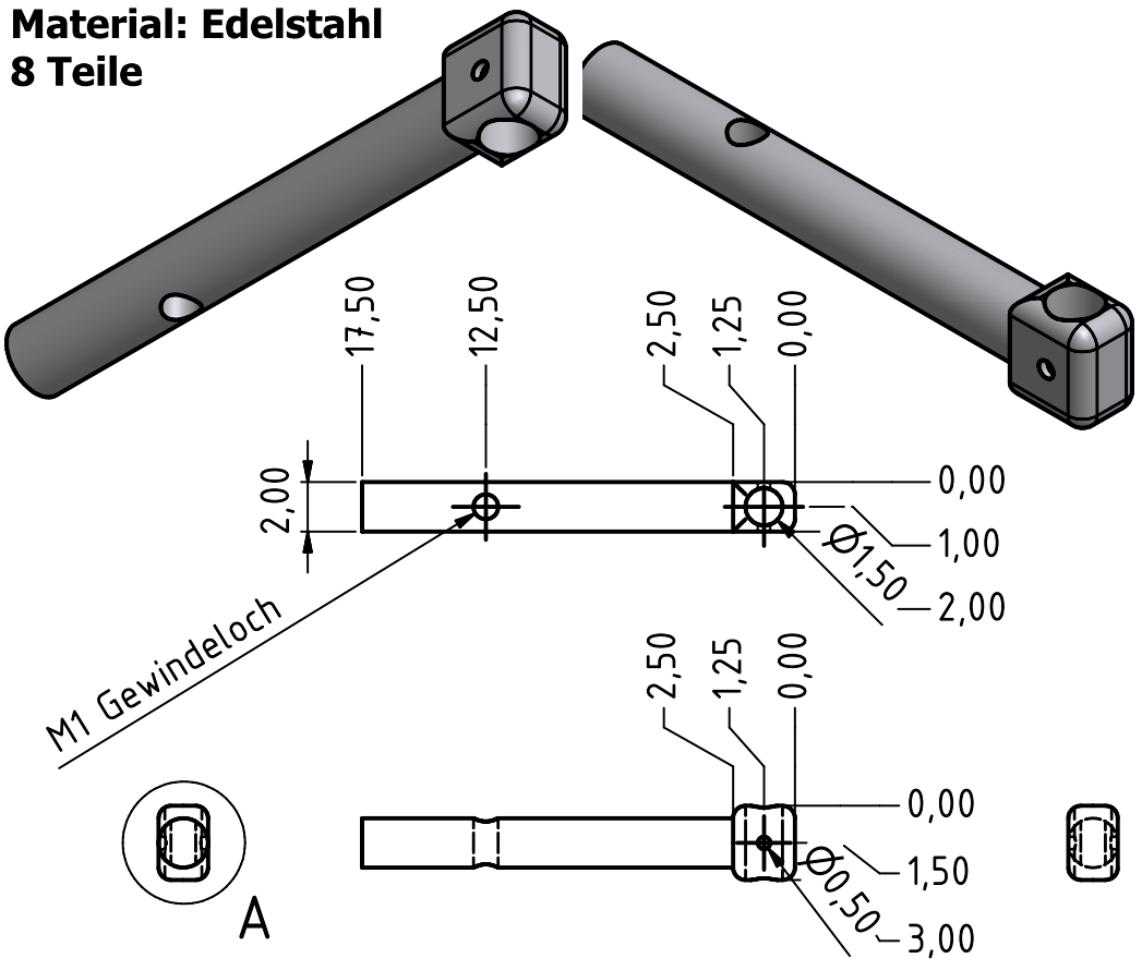

Kanten an abgebildeten Stellen abrunden (z.B. R=0.5mm)
Genauigkeit nicht von grosser Bedeutung, Kanten muessen aber **glatt** sein!

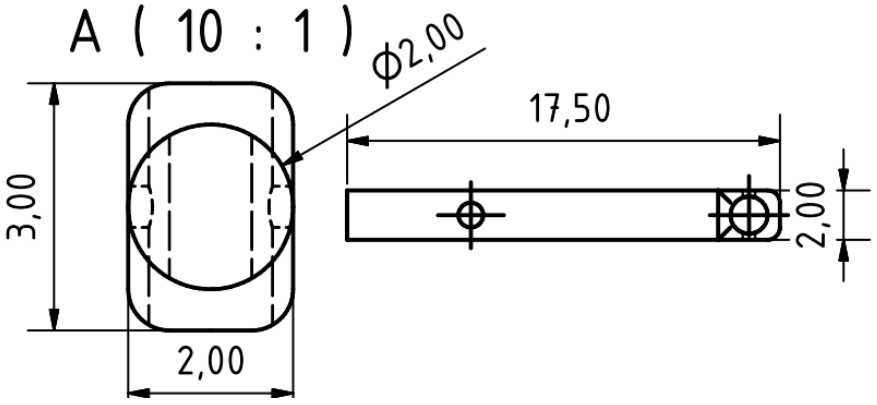

Manipulator contacts: Thermocouple contacts

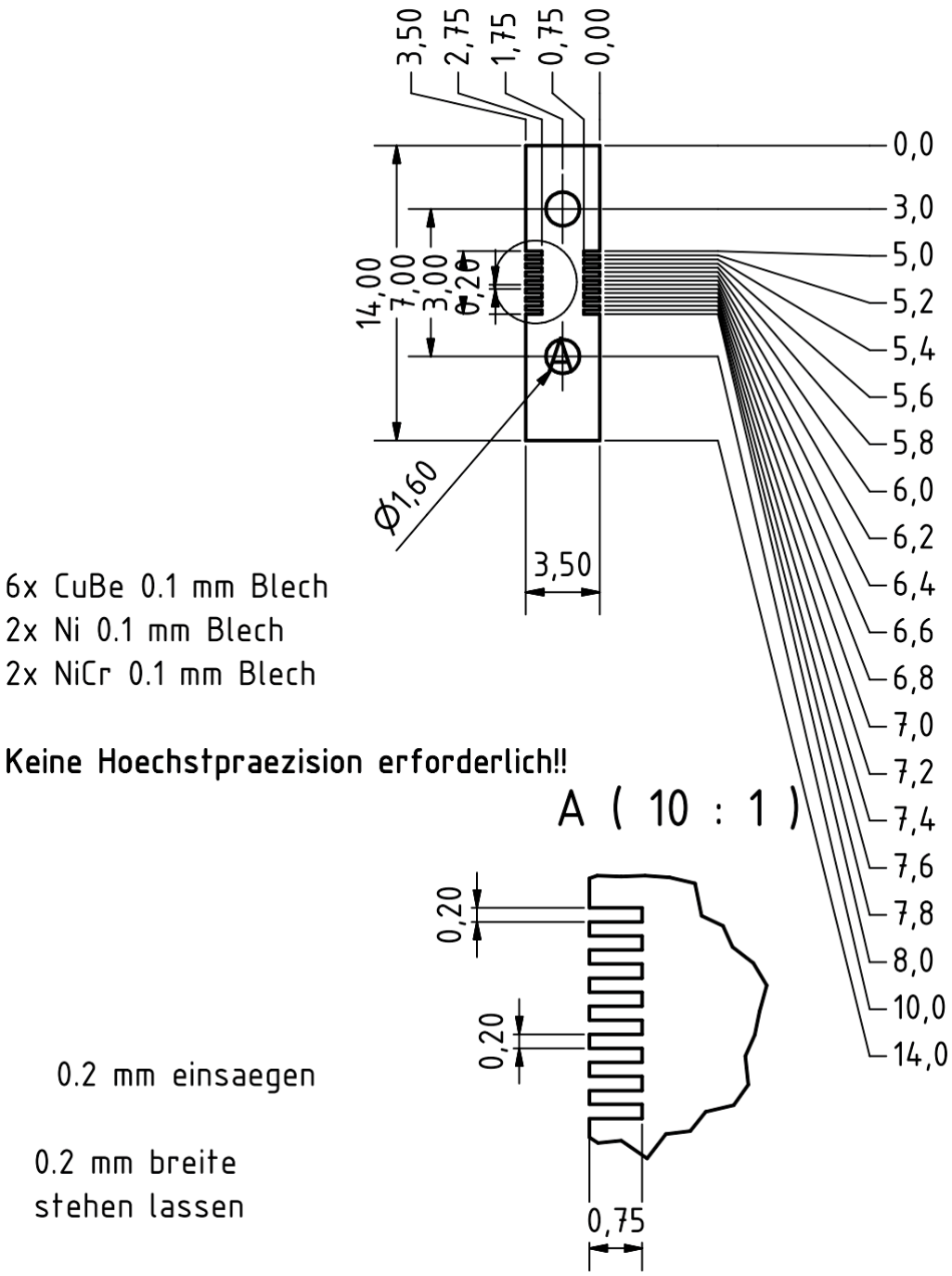

Manipulator contacts: Laminated contacts

APPENDIX C

Danksagung (Acknowlegdements)

Zum Abschluss dieser Arbeit möchte ich mich bei Allen bedanken, die auf unterschiedliche Weise zum Gelingen dieser Arbeit beigetragen haben und ohne die diese Arbeit so nicht möglich gewesen wäre.

Priv.-Doz. Dr. Carsten Busse danke ich für das Angebot der Doktorandenstelle und für die Betreuung und Begutachtung dieser Arbeit. Ganz besonders möchte ich mich bedanken für die Möglichkeit, mich mit Rastertunnelspektroskopie beschäftigen zu können.

Ich möchte mich bei **Prof. Dr. Stefan Schlemmer** für das Zweitgutachten bedanken. Außerdem danke ich **Prof. Dr. Klaus Meerholz** für die Übernahme des Vorsitzes der Prüfungskommission.

Für die Finanzierung meiner Arbeit und des Austauschprojektes mit der Arbeitsgruppe von Dr. Marko Kralj in Zagreb danke ich der Deutschen Forschungsgesellschaft und dem Deutschen Akademischen Austauschdienst.

My special thanks go to **Jörg Zegenhagen** for fruitful discussions concerning the XSW experiments and the final fitting of the XSW data with his program DARE. I also would like to thank my collaborators **Johann Coraux** and **Chi Võ Văn** who performed the beam times with me. Furthermore I thank the staff members at ID32, especially **Blanka Detlefs** and **Julien Duvernay** for the experimental help and **Helena Isern** for assistance during technical problems. For the possibility to extend the measuring time for several hours at ID32 I would like to thank **Christoph Schlüter**.

Special thanks are addressed to our collaborators from Zagreb, especially **Dr. Marko Kralj**, **Marin Petrović**, and **Iva Šrut** for the nice time inside (and outside) the lab in Zagreb. The assistance during the STM measurements and the quick answers from Marin

on several questions were helpful, especially at the end. The discussions with Marko and Marin helped a lot in understanding.

I would like to thank **Prof. Dr. Andreas Stierle** and **Dirk Franz** for the nice collaboration.

Furthermore, my thanks are addressed to **Takahiro Seo**, who did a good job in upgrading our test chamber and the work on high-vacuum preparation of graphene. Sadly, we ran out of time.

I would like to thank **Benjamin Fiedler**, who provided us with the software *MCPdeskew*.

Prof. Dr. Thomas Michely danke ich für die guten Diskussionen bei offenen Fragen und entscheidenden Hinweise für die Lösung von Problemen. Ausserdem danke ich **Thomas Köthe**, **Jonas Weinen** und **Fabio Strigari** für die anregenden Diskussionen bezüglich XPS, welche zum Verständnis der Daten von großem Nutzen waren.

Darüber hinaus möchte ich den Kolleginnen und Kollegen der AG Michely für die nette Arbeitsatmosphäre danken. Insbesondere danke ich **Norbert Henn** für die Lösung existierender (und manchmal auch nicht existierender) technischer Probleme. Für die guten Hinweise zu Interkalation und Clustern möchte ich mich bei **Timm Gerber**, **Stefan Schumacher** und **Ulrike Schröder** bedanken. Mein ganz besonderer Dank für die schöne gemeinsame Zeit mit *Lotti* (auch wenn sie manchmal zickig war) gilt meinen Kollegen **Fabian Craes** und **Jürgen Klinkhammer**. Für die guten Korrekturen zu meiner Arbeit möchte ich mich bei **Fabian Craes** und ganz besonders bei **Dr. Sebastian Standop** bedanken, die mich dazu bewegt haben, die ein oder andere Argumentationskette umzudrehen, zu entflechten oder manchmal besser ganz weg zu lassen. Darüber hinaus danke ich dem gesamten Institut für die angenehme Atmospäre.

Ein großer Dank geht an die mechanische Werkstatt, ohne deren fachkundige Hilfe und hervoragende Arbeit *Lotti* niemals hätte so gut zurecht gemacht werden können. Darüber hinaus möchte ich mich insbesonere bei **Werner Külzer**, **Andreas Freimut**, **Peter Hansmann**, **Timur Zent** und **Adel Jawadi** für die nette Atmosphäre und die große Einsatzbereitschaft bedanken. Und das selbst dann, wenn *der Düsseldorfer* mal wieder mit viel zu komplizierten Zeichnungen und abstrusen Ideen in die Werkstatt kam. Letztendlich konnte jedes noch so schwierige Detail am Ende doch sehr schön gelöst werden; sogar die Deckenfedern.

Mein Dank gilt auch der Elektronik-Werkstatt, allen voran **Gerhard Menz**, **Klaus Lehmann** und **Harald Lüttgen**, ohne deren schnelle und gute Hilfe viele Verbesserungen in dieser Qualität nicht möglich geworden wären.

I would like to thank the theoreticians for acknowledging the fancy work in the lab, even in the case when just the cryostat was refilled.
I also would like to thank the **ESRF travel office** because they managed at the end of one beamtime to bring me back to the airport when the public transportation broke down during heavy snowfall. Without their help I might still be waiting for a flight back home.
I would like to thank **Dream Theater** and the **Trans Sibirian Orchestra**. Whenever I was highly unmotivated I have gained new impulses to go on writing.

Danken möchte ich insbesondere auch meiner Familie für die Unterstützung auch schon vor Beginn dieser Arbeit. Ebenso möchte ich meiner Schwiegerfamilie für die liebevolle Integration eines Physikers danken.

Den größten Dank möchte ich an meine Ehefrau **Meike** richten, die mich insbesondere in stressigen Zeiten liebevoll unterstützt und umsorgt hat. Für das Verständnis, dass ich an manchen späten Abenden noch im Keller (Labor) gesessen habe, weil ich meine Hände nicht von *Lotti* lassen konnte, möchte ich mich sehr bei ihr bedanken. *Viertelnachelf*

PART VIII

Formal Addenda

German Abstract - Deutsche Kurzzusammenfassung

Die Morphologie im System Graphen/Iridium(111) wurde mittels "X-ray Standing Wave" (XSW) Messungen untersucht. Dabei wurde eine Abhängigkeit der Moiré-Korrugation von der Graphenbedeckung beobachtet. Ein Vergleich dieser Daten mit Dichtefunktionaltheorie-Rechnungen (DFT) zeigt eine Abweichung der Korrugation in Folge von Druckspannungsabbau während des Abkühlenvorgangs im Zuge der Präparation. Das Modell der Rehybridisierung von Graphen durch Adsorption von metallischen Clustern wird durch Strukturmessungen bestätigt. Graphen-Interkalationsverbindungen wurden mittels Rastertunnelmikroskopie (STM), Niederenergetischer Elektronenbeugung (LEED) und XSW untersucht. Es wird gezeigt, dass Interkalation durch Brüche und Löcher in der Graphen-Lage an Graphenfalten und deren Kreuzungspunkten ermöglicht wird. Die Überstrukturphasen der Caesium-Interkalatverbindung werden gezeigt. Für Interkalate, deren Wechselwirkung mit der Graphenlage hauptsächlich durch die van-der-Waals Kraft beschrieben ist, wird gezeigt, dass der Ladungstransfer ebenfalls einen messbaren Einfluss auf den Abstand der Lagen hat. Darüber hinaus unterstützt eine Strukturanalyse im System Graphen/O/Ir(111) die Annahme von quasi freistehendem Graphen. Ein "rigid-band" Modell wird eingeführt und auf verschiedene Interkalationverbindungen angewendet. STM-Messungen zeigen eine eindeutige Signatur von Dirac-Elektronenstreuung an Defekten. Diese Prozesse beinhalten sowohl "inter-" als auch "intravalley" Streuung.

List of Publications

Parts of this thesis can also be found in these publications:

[49] M. Pletikosic, I. Šrut, S. Runte, C. Busse, J. T. Sadowski, P. Lazić, I. Pletikosić, Z.-H. Pan, M. Milun, P. Pervan, N. Atodiresei, R. Brako, Šokčević, T. Valla, T. Michely, M. Kralj
The Mechanism of Caesium Intercalation of Graphene
Nature Communications (accepted)

[71] S. Runte, C. V. Van, J. Coraux, J. Zegenhagen, T. Michely, and C. Busse
Graphene buckles under Strain
in preparation

[72] D. Franz, S. Runte, C. Busse, S. Schumacher, T. Gerber, T. Michely, M. Mantilla V. Kilic, J. Zegenhagen, and A. Stierle
Atomic Structure and Crystalline Order of Graphene Supported Ir Nanoparticle Lattices
Physical Review Letters **110**, 065503 (2013)

[73] D. Franz, N. Blanc, S. Runte, J. Coraux, U. Hejral, T. Gerber, C. Busse, T. Michely, A. Stierle
Structure of graphene/Ir(111) supported Pt clusters during CO/O2 exposure
in preparation

[74] S. Runte, C. V. Van, J. Coraux, J. Zegenhagen, T. Michely, and C. Busse
XSW Study of Graphene Intercalation Compounds
in preparation

[86] S. Schumacher, T. Wehling, P. Lazić, S. Runte, D. Förster, C. Busse, M. Petrović, M. Kralj, S. Blügel, N. Atodiresei, V. Caciuc, T. Michely
The Backside of Graphene: Manipulating Adsorption by Intercalation
Nano Letters **13**, 5013 (2013)

[93] T. Gerber, M. Petrović, E. Grånäs, S. Schumacher, S. Runte, F. Craes, D. F. Förster, U. Schröder, J. Coraux, C. Võ Văn, J. Zegenhagen, P. Pervan, C. Busse, M. Kralj, J. Knudsen, and T. Michely
Understanding Core Level Shifts of Doped Graphene
in preparation

[94] S. Runte, F. Craes, J. Klinkhammer, M. Petrović, M. Kralj, T. Michely, C. Busse
STS Investigation on Caesium Intercalated Graphene
in preparation

[96] F. Craes, S. Runte, J. Klinkhammer, M. Kralj, T. Michely, and C. Busse
Mapping Image Potential States on Graphene Quantum Dots
Physical Review Letters **111**, 056804 (2013)

Further publications:

[100] J. Klinkhammer, M. Schlipf, F. Craes, S. Runte, T. Michely, and C. Busse
Spin-Polarized Surface State in EuO(100)
Physical Review Letters (accepted)

[101] V. Geringer, M. Liebmann, T. Echtermeyer, S. Runte, M. Schmidt, R. Rückamp, M. Lemme, M. Morgenstern
Intrinsic and Extrinsic Corrugation of Monolayer Graphene Deposited on SiO2
Physical Review Letters **102** (7), 76102 (2009)

[102] A. Reinholdt, R. Pecenka, A. Pinchuk, S. Runte, L. A. Stepanov, T. E. Weirich, U. Kreibig
Structural, compositional, optical and colorimetric characterization of TiN-nanoparticles
The European Physical Journal D **31** (1), 69-76 (2004)

Offizielle Erklärung

Ich versichere, dass ich die von mir vorgelegte Dissertation selbständig angefertigt, die benutzten Quellen und Hilfsmittel vollständig angegeben und die Stellen der Arbeit - einschließlich Tabellen, Karten und Abbildungen -, die anderen Werken im Wortlaut oder dem Sinn nach entnommen sind, in jedem Einzelfall als Entlehnung kenntlich gemacht habe; dass diese Dissertation noch keiner anderen Fakultät oder Universität zur Prüfung vorgelegen hat; dass sie - abgesehen von unten angegebenen Teilpublikationen - noch nicht veröffentlicht worden ist, sowie, dass ich eine solche Veröffentlichung vor Abschluss des Promotionsverfahrens nicht vornehmen werde. Die Bestimmungen der Promotionsordnung sind mir bekannt. Die von mir vorgelegte Dissertation ist von Priv.-Doz. Dr. Carsten Busse, sowie von Prof. Dr. Thomas Michely betreut worden.